

REPORT DOCUMENTATION PAGE			Form Approved OMB NO. 0704-0188
<p>Public reporting burden for this collection of information is estimated to average 1 hour per response, including the time for reviewing instructions, searching existing data sources, gathering and maintaining the data needed, and completing and reviewing the collection of information. Send comment regarding this burden estimates or any other aspect of this collection of information, including suggestions for reducing this burden, to Washington Headquarters Services, Directorate for Information Operations and Reports, 1215 Jefferson Davis Highway, Suite 1204, Arlington, VA 22202-4302, and to the Office of Management and Budget, Paperwork Reduction Project (0704-0188), Washington, DC 20503.</p>			
1. AGENCY USE ONLY (Leave blank)	2. REPORT DATE May 18, 1999	3. REPORT TYPE AND DATES COVERED Final Report, November 1996-February 1999	
4. TITLE AND SUBTITLE THz Radiation Source Through Periodically Modulated Structures		5. FUNDING NUMBERS C N 68171-96-C-9015	
6. AUTHOR(S) E. Gornik, Ch. Rauch, G. Ploner			
7. PERFORMING ORGANIZATION NAMES(ES) AND ADDRESS(ES) Institut für Festkörperelektronik Technische Universität Wien Floragasse 7 A-1040 Wien, Austria		8. PERFORMING ORGANIZATION REPORT NUMBER Final Report	
9. SPONSORING / MONITORING AGENCY NAME(S) AND ADDRESS(ES) U.S. Army Research Office P.O. Box 12211 Research Triangle Park, NC 27709-2211		10. SPONSORING / MONITORING AGENCY REPORT NUMBER WK2Q6C-7372-EE01	
11. SUPPLEMENTARY NOTES The views, opinions and/or findings contained in this report are those of the author(s) and should not be construed as an official Department of the Army position, policy or decision, unless so designated by other documentation.			
12a. DISTRIBUTION / AVAILABILITY STATEMENT Approved for public release; distribution unlimited.		12 b. DISTRIBUTION CODE	
13. ABSTRACT (Maximum 200 words) The main goal of the project was to investigate various possible mechanism for coherent THz radiation sources based on semiconductor devices A novel concept considers the occurrence of a current driven plasma instability (CDPI) in a confined plasma. In this case tunnel injection can be used to achieve an inverted electron distribution by injecting carriers selectively into higher quantum well states and maintaining an efficient extraction scheme. In this project we have demonstrated for the first time that these injection-extraction structures can be realized by MBE growth and characterized by transport experiments. Two types of structures have been processes into ridge like mesa structures which have demonstrated for the first time THz emission at the energy of the confined plasmon. The observation of electrically excited plasmon emission from parabolic quantum well up to temperatures close to room temperature is milestone for further work. It demonstrates the stability of the plasmon oscillation process and its potential for practical radiation sources. Bunching of electrons has been achieved by the localization of electrons in Bloch oscillations, which is another concept towards the realization of coherent THz emission. High quality superlattice sample were grown and investigated by current spectroscopy in detail, to achieve the required mean free path. With optimized samples electrically induced Bloch emission in a semiconductor was observed for the first time.			
14. SUBJECT TERMS			15. NUMBER OF PAGES
			16. PRICE CODE
17. SECURITY CLASSIFICATION OR REPORT UNCLASSIFIED	18. SECURITY CLASSIFICATION OF THIS PAGE UNCLASSIFIED	19. SECURITY CLASSIFICATION OF ABSTRACT UNCLASSIFIED	20. LIMITATION OF ABSTRACT UL

NSN 7540-01-280-5500

Standard Form 298 (Rev. 2-89)
Prescribed by ANSI Std. Z39-18
298-102

THz RADIATION SOURCE THROUGH PERIODICALLY MODULATED STRUCTURES

Final Progress Report

E. Gornik, Ch. Rauch, and G. Ploner

May 15, 1999

**U.S. ARMY RESEARCH OFFICE
CONTRACT NO. N68171-96-C-9015**

**INSITUT FÜR FESTKÖRPERELEKTRONIK,
TECHNISCHE UNIVERSITÄT WIEN, AUSTRIA**

**APPROVED FOR PUBLIC RELEASE;
DISTRIBUTION UNLIMITED**

The views, opinions, and/or findings contained in this report are those of the authors and should not be construed as an official position, policy, or decision, unless so designed by other documentation.

SUMMARY

The main goal of the project was to investigate various possible mechanism for coherent THz radiation sources based on semiconductor devices. For this purpose we consider concepts in which the electron distribution and correspondingly the emission spectrum can be influenced by bandstructure engineering especially by the growth of nano- structures.

A novel concept considers the occurrence of a current driven plasma instability (CDPI) in a confined plasma. In this case tunnel injection can be used to achieve an inverted electron distribution by injecting carriers selectively into higher quantum well states and maintaining an efficient extraction scheme. In this project we have demonstrated for the first time that these injection-extraction structures can be realized by MBE growth and characterized by transport experiments. Two types of structures have been processes into ridge like mesa structures which have demonstrated for the first time THz emission at the energy of the confined plasmon. A plasma instability has not been achieved yet, but the results indicate that an instability is feasible, if a further improvement of the concept and the structures is achieved. The observation of electrically excited plasmon emission from parabolic quantum well up to temperatures close to room temperature is milestone for further work. It demonstrates the stability of the plasmon oscillation process and its potential for practical radiation sources.

A second concept considers the occurrence of a current driven plasma instability, when the drift velocity exceeds the Fermi velocity. However the necessary drift velocities are unrealistically high. In modulated systems and especially in modulated high mobility quantum wire systems the CDPI effect is expected to occur at lower drift velocities. However the study of quantum wire properties did not yet lead to the required quality of wires and the necessary drift velocities.

Electrons drifting in a periodic potential can emit coherent THz radiation, if a bunching of electrons is achieved. This bunching requires an electron mean free path, which is larger than the period of the potential modulation. The bunching of electrons can also be achieved by the localization of electrons in Bloch oscillations, which is another concept towards the realization of coherent THz emission. High quality superlattice sample were grown and investigated by current spectroscopy in detail, to achieve the required mean free path. With optimized samples electrically induced Bloch emission in a semiconductor was observed for the first time. As the IV-curves of superlattices with a negative conductance part are robust up to high temperatures, the Bloch type of emission may persist up to temperatures close to room temperature. The basic charge oscillations rely on the bunching of macroscopic charges in a similar way as the case of the Plasma instability.

List of Publications

K. Kempa, P. Bakshi, C. Du, G. Feng, A. Scorupsky, G. Strasser, C. Rauch, K. Unterrainer, and E. Gornik

“Towards stimulated generation of coherent plasmons in nanostructures”
Journal of Appl. Physics **84** (7), 1 (1999).

C. Rauch, G. Strasser, and E. Gornik

“Current Spectroscopy of Superlattice Bandstructure and Transport”
Microelectronic Engineering (to be published).

C. Rauch, G. Strasser, K. Unterrainer, A. Wacker, and E. Gornik

“Transition between coherent and incoherent electron transport in GaAs/AlGaAs superlattices”

Phys. Rev. Lett. **81**, 3495 (1998).

C. Rauch, G. Strasser, M. Kast, and E. Gornik

“Mean Free Path of Ballistic Electrons in GaAs/AlGaAs Superlattices”
Superlattice and Microstructures **25**, 47 (1999).

A. Wacker, S. Bose, C. Rauch, G. Strasser, and E. Gornik

“Transmission through Superlattices with Interface Roughness”
Superlattice and Microstructures **25**, 43 (1999).

K. Kempa, P. Bakshi, C. Du, G. Feng, A. Scoropsky, E. Gornik, G. Strasser, K. Unterrainer, and C. Rauch

“Inter-subband scattering rates, population inversion and stimulated emission of THz plasmons in bounded quantum systems.”

Conference Proceedings of the 24th International Conference on the Physics of Semiconductors (to be published).

C. Rauch, M. Kast, G. Strasser, K. Unterrainer, A. Wacker, S. Bose, and E. Gornik

“Coherence Length of Ballistically Injected Hot Electrons in GaAs/AlGaAs Superlattices”

Conference Proceedings of the 24th International Conference on the Physics of Semiconductors (to be published).

G. Strasser, C. Rauch, K. Unterrainer, W. Boxleitner, K. Kempa, E. Gornik

“Ballistic and dissipative electron transport in semiconductor superlattices”

Physica E **3**, 152 (1998).

G. Strasser, C. Rauch, K. Kempa, and E. Gornik
“Ballistic Electron Transport In Semiconductor Superlattices”
Proc. IEEE 24th Int. Symposium on Compound Semiconductors, San Diego (1997), p267-270: Ed.: M. Melloch & M. Reed; IEEE Institute of Physics Publishing, Bristol & Philadelphia 1998.

C. Rauch, G. Strasser, K. Unterrainer, W. Boxleitner, and E. Gornik
“Quenching of miniband transport in biased undoped superlattices”
phys. stat. sol. (b) 204, 393 (1997).

C. Rauch, G. Strasser, K. Unterrainer, K. Kempa, and E. Gornik
“Ballistic electron transport in vertical biased superlattices”
Physica E 2, 282 (1998).

G. Strasser, C. Rauch, and E. Gornik
“Current transport in multiple superlattice structures”
Physica E 2, 515 (1998).

C. Rauch, G. Strasser, K. Unterrainer, B. Brill, and E. Gornik
“Ballistic Electron Spectroscopy of Superlattice Minibands”
Appl.Phys.Lett. 70, 649 (1997).

C. Rauch, G. Strasser, K. Unterrainer, and E. Gornik
“Ballistic electron spectroscopy of semiconductor heterostructures”
Basics of semiconductor device technology (1997) ISBN: 3-901578-02-1.

C. Rauch, G. Strasser, K. Unterrainer, W. Boxleitner, E. Gornik, B. Brill, U. Meirav, and M. Heiblum
“Direct Ballistic Electron Spectroscopy of Vertical Superlattice Minibands”
Superlattices and Microstructures, 22 (2), 143 (1997).

W. Boxleitner, C. Rauch, G. Strasser, L. Hvozdara, E. Gornik, U. Meirav, V. Umansky, and H. Shtrikman
“Electron Dynamics and Band Structure in high quality GaAs/AlGaAs Superlattices”
Proceedings of the ICPS XXIII, Berlin 1996.

Talks

“Ballistic electron spectroscopy of semiconductor superlattices”

International Conference on High Field Transport in Superlattices, Trieste, Italy (08/1999), invited.

“Scattering and Bloch oscillation in semiconductor superlattices”

International Conference on Nonequilibrium Carrier Dynamics in Semiconductors (HCIS-11), Kyoto, Japan (07/1999), invited.

“Coherent and incoherent transport in semiconductor superlattices”

American Physical Society, Centennial Meeting, Atlanta, USA (03/1999).

“Transition between coherent and incoherent miniband transport in semiconductor superlattices”

University of Technology Berlin, Germany (12/1998), invited.

“Transmission through undoped biased GaAs/AlGaAs superlattices”

University of Erlangen-Nürnberg, Germany (11/1998), invited.

“Transmission through superlattices with interface roughness”

International Conference on Superlattices, Microstructures and Microdevices-11, Hurgada, Egypt (07/1998).

“Mean free path of ballistic electrons in GaAs/AlGaAs superlattices”

International Conference on Superlattices, Microstructures and Microdevices-11, Hurgada, Egypt (07/1998).

“Ballistic Electron Spectroscopy of semiconductor Quantum Devices”

QUEST Seminar, University of California Santa Barbara, USA (07/1998), invited.

“Ballistic Electron Spectroscopy of semiconductor Quantum Devices”

40 th Electronic Materials Conference, Charlottesville, USA (06/1998).

“Transition between coherent and incoherent electron transport in biased superlattices”

Solid State Electronics, TU Vienna, Austria (03/1998).

“Coherence length in GaAs/AlGaAs superlattices”

4th Seminar on Quantum Heterostructures and Superlattices, Regensburg, Germany (01/1998), invited.

“Transport in Halbleiterquantensystemen, Entwicklung von THz Quellen”

Atominstutit der österreichischen Hochschulen, Vienna, Austria (01/1998).

“Hot electron transport in semiconductor quantum heterostructures”

International Conference on Hot Carriers in Semiconductors-10, Berlin, Germany
(08/1997).

“Ballistic electron spectroscopy of biased undoped superlattices”

International Conference on Modulated Semiconductor Structures-8, Santa Barbara, USA
(07/1997).

„Coherence Length of Ballistically Injected Hot Electrons in GaAs/AlGaAs Superlattices”

24th International Conference on the Physics of Semiconductors (ICPS-24), Jerusalem,
Israel (1998)

Diploma Theses and PhD Theses

- ◆ W. Boxleitner, Bandstructure and Ballistic Transport in Semiconductor Heterostructures, (PhD Thesis, TU Wien, June 1997)
- ◆ Ch. Rauch, Ballistic Electron Transport in Semiconductot Heterostructures (PhD Thesis, TU Wien, Sept. 1998)
- ◆ G. Ploner, Quantum Wires: Investigation of Fabrication and Characterization Techniques (PhD Thesis, TU Wien, Dec. 1998)
- ◆ R. Zobl, THz Plasmon Emission (PhD Thesis, TU Wien in Progress)
- ◆ C. Pacher, Development of THz Emission Devices (Diploma Thesis, TU Wien, finished Jan. 1999)

List of participating Scientific Personal

Prof.Dr. E. Gornik: Principal investigator

Dr.K. Unterrainer , Dr.G. Strasser : Research Associates

Ch. Rauch, G. Ploner: PhD students both 50% employed within the project

W. Boxleitner: PhD student

R. Zobl, C. Pacher: Diploma thesis student

CONTENTS

1. BALLISTIC ELECTRON TRANSPORT	7
1.1. TUNNEL BARRIER INJECTOR	7
1.2. HOT ELECTRON SPECTROSCOPY	8
1.3. EXPERIMENTAL APPROACH	9
<i>1.3.1. Molecular Beam Epitaxial Growth.</i>	9
<i>1.3.2. Three Terminal Device Fabrication</i>	11
<i>1.3.3. Measurement Setup.</i>	14
1.4. HOT ELECTRON DISTRIBUTION OF A TUNNELING BARRIER EMITTER.....	14
1.5. BALLISTIC ELECTRON SPECTROSCOPY OF UNBIASED UNDOPED SUPERLATTICES	17
<i>1.5.1. Mapping the Miniband Positions</i>	17
1.6. BALLISTIC ELECTRON SPECTROSCOPY OF BIASED UNDOPED SUPERLATTICES	19
1.7. QUANTUM WIRE DEVICES.....	29
<i>1.7.1. Characterization by magnetophonon spectroscopy</i>	31
<i>1.7.2. Vertical tunneling through tunable quantum wires.</i>	40
2. EMISSION STUDIES	54
2.1. MULTIPLE SUPERLATTICE STRUCTURES	54
<i>2.1.1. Higher current Three Terminal Devices</i>	57
2.2. EMISSION MEASUREMENT TECHNIQUE.....	59
2.3. GENERATION OF PLASMON EMISSION FROM PARABOLIC QUANTUM WELLS	61
2.4. GENERATION OF COHERENT PLASMONS FOR RADIATIVE DECAY	65
<i>2.4.1. Transport characterization</i>	67
<i>2.4.2. Emission experiments</i>	70
<i>2.4.3. New plasmon generation concepts</i>	73
2.5. SUPERLATTICE EMISSION, BLOCH EMISSION	76

Part A

Electron Transport

E. Gornik, C. Rauch, G. Ploner, G. Strasser, C. Pacher, R. Zobl and W. Boxleitner

In this part of the project we investigate the transport properties of semiconductor superlattices, to obtain basic information for injection and emission structures. The technique applied is based on a transistor like structure to measure the mean free path of ballistically injected hot electrons. This is of great relevancy, since one of the basic requirements for the realization of an emission source in the THz regime is the knowledge of the nonradiative scattering mechanisms.

A systematic study of undoped GaAs/AlGaAs superlattices is performed. The measurements are carried out using a hot electron transistor as an electron spectrometer. The transmittance of the superlattice at different superlattice bias conditions is measured by varying the energy of the injected hot electron beam. For a short period superlattice the transmittance is found to decrease with the electric field for positive and negative biases due to an increasing localization of the wave function. For a superlattice longer than the coherence length, the transmission becomes asymmetric and dependent on the electric field direction. The onset of scattering induced miniband transport is clearly evident and the transition between coherent and incoherent electron transport in superlattices is observed for the first time. A coherence length of 150 nm and a scattering time of 1 ps is determined. The experimental results are in good agreement with a fully three dimensional calculation including interface roughness with typical island sizes of 10 nm, demonstrating that interface roughness scattering limits the coherence length of ballistic electrons.

The second part of this chapter deals with the study of quantum wires. Quantum wires provide a tool for tunable subband systems, which can basically be applied for generation and detection devices in the THz regime. Here we present the development of a new transport method which probes the subband spacing of quantum wires in the case of low numbers of occupied subbands. It relies on the observation of the so-called magnetophonon resonance in 1D electron gases and has the additional advantage that it can be carried out at relatively high temperatures (above 77 K).

A new device is introduced, which in a simple and flexible way overcomes the difficulties encountered when independent contacts are to be established to two closely spaced electron gases. In addition, the new device allows to impose an electrostatically tunable confinement on its active region and to study tunneling processes for varying dimensionality of the initial and final states. The results will be discussed with regard to possible applications of quantum wires for far infrared detectors.

1. BALLISTIC ELECTRON TRANSPORT

Ballistic electron transport is of technological and scientific interest. Technologically, ballistic electrons might become the basis for a generation of electronic devices that are at least an order of magnitude faster than today's devices. Scientifically, ballistic electron devices can be used to investigate the quantum mechanical properties of coherent electrons in semiconductors, because these electrons, like ballistic electrons in a vacuum tube, can be studied as freely moving quantum mechanical wave packets.

1.1. Tunnel Barrier Injector

As indicated in *Figure 1*, in a three terminal device, a tunneling barrier is used to generate ballistic electrons which are injected into a thin highly doped base. These injected hot electrons represent the input signal of the ballistic electron spectrometer.

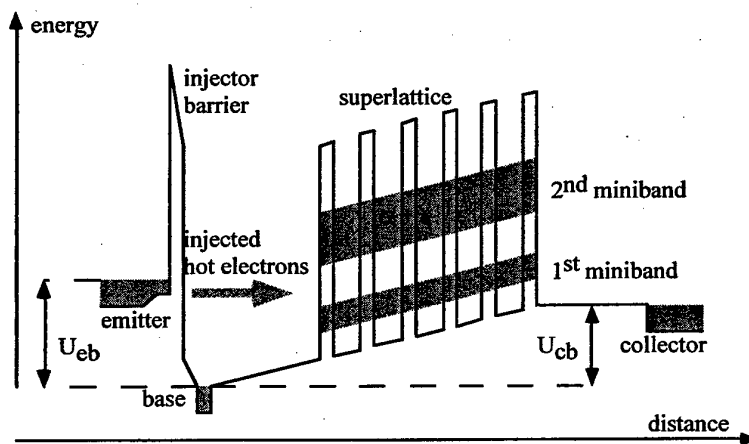


Figure 1: The conduction band of a hot electron transistor used in our experiments under typical bias conditions. Quasi-monoenergetic hot electrons are injected at the tunneling barrier. Scattered electrons are collected at the base, transmitted electrons are measured at the collector contact.

The growth parameters of this tunneling injector are of significant importance since the width of the injected electron distribution limits the energy resolution of the experiment. The probability that an electron will tunnel depends in part on the applied voltage and the thickness of the barrier. The thickness of the spacer layers to the left and to the right of the tunneling barrier influences the width of the injected energy distribution. The total energy of the tunneling electrons does not change because tunneling is an elastic process. Consequently, the kinetic energy of the electrons increases when they tunnel from a region of high potential energy to a region of low potential energy, meaning they are injected with surplus kinetic energies. In addition, the electrons that tunnel are mainly electrons that are moving in directions perpendicular to the barrier since the tunneling probability is a

function of the component of the k -vector that is perpendicular to the tunneling barrier, and so the injected electrons form an energy beam that is mostly aimed parallel to the growth direction. The kinetic energy with which the electrons are injected depends linearly on the applied voltage, and so it is easy to adjust.

1.2. Hot Electron Spectroscopy

Hot electron spectroscopy is a powerful tool to investigate the transmission properties of semiconductor quantum structures. This technique is basically a three terminal extension of conventional diode transport structures, where ballistic electrons are injected via an AlGaAs tunneling barrier into the semiconductor heterostructure under investigation. Since the structure resembles a unipolar transistor, standard notation to describe the currents and voltages involved is used. The emitter/base junction functions as a hot electron injector and the base/collector junction as a hot electron analyzer. When the emitter is biased negative, electrons are injected into the base region with an excess energy $e.U_{EB}$ above the energy of the base Fermi energy. Electrons that pass the superlattice are measured at the highly doped GaAs collector layer. The transfer ratio $\alpha=I_C/I_E$ reflects the probability of an electron to cross the base and the superlattice at given emitter energies.

To understand the basic principle of hot electron spectroscopy it is useful to have a simple picture in mind which is illustrated in Figure 2. The collected current is assumed to result as a convolution between the injected hot electron distribution and the transmission characteristics of the miniband. The energy distribution is considered to have a sharp edge at the high energy side, and a smoother tail at lower energies. Figure 2 (a) shows the situation where no collector current is observed since the energy of the injected hot electrons is lower than the lower edge of the first miniband. All the electrons are reflected by the superlattice and are collected at the base. As the upper edge of the injected hot electron distribution reaches the lower edge of the first miniband an increase of the transfer ratio is observed (Figure 2 (b)). The injected electrons now do have an energy that is high enough to tunnel through the first miniband. Thus the onset of the first peak can be associated with the energy position of the first miniband with respect to the GaAs conduction band edge. For energies higher than the first miniband the transfer ratio drops quite significantly (Figure 2 (c)) since there is no transport possible through the forbidden minigap of the superlattice. The second observed peak shifted 36 meV to higher injection energies, can be ascribed to electrons that are injected into the drift region, have lost the energy of a longitudinal optical phonon ($\hbar\omega_{LO}=36$ meV). Since the electron momentum for longitudinal optical phonon scattering is conserved, these electrons can also tunnel through the miniband (Figure 2 (d)).

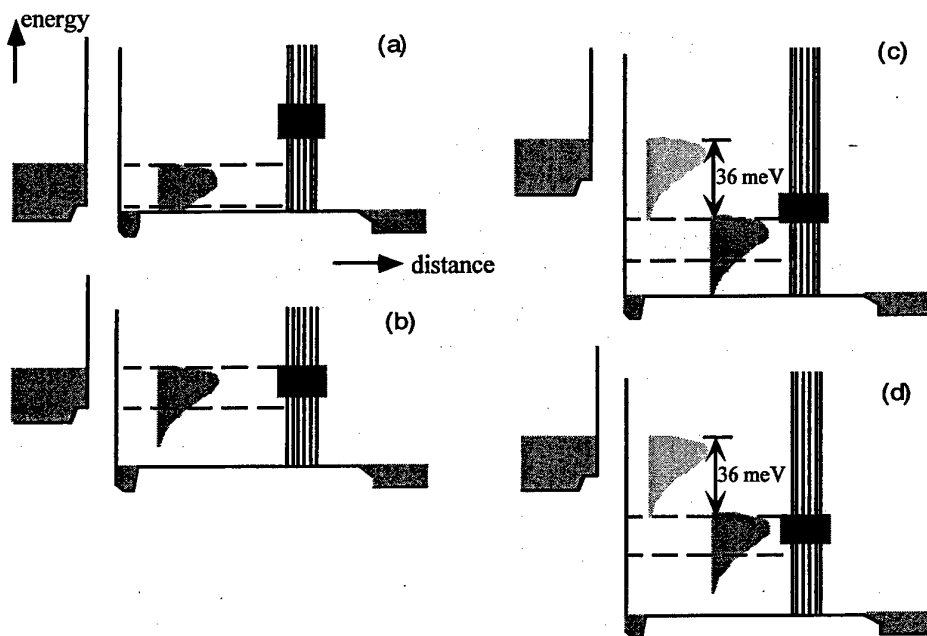


Figure 2: Sketch showing how the transfer ratio results as a consequence of a convolution between the injected carrier distribution and the transmittance of the superlattice.

It should be noted that the energy resolution of the experiment is mainly limited by the width of the injected electron distribution and can be improved by increasing the thickness of a spacer layer grown in between the injector barrier and the highly doped emitter contact.

1.3. Experimental Approach

In this section, the fabrication of a three terminal device will be described. The fabrication process can be divided into two main steps: molecular beam epitaxial growth and forming of planar structures using photolithography.

1.3.1. Molecular Beam Epitaxial Growth

All samples were grown on epi-ready semiinsulating GaAs material at a substrate temperature of 420°C. Typical growth rates, measured using RHEED oscillations, are about 1.1 μm/h. A typical layer structure, used in the experiments is shown in Figure 3.

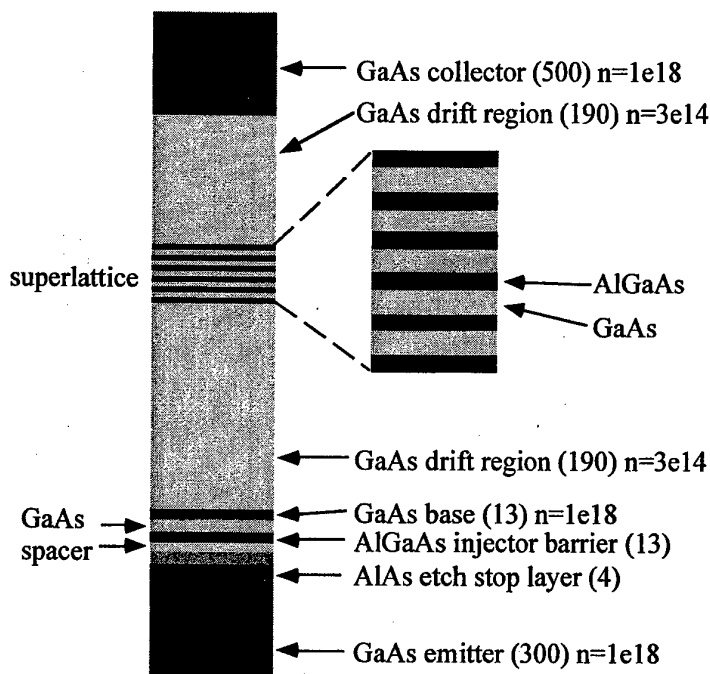


Figure 3: Layer structure of a typical three terminal structure. The layer thicknesses are given in nm and the doping concentrations in cm^{-3} .

The growth started with a highly doped ($n = 1 \times 10^{18} \text{ cm}^{-3}$) 500 nm GaAs collector contact layer followed by a 140 nm GaAs drift region. The drift region is slightly n-doped in order to avoid undesired band bending. A doping concentration of $n = 3 \times 10^{14} \text{ cm}^{-3}$ assures a high mean free path (in the order of 3 μm) and no band bending.

The drift region is followed by the superlattice under investigation. The superlattices consist of 2.5 nm AlGaAs barriers with an Al content of $x = 0.33$ and GaAs wells with different well widths. The sample parameters are given in *Table 1*.

Wafer No.	No. of periods	Well widths (nm)	Barrier thickness (nm)	remarks
G351	5	6.5	2.5	
G338	10	6.5	2.5	
G186	10	6.5	2.5	older
G339	15	6.5	2.5	
G352	20	6.5	2.5	
G353	30	6.5	2.5	
G175	5	15	2.5	
G174	5	8.5	2.5	
G169	5	6.5	2.5	

Table 1: Superlattice growth parameters

The growth continues with a 160 nm slightly doped ($n = 3 \times 10^{14} \text{ cm}^{-3}$) drift region and a 30 nm undoped GaAs spacer layer. This drift region has been added to the structure in

order to reduce quantum confining effects originating from the quantum well formed by the emitter barrier and by the superlattice.

This is followed by a highly doped ($n = 1 \times 10^{18} \text{ cm}^{-3}$) GaAs base layer of 13 nm width. This contact layer has to be very thin because otherwise too many electrons are lost due to electron-electron scattering in this highly doped region. About 60 % of the injected hot electrons traverse the base ballistically. On top of the base layer a 200 nm GaAs spacer and a 13 nm $\text{Al}_{0.33}\text{Ga}_{0.67}\text{As}$ injector barrier is grown followed by another 10 nm GaAs spacer layer and a 20 nm nominally n-doped ($n = 3 \times 10^{17} \text{ cm}^{-3}$) layer, in order to achieve an estimated full width at half maximum of the normal energy distribution of injected electrons of less than 20 meV. Finally a highly doped n^+ layer is grown on top to form the emitter contact.

The carrier concentration versus depth can be measured using a standard BioRad C-V etch profiler. Figure 4 shows the doping profile of sample g175. The carrier concentration of the emitter and collector is $n = 1.1 \times 10^{18} \text{ cm}^{-3}$ while the carrier concentration at the base seems to be less than the nominal value of $n = 1 \times 10^{18} \text{ cm}^{-3}$. This is partly caused by the limited resolution of the C-V profiler and by diffusion of the donor atoms to the spacer layers. However the position of the base layer with respect to the surface can be determined very well and compared to the nominal position. Usually deviations of the layer thicknesses of less than 5 % are observed.

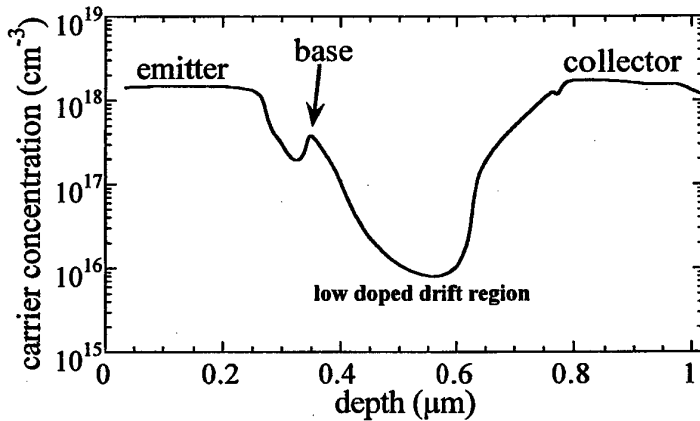


Figure 4: Measured carrier concentration versus depth of an MBE grown three terminal structure. The accurate position of the base is clearly evident.

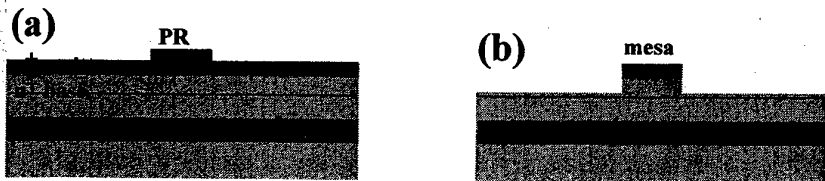
1.3.2. Three Terminal Device Fabrication

The processing of three terminal devices include basically five lithographic steps. Since the accuracy between following fabrication steps has to be very high ($\pm 0.5 \mu\text{m}$), appropriate markers are added to the mask. The pattern-generated mask is designed using AutoCAD. The size difference between markers on the mask to the markers on the sample

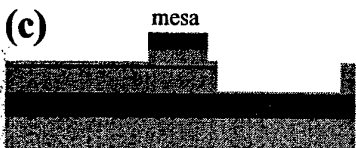
is 2 μm . It should be noted that all lithographic steps are aligned to markers evaporated at the beginning of the processing in order to avoid continuation errors.

The following describes the fabrication of one device. Practically, about 400 devices are produced on one $6 \times 6 \text{ mm}^2$ piece of GaAs.

A) Selective etching of the emitter mesa to define the active area ($30 \times 30 \mu\text{m}^2$).



B) Etching to the collector layer



A typical vertical profile of the structure after etching is shown in *Figure 5* measured using an alpha stepper (force 5 gram, speed slow, high resolution).

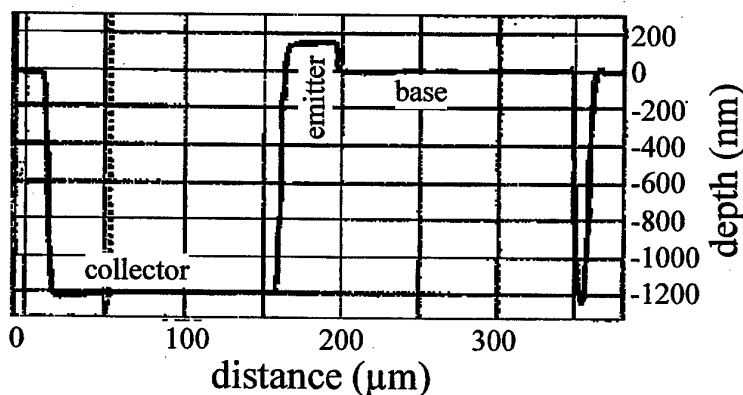
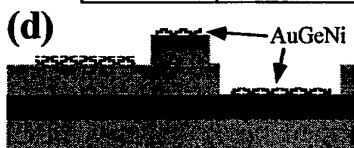


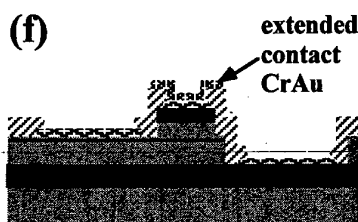
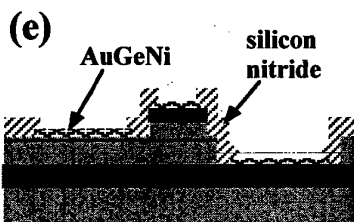
Figure 5: Measured vertical profile of a three terminal device using an alpha stepper.

C) Evaporation of ohmic contacts to emitter, and collector

material	Thickness (nm)	Deposition rate (nm/s)
Ge	15	2
Au	30	2
Ni	14	0.3
Au	230	3



D) Silicon nitride isolation layer (PECVD). Serves as an isolation layer of the extended contact of the emitter mesa to the underlying base layer.



E) Evaporation of the extended emitter contact pad

material	Thickness (nm)	Deposition rate (nm/s)
Cr	10	3
Au	250	3

F) Wire bonding

A picture of the device is shown in *Figure 6*.



Figure 6: Photograph of a bonded three terminal device. The tiny mesa structure can be found in the middle of the picture.

1.3.3. Measurement Setup

Most of the measurements are done at 4.2 K in a helium dewar. The sample is mounted on an eight pin sample rod. Since the currents at the collector are relatively low the dewar, sample rod and the coax cables are very well shielded to avoid unnecessary noise.

Some measurements are performed in a cryostat which is equipped with a magnet for fields up to 11 Tesla and a variable temperature insert (VTI). The sample can be cooled inside the VTI in a temperature range from 2 to 300 K. The temperature is measured with an Allen Bradley resista 1 cm above the sample. A simplified block diagram of the measurement setup is shown in Figure 7.

The transfer characteristics of the samples are measured using an HP 4155A semiconductor parameter analyzer with a $10 \text{ fA}/1\mu\text{V}$ resolution. The HP 4155A is equipped with four source/monitor units, all parameters like emitter voltage and current (U_{EB}, I_E), base current (I_B), and collector voltage and current (U_{CB}, I_C) can be recorded and controlled parallel during a measurement.

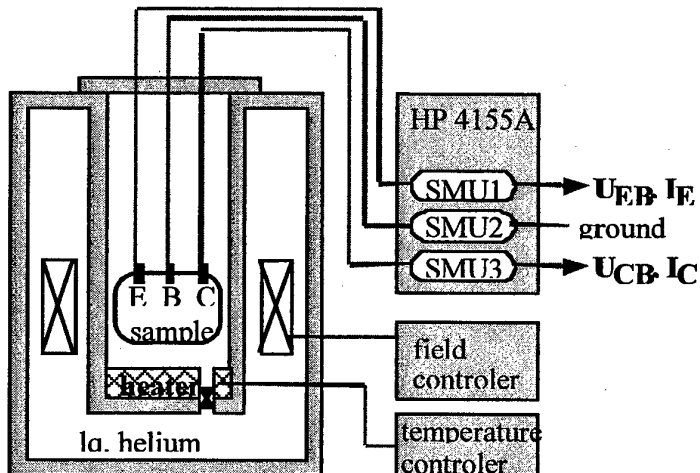


Figure 7: Measurement setup for current voltage characterization of the samples at different temperatures and different magnetic field. An HP parameter analyzer is used to apply voltages to emitter and collector as well as to measure current at the emitter and collector in parallel.

The measured collector current (I_C) is divided by the measured emitter current (I_E) to give the static transfer ratio $\alpha = I_C/I_E$ as a function of the applied emitter voltage (U_{EB}) at different collector bias conditions (U_{CB}) temperatures (T) and magnetic fields (B).

1.4. Hot Electron Distribution of a Tunneling Barrier Emitter

This section summarizes the results on the study of ballistic electron transport in GaAs/AlGaAs superlattices. Since the measured transfer characteristics is a convolution of the injected hot electron distribution and the superlattice under investigation, a reference sample is grown in order to determine the shape of the injected electron distribution experimentally (see section 1.4). Section 1.5 summarizes the results on ballistic electron

spectroscopy of field free undoped superlattices. Using this technique it is possible to map the positions of minibands and minigaps for superlattices with different well widths. Section 1.6 describes the effect of an electric field on the transmission properties of undoped superlattices of different lengths. The quenching of the ballistic transport through the superlattice due to Stark localization of the superlattice states is observed. The transition between coherent and incoherent transport in the superlattice is shown and the experimental results are used to determine the scattering time and the coherence length of an electron in an undoped superlattice. It is found that the coherence length is limited by interface roughness scattering.

To measure the energy distribution of ballistic hot electrons injected through a tunneling emitter, a three terminal device is grown as described in chapter 1.3.1. Instead of a superlattice a resonant tunneling diode (RTD) is grown in the drift region. The energy diagram of the conduction band of this device is shown in *Figure 8*.

The asymmetric resonant tunneling diode (6 nm Al_{0.3}Ga_{0.7}As barrier/12 nm GaAs well/8 nm Al_{0.3}Ga_{0.7}As barrier) acts as a normal energy filter for the injected electrons. The RTD is designed in a way that the first resonant state ($E_1 = 23\text{meV}$) is well below the energy of an longitudinal optical phonon ($\hbar\omega = 36\text{meV}$) to avoid electron loss due to LO-phonon scattering in the drift region.

The measured transfer ratio is shown in Figure 9 as a function of the injection energy which is equal to the applied negative emitter bias reduced by a constant offset due to the difference of the base Fermi level and the band edge of the drift region. Below the energy of the first resonant state E_1 of the RTD no collector current is observed, since no electrons have an energy that is high enough to cross the resonant tunneling barrier. The onset at about 21 meV determines the energy level of the first resonant state (E_1) of the analyzer RTD. Since the resonant linewidth of the double barrier structure is negligible compared to the width of the injector distribution, the measured transfer ratio is proportional to the hot electron distribution of the injector. The second peak at about 70 meV is due to electrons that have lost the energy of an LO-phonon while traversing the drift region. Since the k -vector is conserved for LO-phonon scattering processes ($q=0$ scattering is dominant), these electrons can be collected at an energy shifted by the LO-phonon energy (=36 meV).

Starting at about 90 meV transport through the second resonant state (E_2) is observed. This peak basically reproduces the shape of the injected hot electron distribution for higher injection energies. At 187 meV the third quantized level can be observed. The measured onsets of the transfer ratio agree well with the calculated positions of the quantized states ($E_{1,\text{calc}} = 23\text{ meV}$, $E_{2,\text{calc}} = 93\text{ meV}$, $E_{3,\text{calc}} = 196\text{ meV}$). The calculated positions are indicated by dashed lines in Figure 9. The overall increase of the peak value of the measured transfer ratio is a consequence of the increase of the linewidth of the resonant states with energy.

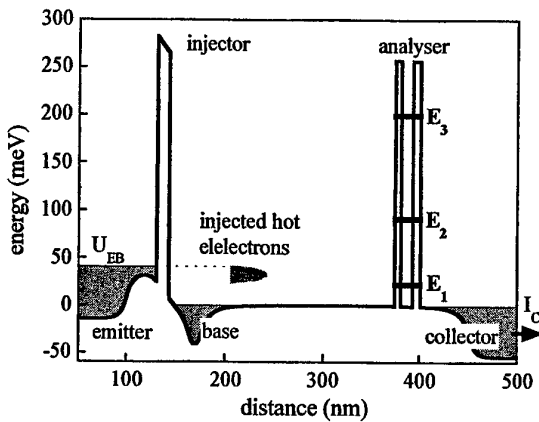


Figure 8: Schematic conduction band diagram of a transistor structure used to measure the injected hot electron distribution. A resonant tunneling diode is used as an energy band pass filter.

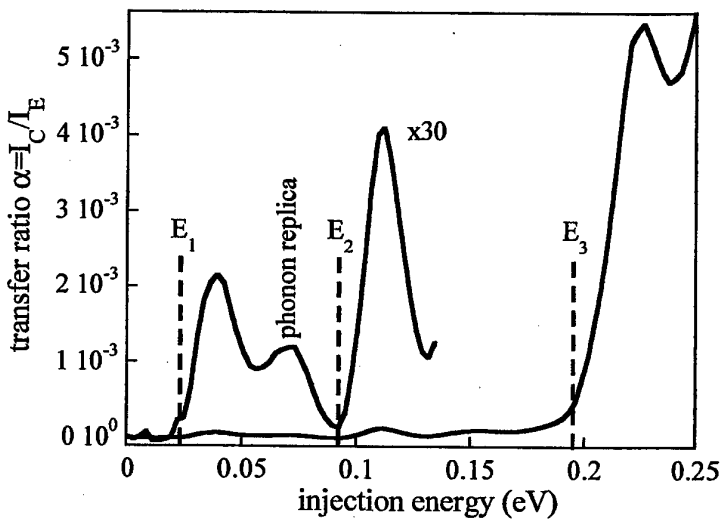


Figure 9: Measured static transfer ratio as a function of injection energy of a resonant tunneling diode grown in the drift region of a three terminal device. An increase of the transfer ratio at the nominal energy positions (dashed vertical lines) of the quantized states is clearly evident.

Since the first peak of the transfer ratio α is proportional to the injected hot electron distribution (dots *Figure 10*), the full width at half maximum can be determined from the experiment to be $\Delta E_{\text{inj}} = 20$ meV. The shape of the distribution is slightly asymmetric with its maximum at the high energy side. We observe no significant change with higher injection energies up to 200 meV.

The measured energy distribution is compared to simulations in *Figure 10*. The calculation is based on a transfer matrix method for the envelope functions of the Γ_8 valley of GaAs/AlGaAs. The different effective masses and nonparabolicity are taken into

account in our model. From the transmission coefficients of the injector and the RTD the injected energy distribution and the ballistic current are calculated [1].

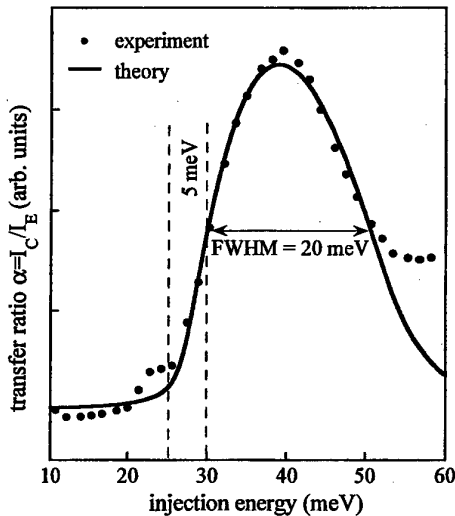


Figure 10: The experimentally determined shape of the injected hot electron distribution (dots) of a 13 nm AlGaAs tunneling barrier injector compared to a calculation based on a transfer matrix method (solid line).

1.5. Ballistic Electron Spectroscopy of unbiased undoped Superlattices

In this section a detailed systematic study of ballistic transport in field free GaAs/AlGaAs superlattices with different well widths is presented. Since the high quality structures are undoped, the influence of electron-electron and electron impurity scattering can be neglected. Under flat band conditions the eigenstates of the periodic structure are expected to be extended over the entire length of the superlattice.

1.5.1. Mapping the Miniband Positions

Three different superlattices with six AlGaAs barriers (2.5 nm) and five GaAs wells of varying widths, 6.5 nm, 8.5 nm, and 15 nm are studied. The miniband positions are calculated using a self-consistent Schrödinger calculation. A summary of the superlattice tunneling structures investigated is given in *Table 2*, where Δ_{MB1} and Δ_{MB2} denote the widths of the first and of the second minibands, Δ_{01} the energy position of the first miniband with respect to the conduction band edge and Δ_{12} denotes the width of the minigap between the first and the second miniband.

Sample No.	Well (nm)	Δ_{01} (meV)	Δ_{MB1} (meV)	Δ_{12} (meV)	Δ_{MB2} (meV)
G169	6.5	46	22	114	94
G164	8.5	33	13	85	53
G175	15	14.5	3.5	40	14

Table 2: Miniband parameters

In *Figure 11* the schematic equilibrium Γ -point conduction band energy diagram including band bending is shown for typical biasing conditions.

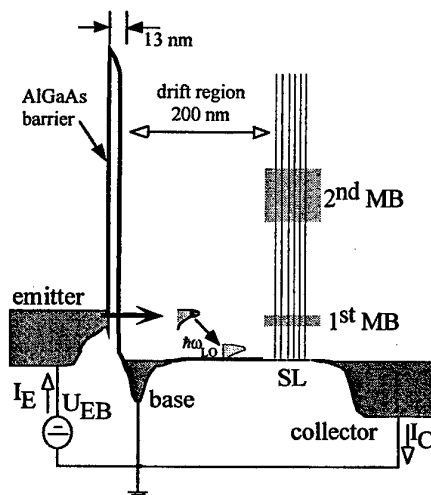


Figure 11: Schematic band diagram showing the conduction band edge of a three terminal device under forward emitter bias and a superlattice under flat band condition. The measurement circuit is drawn schematically.

The static transfer ratio of sample g164, $\alpha = I_C/I_E$, plotted in *Figure 12* as a function of the injection energy shows several maxima and a sharp rise at 280 meV. The position of the first peak coincides very well with the first miniband. Thus, we claim that the first peak is due to miniband transport through the lowest miniband. For energies higher than the first miniband the transfer ratio drops quite significantly since there is no transport possible through the forbidden minigap of the SL. The second observed peak is shifted 36 meV to higher injection energies and is ascribed to the first LO-phonon emission replica ($\hbar\omega_{LO} = 36$ meV) of the injected electron distribution. The relative position in energy and width are equal to that of the first peak. The energy range of electrons injected at voltages corresponding to this second peak is in the forbidden band and no contribution is expected from electrons which have not lost energy due to optical phonon emission. The peak at 150 meV represents transport through the second SL miniband.

For an analysis of the observed features we compare the experimental data with the theoretically calculated miniband positions. The calculated positions and widths of the first and second miniband are indicated by bars. An excellent agreement of the onset of the

transfer ratio peaks and the lower edge of the calculated miniband positions is found. The sharp rise of the transfer ratio at 280 meV is due to the transition to continuum states. This energy, which corresponds to the conduction band offset of the superlattice barriers, gives us a confirmation of the AlAs mole fraction of the AlGaAs compound.

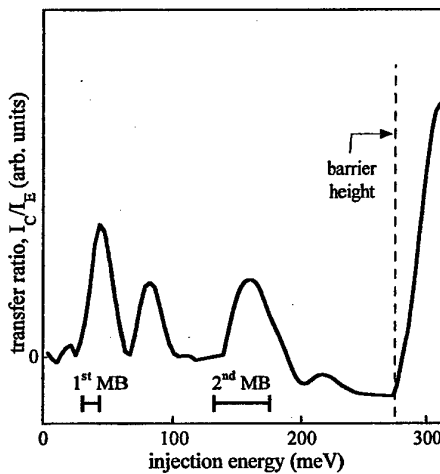


Figure 12: Transfer ratio $\alpha=I_C/I_E$ versus injection energy of sample g164. The calculated miniband positions are indicated by bars.

In *Figure 13* we show the transfer ratio α as a function of the injection energy for three samples with different well widths at lower injection energies. There is a clear shift of the peaks to higher energies with decreasing superlattice well width. The calculated miniband positions are again indicated by bars as in *Figure 12*. Note that it is possible to resolve even very narrow minibands at low energies as seen for sample g169. The reduced quality (signal to noise ratio) of the measured transfer ratio of this sample is due to the low number of electrons injected at low energies, thus the measured collector current is in the range of 2 pA. However the width of the injected electron distribution can be estimated to be about 20 meV since the calculated width of the first miniband of sample g169 is 3.5 meV and the measured width of the peak due to transport through the first miniband is 24 meV. Due to the finite width of the injected hot electron distribution (see section 1.4) the measured transfer ratios of all samples are broadened. This low energy tail of the injected electron beam is indicated by dashed bars in *Figure 13*.

It should be pointed out that this technique provides an unique possibility to map the positions of minibands in field free undoped superlattices. The structure described above gives the highest energy resolution reported so far.

1.6. Ballistic Electron Spectroscopy of biased undoped Superlattices

When a uniform electric field is applied to the superlattice, the quasi-continuous minibands break up into a ladder of discrete Wannier-Stark states. This localization of the electron wave function has direct consequences on the ballistic electron transport.

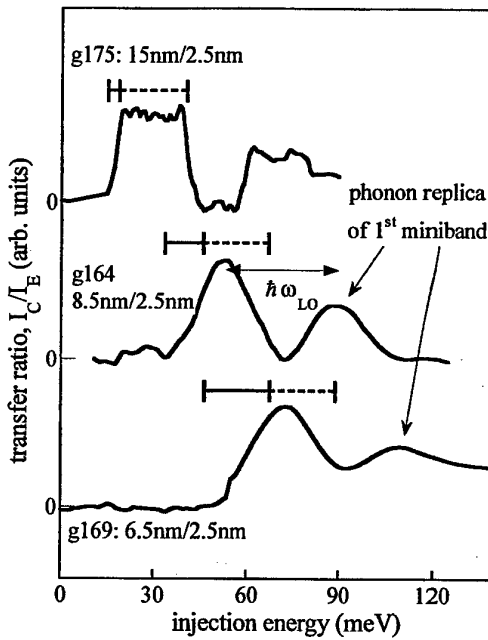


Figure 13: Transfer ratio α versus injection energy at lower injection energies for three samples with different well widths. The calculated miniband positions are indicated by solid bars as well as the broadening due to the finite width of the injected hot electron distribution (dashed bars). A double arrow represents the energy of a longitudinal optical phonon.

Considerable activity has been denoted to study the transport properties of biased superlattices in the literature. However, one of the main problems hindering the systematic experimental study of electron transport in superlattices has been the independence of the intensity of the current injected and the electric field present in the superlattice which is unavoidable in two terminal structures.

Using a three terminal device, one is able to inject ballistic hot electrons independently from the superlattice bias, thus the transmission properties of undoped superlattices can be measured in a very systematic way. The calculated equilibrium Γ -point conduction energy diagram including band bending is shown in Figure 14 under typical injection conditions for negative bias applied to the collector.

The measured transfer ratio α for a ten period superlattice (g338) under different negative collector base (U_{CB}) biases is shown in Figure 15.

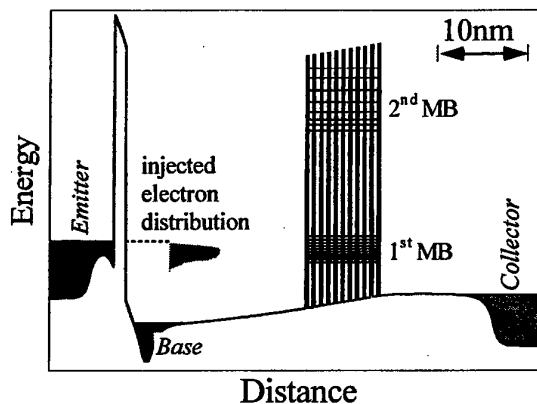


Figure 14: Calculated band diagram of a three terminal device for negative bias applied to the collector.

The black solid line represents the transfer ratio at flat band condition ($U_{CB}=0$). The sharp increase of the transfer ratio at about 45 meV coincides very well with the lower edge of the first miniband which is calculated to be 46 meV. The observed peak due to transport through the first miniband is broader than the expected miniband width ($\Delta= 22$ meV) due to the finite width of the injected electron distribution as discussed in chapter 1.4. Also the LO-phonon replica, shifted by 36 meV to higher injection energies is clearly evident. Assuming an optical phonon scattering time of 200 fs at 100 meV electron energy and an electron velocity of 7.2×10^5 m/s, about 80 % of the injected electrons are scattered in the drift region and loose 36 meV in energy. This results in a non vanishing transfer ratio between the peaks since the full width at half maximum of the injected electron distribution (20 meV) plus the width of the first miniband (22 meV) is greater than the LO-phonon energy. Superposition of the replicas and the non scattered electrons leads to the observed behavior in the transfer ratio as evident in the experiment (Figure 15). Even the second phonon replica, shifted by 72 meV to higher energies are observed at all biases.

The observed transfer ratio decreases quite dramatically with the applied electric field due to the localization of the electron wavefunctions in the superlattice.

The onset of the transfer ratio shifts with the applied collector-base bias since the lower edge of the first miniband shifts with the applied collector bias. This is mainly due to the voltage drop in the drift region between the superlattice and the base and due to the increasing localization of the lower miniband states that become non transparent for ballistic electrons meaning that the lowest transparent state is a level closer to the center of the miniband. The comparison of the measured miniband position (using the 3dB criterion) with the miniband position of the lowest transparent state derived from a self consistent Schrödinger calculation of the entire structure, gives the information about the voltage drop in the drift regions and in the superlattice.

Figure 16 shows the energy positions of the experimentally derived onsets of the transfer ratio plotted versus collector-base (U_{CB}) bias. The onset is measured at the 10 % onset of the maximum transfer ratio. A very linear but asymmetric behavior can be observed. The asymmetry can be ascribed to the asymmetry of the structure, since the drift

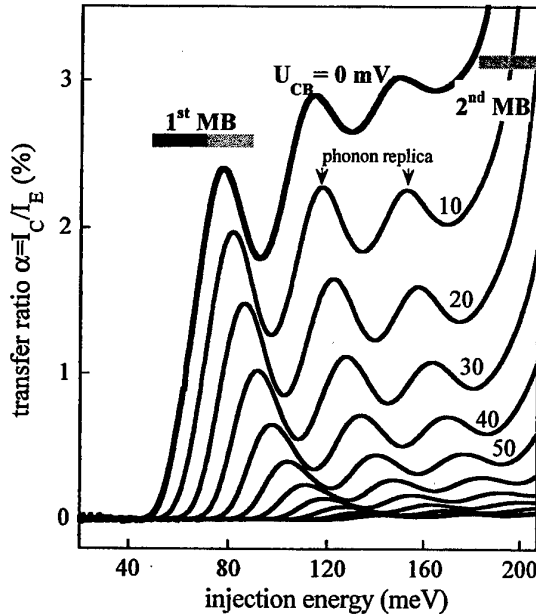


Figure 15: Transfer ratio versus injection energy at different negative applied collector base voltages. The dark bar indicates the calculated position of the miniband. The gray bar represent the full width at half maximum of the injected hot electron energy distribution.

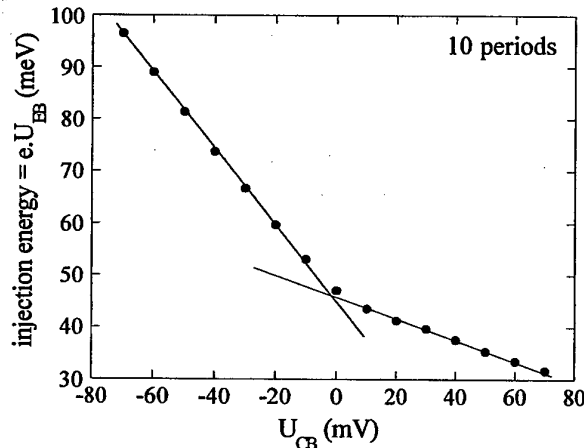


Figure 16: 10 % onset of the transfer ratio versus collector base bias. The crosspoint of the linear fits defines the zero voltage situation.

regions on each side of the superlattice are of different lengths. Comparing the slopes of the theoretical derived onsets to the slopes of the measured onsets gives an accurate relation between applied collector bias to the voltage drop across the superlattice and therefore of the superlattice electric field. Furthermore the extrapolation of the two slopes to the crossing point identifies the flat band condition with high accuracy as well.

The total miniband transmission (T_c) which is defined as twice the area of the lower energy side of the first transfer ratio peak is taken as a measure for the average current

through the first miniband at given bias condition. The current above the first maximum is influenced by the first LO-phonon replica and, thus, not used for the determination of T_α .

Figure 17 shows the total miniband transmission versus electric field of the ten period superlattice. It can be seen that the transmission vanishes for an applied electric field exceeding 4.5 kV/cm. For lower electric fields the superlattice states extend successively one after the other over the entire superlattice dimension and become transparent which leads to an increase of current. At zero bias all superlattice states are extended, leading to a maximum of the measured transmission.

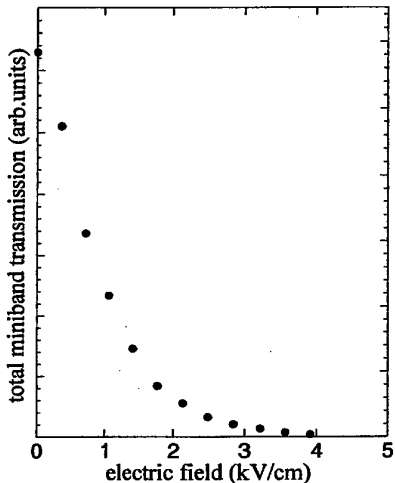


Figure 17: Measured total miniband transmission versus applied electric field of the ten period superlattice sample.

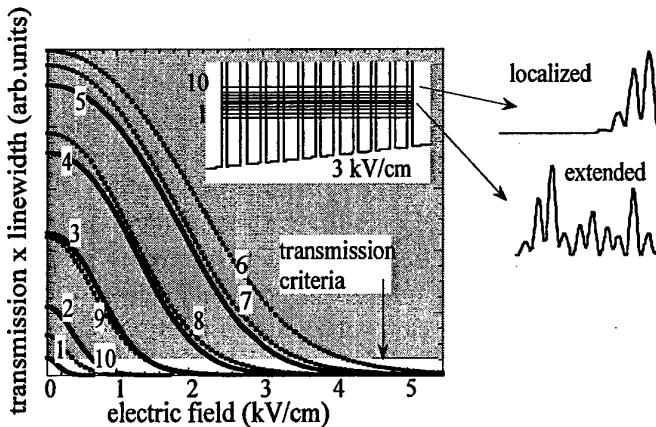


Figure 18: Calculated miniband transmission times linewidth of each single superlattice state versus electric field for a ten period 6.5 nm GaAs/2.5 nm AlGaAs superlattice.

Based on the transfer matrix method using an envelope function approximation, the transmission times linewidth of each superlattice state is calculated as a function of the electric field. This value is considered to be proportional to the current through a discrete subband state. In Figure 18 the transmission times linewidth is plotted for each single state

versus electric field. It can be seen that the lowest and uppermost superlattice states (indicated by 1 and 10) fall under a certain transmission criteria, which is basically defined by the resolution of the experiment, at very low electric fields. The situation at 3 kV/cm is sketched in the inset of Figure 18. While the electron wave functions of the lower and uppermost states are already localized, the center states are still extended over the total dimension of the superlattice. Thus coherent electron transport through these states is possible, while electrons injected into localized states will be reflected by the superlattice.

Transition between Coherent and Incoherent Miniband Transport

The transmission of superlattices with increasing number of periods is measured systematically as a function of superlattice bias. For a short period superlattice the transmittance is found to be independent of the direction of the electric field. For superlattices larger than the coherence length, the transmission becomes asymmetric and dependent on the electric field direction. The onset of scattering induced miniband transport is clearly evident. The coherence length and the scattering time could be determined in the experiments. Furthermore, the scattering mechanism limiting the coherence length of a ballistically injected hot electron could be identified as interface roughness scattering.

In the experiments five samples with superlattices consisting of either 5 (g350), 10 (g338), 15 (g339), 20 (g352), and 30 (g353) were grown in a series in order to investigate the transmission of samples with comparable growth conditions. However, the ten period sample was grown twice under different growth conditions. The static transfer ratio is measured at 4.2 K in a common base configuration.

The measured transfer ratio of the samples are shown in Figure 19 after subtracting the leakage current between base and collector for different collector base biases (U_{CB}) for U_{CB} steps of 10 mV. No collector current is observed up to the first transparent state of the lower miniband. The black solid line again indicates the transfer ratio at flat band condition ($U_{CB}=0$).

A clear shift of the maximum (due to the voltage drop in the drift region) and a reduction of the amplitude is observed for negative collector bias. After a first increase a significant lower reduction of the amplitude is observed for increasing positive collector biases for all samples except for the five period superlattice. For this sample the maximum amplitude of the transfer ratio is measured under flat band condition. Again, the slopes of the emitter-base (U_{EB}) bias of the 10 % onsets of the transfer versus collector-base (U_{CB}) bias are evaluated and extrapolated to the cross point in order to identify the flat band condition for each sample. It turns out that the difference between the voltage corresponding to the flat band condition and the applied superlattice voltage is less than 2 mV. However, it is taken into account in our evaluation procedure.

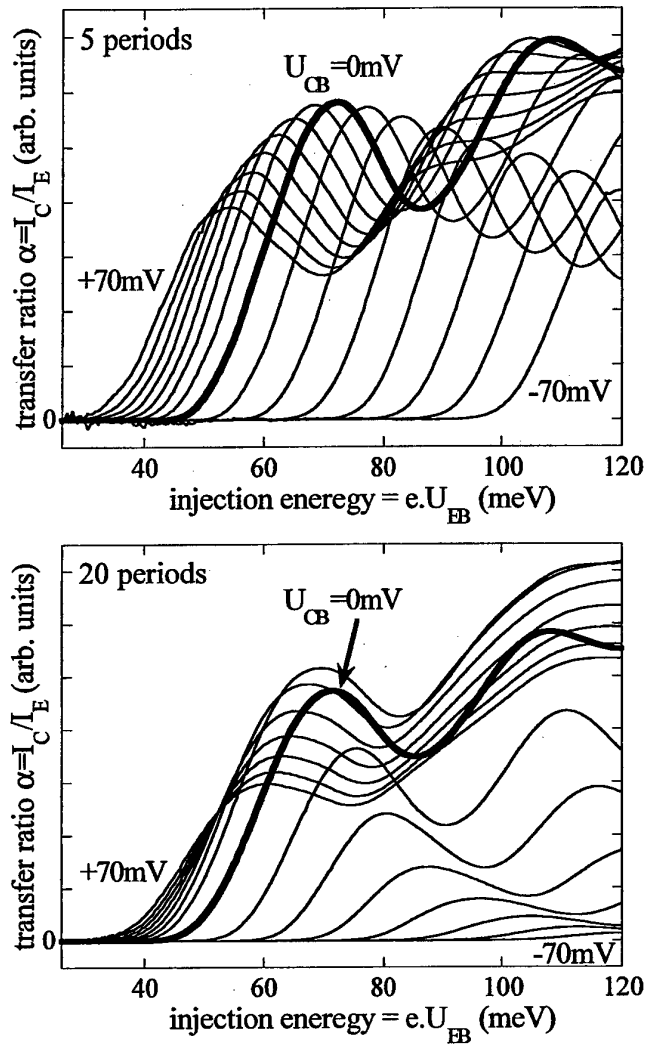


Figure 19: Measured transfer ratio α versus injection energy at different collector base voltages (U_{CB}) of the 5 period (a) and of the 20 period (b) sample for U_{CB} steps of 10 mV. The solid black line represents the transfer ratio under flat band condition ($U_{CB} = 0$).

The analysis of the total miniband transmission T_α of the five period sample is shown in Figure 20 over the voltage applied to the superlattice. The measured transmission is symmetric for both bias directions. In order to compare our experimental data to theory a calculation of the transmission is performed considering a one dimensional ideal structure with nominal sample parameters. The calculation of the transmission is based on a transfer matrix method using an envelope function approximation, which also includes non-parabolicity. The result demonstrates again the quenching of the current as a function of the applied electric field. By summing up the contributions to the current for all injection energies we obtain the transmission T_α as shown by a dashed line in Figure 20.

The calculated curve is symmetric with respect to the field direction as quenching of the Wannier-Stark states only depends on the absolute value of the electric field. This

calculation agrees quite well with the experiment for the five period superlattice (dots), demonstrating that the transport is dominated by coherent transmission. For voltages higher than 20 mV a deviation from the calculated transmission is observed. The measured current seems to be higher than the calculated coherent current. This can be explained in terms of tunneling of electrons accumulated at the interface between left drift region on the superlattice. The onset is expected at the voltage corresponding to half of the energy gap between the GaAs conduction band and the lower edge of the first miniband (half barrier height). Since the energy gap is 46 meV the onset of this additional current should occur for voltages higher than 23 mV which is clearly evident in the experiment.

However, the picture changes dramatically for samples with more periods. In *Figure 21* the miniband transmission T_α versus superlattice bias is shown for the 20 period sample.

For negative bias (decelerating field) the measured transmission (dots) decays faster with superlattice bias than the five period sample. For positive bias (accelerating field) the transmission first increases due to an additional field induced current and then decreases as well. The observed behavior can be assigned to the onset of diffusive transport. For a longer superlattice only a small fraction of the carriers traverse the structure without scattering. Typically, the scattering process decreases the kinetic electron energy in the transport direction, either by transferring the energy difference to a motion perpendicular to the SL-direction (elastic scattering), or by exciting a phonon (inelastic).

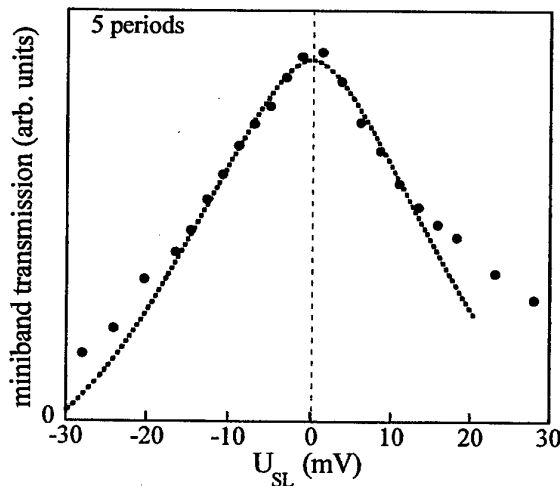


Figure 20: Miniband transmission versus superlattice bias of the 5 period sample (dots). The result of a 1 dimensional calculation based on a transfer matrix method is indicated by a dashed line.

If a positive bias is applied to the collector, an increase of the transfer ratio is observed since the scattered electrons contribute additionally with the coherent electrons to the collector current. Thus in that bias direction we measure the current due to coherent

transport (I_{coherent}) plus the current due to scattered electrons ($I_{\text{diffusive}}$). A schematic drawing of the different contributions to transport for positive bias is shown in *Figure 22*.

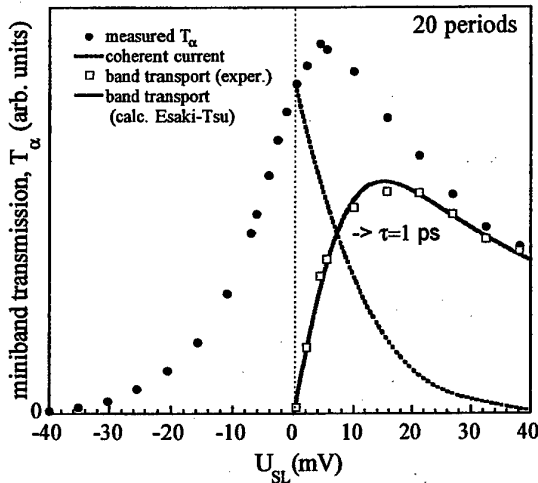


Figure 21: Miniband transmission versus superlattice bias of the 20 period sample (dots). For positive applied bias, the coherent part (dashed line) is subtracted from the data to give the incoherent current (squares). The incoherent current is fitted using the Esaki-Tsu formula (solid line).

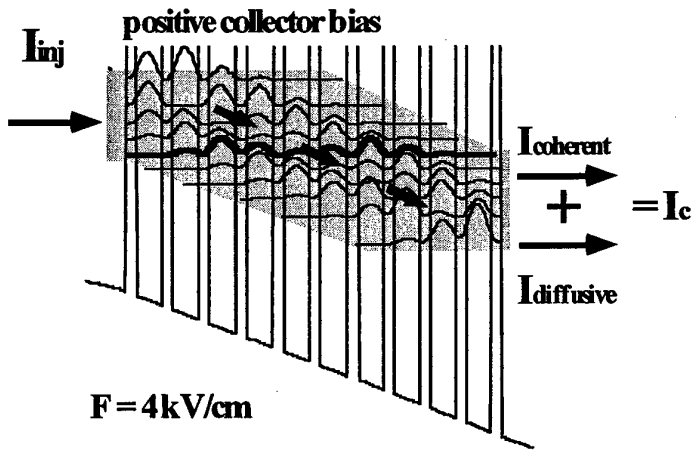


Figure 22: For positive electric fields the measured collector current consists of the diffusive current and the coherent current.

For negative bias only coherent electrons traverse the superlattice since scattered electrons are flowing back to the base according to the applied electric field as shown in Figure 23. Therefore, the scattering destroys the symmetry of the transmission with respect to the field direction.

Following our reasoning given above, the transmission for negative electric fields is mainly due to the fraction of electrons traversing the structure without scattering. This

ballistic part (dashed line in *Figure 21*) is symmetric with respect to the field since coherent transport is independent on the direction of the applied electric field. In order to obtain the current due to scattered electrons, the coherent current can be subtracted from the experimental data for positive superlattice biases as shown in *Figure 21* for the 20 period structure. The difference (open squares) can then be interpreted as the scattering induced current ($I_{\text{diffusive}}$) which is found to be in excellent agreement with the Esaki Tsu [2] model using a scattering time τ_{scatt} of 1 ps. The obtained fit is shown as a solid line in the figure.

The average velocity in the miniband is of the order of $\Delta d/(2\hbar) = 1.5 \times 10^7$ cm/s where d is the superlattice period and Δ the miniband width. This results in a mean free path of $\ell_{\text{coh}} = v\tau_{\text{scatt}} = 150$ nm. This length is significantly larger than the five period superlattice (45nm) in good agreement with the interpretation that ballistic transport dominates for the short structure, while scattering becomes important for the longer superlattices.

The scattering time of 1 ps appears quite reasonable for transport in an undoped superlattice. The coherent transmission time is estimated for the individual Stark state to be 0.6 ps for the five period superlattice which increases to 2.4 ps for the 20 period sample. These times are consistent with the onset of scattering for samples with more than 10 periods.

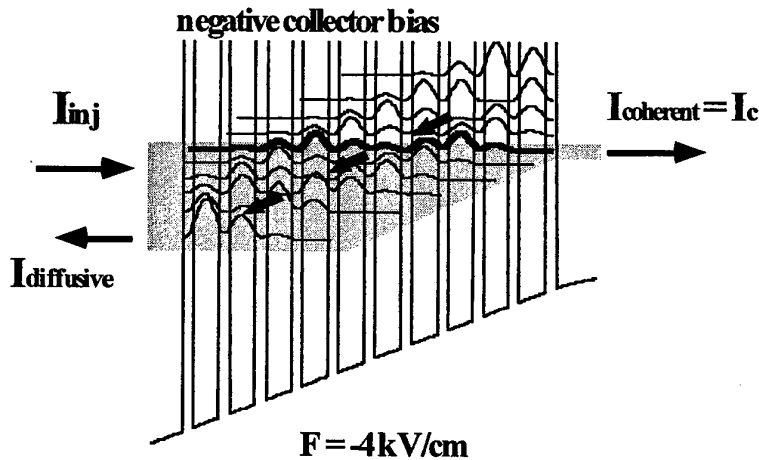


Figure 23: For negative electric fields the collector current is due to coherent electrons tunneling through the superlattice. Scattered electrons are flowing back to the base.

In order to identify the limiting scattering mechanism we have performed a calculation of the transmission through a full three dimensional structure where interface roughness is included. We use typical island sizes of 20 nm and consider a well width fluctuation of one monolayer. The result of this calculation is compared to the experimental data as shown in *Figure 24*. It can be seen that the calculated transmission (solid line) for the 20 period sample becomes asymmetric in excellent agreement with the experimental result (diamonds).

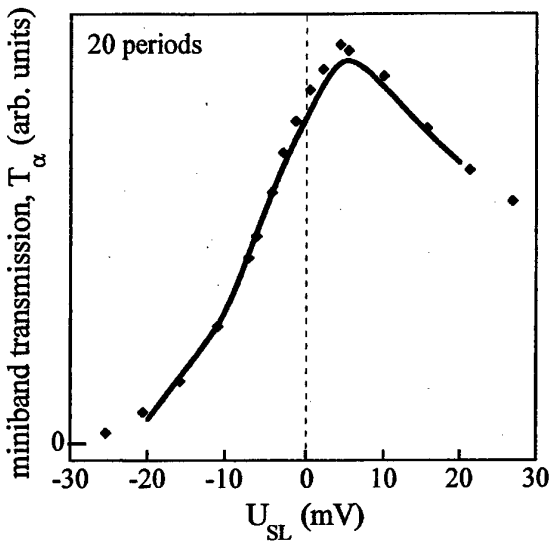


Figure 24: Comparison between the measured miniband transmission of the 20 period sample (diamonds) with the result of a fully three dimensional calculation including interface roughness scattering (solid line).

This clearly demonstrates that scattering by interface roughness induces the asymmetry and can be considered as the main scattering mechanism in these undoped structures at a temperature of 4.2 K.

A comparison of the miniband transmissions of all samples versus applied superlattice voltage is shown in Figure 25. A clear increasing asymmetric behavior for all samples is observed, where the asymmetry is growing with the period number. The experimental curves are shifted for clarity, but cannot be compared directly in absolute terms since the current values for different samples of the same period vary by $\pm 30\%$. The peak value of the measured transmission shifts to higher superlattice voltages for increasing length of the superlattice in agreement to the reasoning given above.

The onset of diffusive transport can be clearly identified between the 5 and 10 period superlattice.

It should be noted that this technique can be used as a universal tool for systematic studies of superlattice transport of periodic heterostructures with varying growth conditions, local doping and bandstructures.

1.7. Quantum Wire devices

Semiconductor quantum wires are lagging behind in device applications. This is mainly due to the fact that the fabrication techniques mainly employed until very recently do not provide sufficient quality and reproducibility of the quasi 1D systems. There are therefore two main interests in the research efforts concentrating on 1D systems. The first aims at the investigation of new fabrication techniques, which are expected to yield nearly defect-free, *truly* one-dimensional electron systems with electrons occupying only the

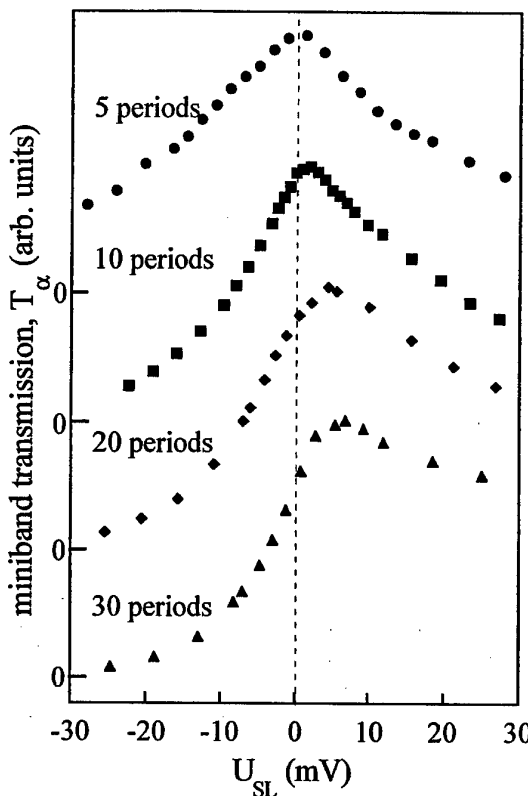


Figure 25: Comparison of the miniband transmission versus superlattice bias of the 5 (dots), 10 (squares), 20 (diamonds), and 30 (triangles) period sample. An increasing asymmetry with increasing superlattice length is clearly evident. All curves is normalized to one at zero superlattice bias

lowest 1D subband. These systems are also interesting from the point of view of basic research, as they will form the testing ground for numerous theoretical predictions on the spectral and transport properties of truly one-dimensional systems [3, 4, 5, 6, 7, 8, 9, 10]. Some progress in this direction has been made recently by the introduction of the cleaved edge overgrowth technique. This technique allows the fabrication of truly 1D ballistic channels with lengths exceeding 10 μm , which are also accessible to transport investigations [11]. In recent transport experiments [12] it is found that the quantization of the conductance in these wires is obviously non-universal, i.e. in units smaller than the universal conductance quantum $2e^2/\hbar$. A number of attempts to explain this observation has been made so far (see, e.g. [13]), indicating interesting effects of the interaction between the 1D channel and the adjacent 2D contacts. Similar results have been reported recently on long ballistic channels fabricated from very high mobility GaAs-AlGaAs material, where the lateral confinement is induced by a combination of deep mesa etching and side gate structures [14, 15].

Also the successful fabrication of up to 1 μm long split gate structures on top of deeply buried high mobility electron gases should be mentioned [16]. The transport experiments

conducted with this device structure showed clear evidence of spin polarized ground state subbands induced by the mutual interactions of 1D electrons [17, 18, 19].

Another very promising path followed in the realization of true 1D systems simultaneously breaks the ground for the future field of *molecular electronics*. It has celebrated its first successes very recently with the investigation of the transport properties on single specimens of multiwalled and also single walled *Carbon nanotubes*. [20, 21, 22, 23, 24]. These macromolecules show unique mechanical and electronic properties [25] and it may be speculated that due to the unique growth properties of Carbon the first functional entities of molecular electronic devices will be investigated soon [26, 27].

From this it becomes clear that the main interest in quantum wire research tends toward single mode devices or at least toward low numbers of occupied 1D subbands. An interesting possibility for the practical application of quantum wires is their use as detecting devices in the far infrared spectral range. In order to make quantum wires interesting for this field of application, it will be necessary to focus present research work on single wires with electrically tunable properties.

The present report therefore deals on the one hand with the investigation of a transport method which probes the subband spacing of quantum wires and provides an alternative to the standard magnetic depopulation method in the case of low numbers of occupied subbands. It relies on the observation of the so-called magnetophonon resonance in 1D electron gases and has the additional advantage that it can be carried out at relatively high temperatures (above 77 K). On the other hand another frequently used method of subband spectroscopy will be discussed here, namely tunneling spectroscopy. A new device is introduced, which in a simple and flexible way overcomes the difficulties encountered when independent contacts are to be established to two closely spaced electron gases. In addition, the new device allows to impose an electrostatically tunable confinement on its active region and to study tunneling processes for varying dimensionality of the initial and final states. The results obtained with the various types of quantum wire devices introduced in this report will be briefly discussed with regard to possible applications of quantum wires as far infrared detectors.

1.7.1. Characterization by magnetophonon spectroscopy

In 1961 Gurevich and Firsov [28] discovered that in polar semiconductors the quantization into Landau levels (LLs) at high magnetic fields should lead to resonant LO phonon scattering of electrons between these equidistant Landau levels. As the LO phonons are assumed to be dispersionless in the interesting k-space region, resonant scattering between Landau levels is expected whenever the phonon energy equals an integral multiple of the LL energy spacing:

$$\hbar\omega_{LO} = N\hbar\omega_c$$

This so called magnetophonon effect has been shown to result in an oscillatory behavior of the magnetoresistance at temperatures high enough to ensure a sufficient population of the phonon states (usually at $T \geq 100$ K). Since then magnetophonon

resonances (MPRs) have been observed in a variety of semiconductor systems (for a review of the work until 1975, see Ref. [29]). In the bulk, the observation of MPR has become a standard method for the determination of effective masses [30], [31] and proved to be a useful tool for the investigation of the conduction band nonparabolicity in binary compounds up to 400 K [32], [33]. Since the first magnetophonon experiment carried out on 2D systems [34], a wealth of phenomena could be studied in 2D electron gases using the magnetophonon effect. Besides the determination of effective masses, an important subject of investigation thereby was the influence of the reduced dimensionality on the electron phonon interaction. For example, from a combination of cyclotron resonance and magnetophonon resonance measurements on GaAs-AlGaAs heterojunctions it has been found [35], [36] that the dominant interaction of the confined electrons is not with bulk LO phonons. By taking the effective mass values from cyclotron resonance measurements, the frequency of the effective phonons can be extracted from MPR data and is found to be around 282 cm^{-1} , i.e. situated between the bulk LO (296.4 cm^{-1}) and TO (273.2 cm^{-1}) frequencies of GaAs. In the work cited above therefore an interface phonon is made responsible for the magnetophonon effect in 2DEGs

Using high mobility GaAs-AlGaAs heterostructures, Leadley et al. [37] investigate the dependence of the MPR oscillation amplitude on the spacer layer thickness. A fully self consistent incorporation of *all* scattering mechanisms including acoustic phonon and impurity scattering [38] reproduces their experimental findings in great detail and also correctly predicts the experimentally observed collapse of MPR at very high magnetic fields [37].

As discussed previously, in quantum wires the energy spacing of magnetoelectric hybrid levels does not only depend on the magnetic field strength, but also on the zero field 1D subband spacing. If, for example, parabolic confinement is assumed, the energy levels are calculated according to $E_n(B) = \hbar\omega = \hbar\sqrt{\omega_c^2 + \omega_0^2}(n+1/2)$. This leads to a modification of the magnetophonon resonance condition (1.1) where now $\hbar\omega$ has to be used instead of $\hbar\omega_c$. As a consequence, the magnetic field positions of the magnetophonon resonances should be shifted to slightly lower fields compared to the 2D case. Since this shift depends on the subband energy $\hbar\omega_0$, it is expected that MPR can be used for subband spectroscopy of 1D quantum channels.

A first investigation along this direction [39], however, has given only ambiguous results on the 1D subband spacing. Though it was possible to detect a weak magnetophonon signal in an array of several hundred quantum wires, the obtained $\hbar\omega_0$ was found to exceed the corresponding magnetic depopulation value by a factor up to 2.5.

Magnetophonon effect in quantum wires: experimental results

The experiments on the magnetophonon effect in 1D electron systems were conducted on three different modulation doped GaAs-AlGaAs heterojunctions, in the following referred to as g73, g79 and g166. The confinement scheme chosen for the present investigation is the shallow etching method. This method has been chosen despite its (numerous) disadvantages because it is simple to implement and because the investigation of single split gate structures, fabricated by electron beam lithography, has not proved to be more advantageous. In order to obtain a magnetophonon signal of reasonable amplitude and resolution it is favorable to reduce the influence of all scattering mechanisms other than phonon scattering as far as possible. Therefore the main results are obtained for samples of the type g166. This heterostructure has a relatively large spacer layer combined with relatively "low" integral doping ($< 2 \times 10^{18} \text{ cm}^{-3}$). This layout has a twofold purpose: First, it is intended to reduce the influence of remote impurity scattering on the magnetophonon signal. And second, the corresponding low electron density in the 2D channel makes it possible to achieve appreciable lateral confinement by only slightly "scratching" the surface. It is hoped and, of course, there is some experimental evidence, that this will reduce the additional scattering by the surface defects induced by the shallow etching process. The heterostructures g73 and g79 have larger electron densities and consequently require deeper etching in order to confine the electron gas into narrow channels. They were found to give insufficient resolution of the magnetophonon oscillations and were only used for comparative studies.

The chosen sample layout is shown in Figure 26. It consists of a simple two-terminal device structure where the quantum wires, fabricated by laser holography and subsequent wet chemical etching, extend between two large Ohmic contacts. Although it is easy to fabricate four-terminal device structures with the wires located between two extra voltage probes, the two-probe design has been chosen due to its endearing simplicity. With this design, of course, one has to take into account the contact resistance and its magnetic field dependence. However, by a proper processing this contact resistance can be made small as compared to the relatively large low temperature source-drain resistance (at least several kilohms) of the wire array. The dimensions of the mesa or wire array ($200 \times 20 \mu\text{m}^2$) were chosen with regard of the experiences made earlier with very large arrays (several hundred quantum channels in parallel investigated e.g. in Refs. [40], [41], [42]). The shallow etching method induces significant inhomogeneities of the wire quality over the array. For large arrays this may corrupt the experimental results, especially when a small resistance oscillation, buried in a large background, is to be resolved. The period of the holographic grating has been chosen to be 475 nm in all cases, which leads together with the mesa width to an array of about 40 wires in parallel. This assures an easily accessible signal without inducing serious inhomogeneities in the signals of individual wires.

In the experiments, the electron density in the wire devices was varied by illuminating the wires with a red light emitting diode and by temperature cycling. Details of the experimental procedure can be found in refs. [43] and [44]. Figure 27 shows some typical data for sample g166/1. Here, the first derivative of the high temperature

magnetoresistance is plotted as a function of the magnetic field strength B , measured after various temperature cycles, labeled #1 - #5. Each trace corresponds to a different electron density in the wire array.

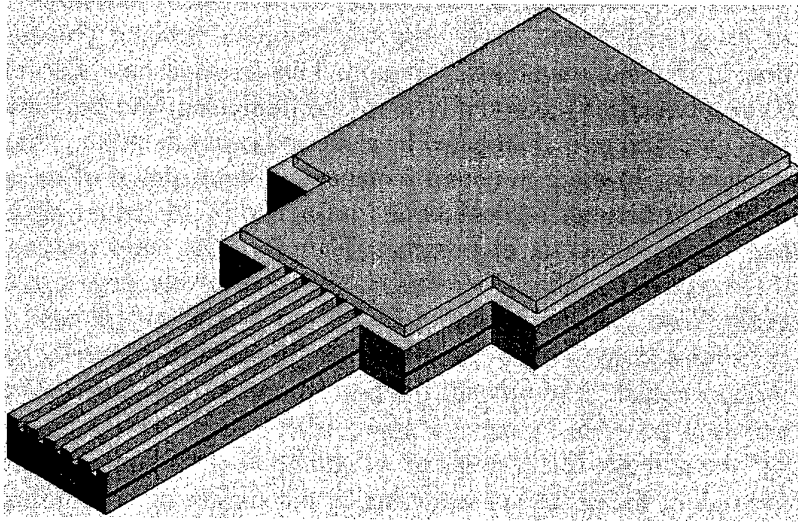


Figure 26: Schematic cut through the two terminal wire device. The dimensions of the drawing are not to scale. The mesa extending between the two large Ohmic contacts ($300 \times 300 \mu\text{m}^2$) is $20 \mu\text{m}$ wide and $200 \mu\text{m}$ long. On its top an array of approximately 40 parallel quantum wires is fabricated by laser holography and shallow etching. The thick solid line symbolizes the position of the 2DEG.

In Figure 28 the oscillatory parts of $R_{xx}(B)$ are compared for samples g166/1 and g166/8. The carrier densities in the wires are approximately equal for the two curves. The oscillatory parts $R_{osc}(B)$ were obtained after subtraction of the monotonous background resistance from the $R_{xx}(B)$ curves.

An interesting feature of the oscillatory component R_{osc} are the large variations of the oscillation amplitudes for the various samples. As seen in the figure, the amplitude of R_{osc} is in the case of g166/1 almost an order of magnitude smaller than for g166/8, even if comparable electron densities are present in the wires.

It turns out that the positions of the extrema in R_{osc} can be analyzed in terms of a simple parabolic model. Here the magnetic field dependence of the one-dimensional magnetoelectric hybrid levels is given by the simple relation $(\hbar\omega_{eff})^2 = (\hbar\omega_c)^2 + E_0^2$, E_0 being the 1D subband spacing and ω_c the cyclotron frequency. Within this model the magnetic field positions (squared) of the resonant extrema of R_{osc} depend linearly on the inverse index N (squared) [43, 44]. An example of this is shown in Figure 30 for sample g166/1. In principle, both samples are expected to represent the weak confinement case. That is, when the resonance condition is matched, one should observe a resonant minimum in R_{osc} for both samples. It turns out that this is correct for sample g166/8, which according to the sample processing parameters is more weakly confined than g166/1. For g166/1, however,

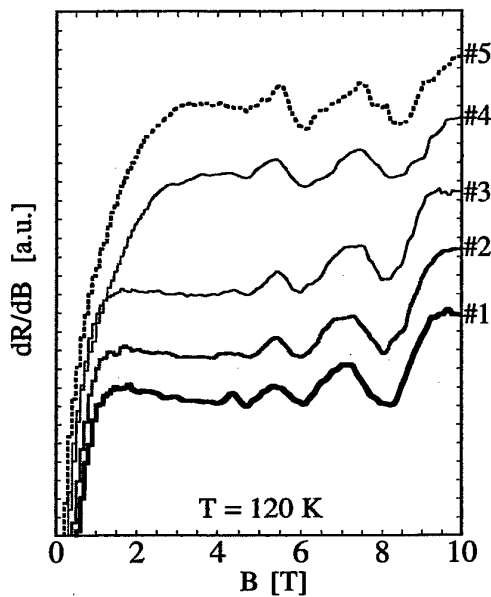


Figure 27: Numerical derivative of the high temperature magnetoresistance obtained for g166/1 at $T = 120$ K. The raw data were smoothed by a 6% weighted fit before differentiation. The labels indicate the corresponding temperature cycle.

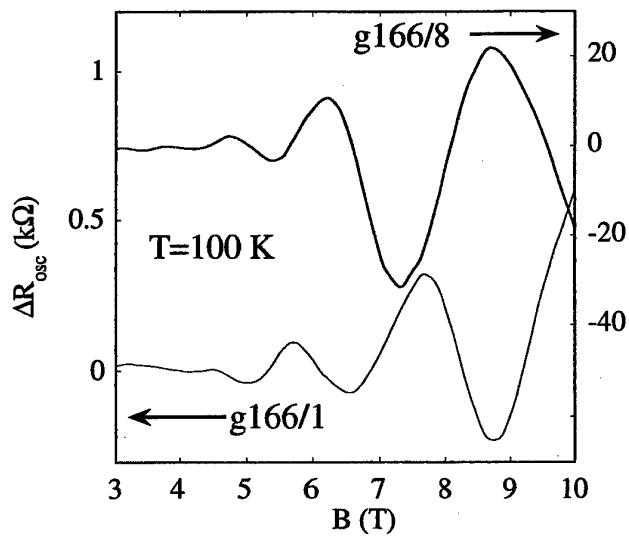


Figure 28: Comparison of the oscillatory part of R_{xx} for g166/1 and g166/8 at $T = 100$ K and comparable electron density. The background resistance has been subtracted according to the method described in the text. Note the different y-axis scales valid for the two curves.

this treatment gives effective mass values that are unrealistically high (order $0.09 m_e$). Since there is no reasonable explanation for a mass enhancement of this order of magnitude, one has to resort to a different picture in the case of g166/1. A clue can be obtained by inspecting once more R_{osc} , compared for the two samples in Figure 28. There is not only a considerably smaller amplitude observed for g166/1 but also an overall “phase-shift” of the oscillatory part of R_{xx} .

This leads us to consider an intriguing possibility which could remove the discrepancy in the mass values and explain why there is such a strong reduction of the oscillation amplitude for g166/1 that is not accompanied by a significant level broadening. To this purpose we recall the theoretical considerations of Mori et al. [45]. Their model emphasizes the importance of the skipping orbit motion in a laterally confined system and predicts that the corresponding contribution to the magnetoresistance should begin to dominate as the confinement exceeds a certain strength. This should lead to a significant qualitative change in the features of R_{osc} insofar as *maxima* of the resistance should occur at resonance where for weak confinement minima are observed. This crossover is depicted in Figure 29, showing the results of calculations analogous to those reproduced in [45].

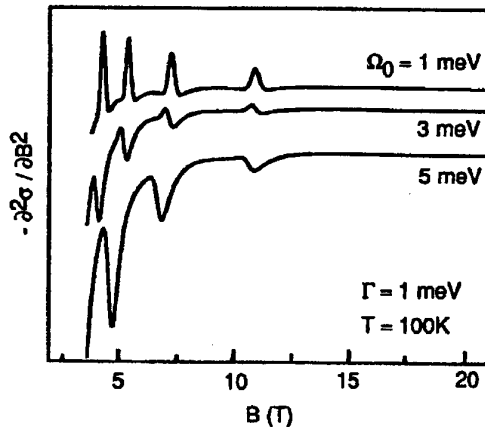


Figure 29: Second derivative of the magnetoconductivity calculated from the model of Mori et al. [45]. The calculation is repeated for three different values of the confinement strength (measured in harmonic oscillator energies): weak (1 meV), intermediate (3 meV) and strong (5 meV) confinement. At intermediate confinement a crossover from resonant minima to resonant maxima in the conductivity is observed. The width Γ of the magnetoelectric hybrid levels is assumed to be magnetic field independent. Taken from Ref [40].

Here, the second derivative of the magnetoconductivity (multiplied by -1) is plotted according to the model of Mori et al. for three different confining frequencies of the underlying parabolic model potential. As seen in the Figure, a crossover between minima and maxima occurs due to the competition of the contributions of skipping orbit and hopping motion in the wire. Near the crossover point, where σ_{po} just begins to dominate

σ_{e-ph} the resulting oscillation has resonant minima. Since σ_{po} at this point does not yet greatly dominate over σ_{e-ph} the oscillation amplitude of the sum $\sigma_{po} + \sigma_{e-ph}$ is small. As the contribution of σ_{po} grows with increasing confinement strength so does the oscillation amplitude. (Note that Figure 29 displays $-d^2\sigma/dB^2$. A minimum therefore corresponds to a minimum in σ itself and hence to a maximum in R_{osc}).

If it is then that g166/1 represents a sample where just such a crossover occurs, this would explain the reduction of the amplitude of R_{osc} without considerable enhancement of its width. And it could as well explain the observed “phase shift”. Having noted this, one might determine the position of the maxima in R_{osc} from the derivatives plotted in Figure 27 and repeat the foregoing analysis with the resulting data. As can be seen from Figure 30, again the simple parabolic model perfectly fits to the data points.

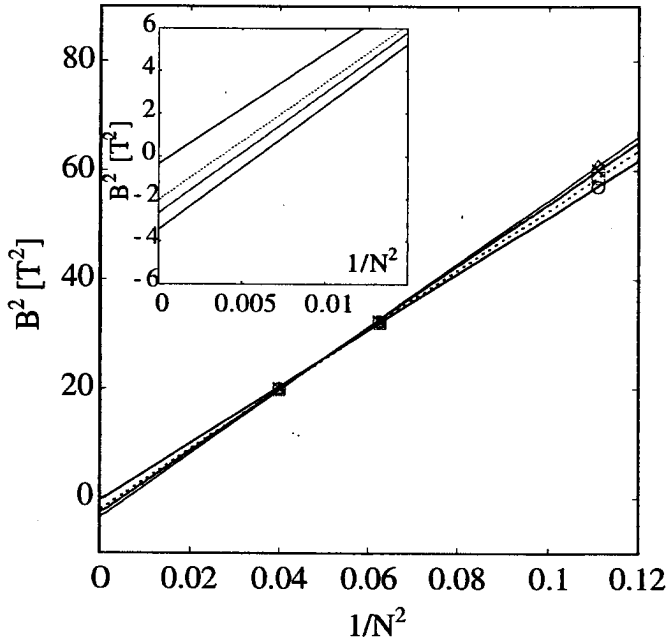


Figure 30: The squared magnetic field position of the maxima of the magnetoresistance oscillation observed for g166/1. The data points were obtained from the derivatives plotted in Figure 27 and correspond to measurements #1 (circles), #2 (squares), #3 (crosses) and #4 (triangles) of this Figure. The straight lines are fitted according to Eq.(4.2). The inset shows a close up of the fitted curves near $1/N^2=0$. The lowest curve corresponds to measurement #4, the uppermost to measurement #1. For measurement #6 the magnetophonon oscillations are not resolved with sufficient accuracy in order to extract three or more oscillation minima.

The close-up of the fitted lines near $1/N^2=0$ again shows the systematic increase of the intersection with the ordinate axis as the electron density is reduced. It turns out that now the discrepancy of the resulting mass values is removed. The latter are found to lie close to $(0.075 \pm 0.03)m_e$.

In Figure 31 the extracted subband spacings are shown as a function of the one-dimensional electron density in the wires. This is the central result of this chapter. The details of how the 1D densities can be estimated from the magnetic depopulation measurements are explained in detail in ref. [43]. The subband spacing is seen in all cases to grow as the density is reduced, i.e. as the number of temperature cycles is increased. Also shown in the figure are the values of the subband spacing that could be obtained from magnetic depopulation measurements on g166/8. For g166/1 no such low-temperature data are available because of the lack of oscillatory structure in the corresponding magnetoresistance traces. Figure 31 clearly shows how the magnetophonon method extends the density range, where subband spectroscopy can be performed, considerably beyond that accessible to magnetic depopulation.

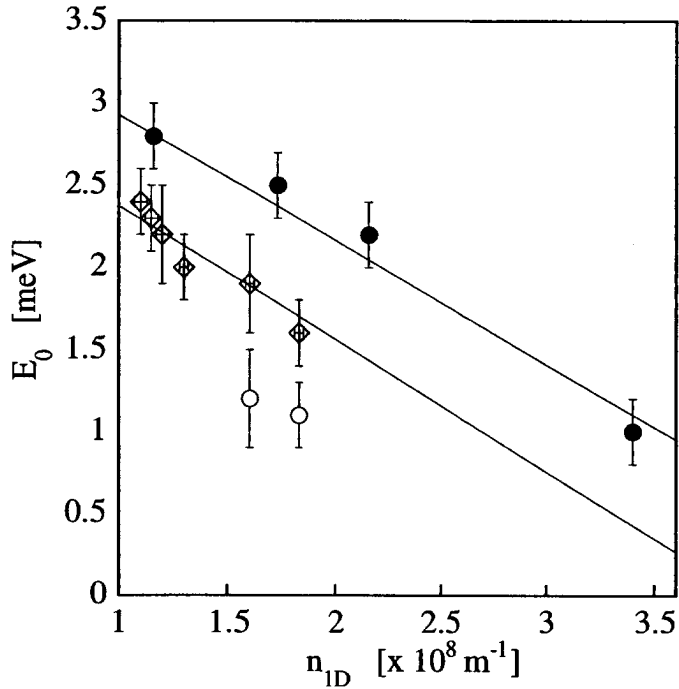


Figure 31: Subband spacing as a function of 1D electron density for samples g166/1 (solid circles) and g166/8 (open diamonds). Open circles mark those subband spacings of g166/8 that could be obtained from magnetic depopulation data. The solid straight lines are from a free linear fit to the experimental points and are only guides to the eye.

The subband spacing is seen to increase as the density of free carriers in the wires decreases. This is what has been predicted from self consistent calculations [46]. The observed behavior is easily explained qualitatively by noting that the confinement potential has its origin in a periodic modulation of the donor distribution, generated by the shallow etching. The presence of free carriers partially screens out this so called *bare* confinement potential. Consequently the total confinement will be stronger with fewer electrons present in the wire. To test this assertion we have performed magnetic depopulation experiments

on samples of the type g79. The electron density was varied in this case by applying a back gate voltage from the substrate side of the sample. In Figure 31 the subband spacing is plotted as a function of electron density. Both parameters are obtained from the corresponding Landau plots. The same quasi linear increase of E_0 with decreasing N_{1D}^e as in Figure 31 is observed.

The observed differences between subband spacings that were obtained from magnetophonon measurements and those obtained from magnetic depopulation experiments (cf. Figure 31) are due to the fact that the electrostatic confinement of shallow etched wires is not exactly parabolic but rather of a sinusoidal shape.

To summarize these considerations, one may state that magnetic depopulation experiments always probe the subband energies at the Fermi energy, whereas magnetophonon resonance experiments are sensitive to the sublevels near the bottom of the confinement potential. This not only explains the experimentally observed difference between the energy values extracted by the two methods. It also shows that the combination of the two methods provides in a simple manner direct information on the actual shape of the underlying confinement potential, in that it allows to decide immediately if the potential is cosine or square well like. The latter case represents a situation that is in a sense invert to the sinus potential: here, the upper levels have a somewhat greater energetic spacing than the low lying ones.

In summary, the magnetophonon effect could be successfully applied to characterize shallow etched quantum wires. This has been achieved for electron densities so low that the corresponding information could no longer be obtained from magnetic depopulation experiments. Clear evidence has been found for the first time that a crossover occurs in the magnetophonon resonant oscillation of the resistance when the influence of the lateral confinement begins to dominate the magnetotransport properties at high temperatures. However, the subband spacings of the two samples under investigation differ by not more than 1 meV. It is therefore somewhat surprising that the two wire arrays behave qualitatively different. This might be an indication that there are additional factors which make the transition to a magnetophonon effect that is dominated by skipping orbit motion less smooth than it is suggested by the theoretical model.

Significant differences between the subband spacings were found depending on whether they are determined by low temperature or high temperature methods. We propose a model that is capable to explain the observed differences. It relies on the fact that the actual potential shape of shallow etched wires is sinusoidal instead of parabolic. The simulation of magnetophonon resonance experiments for wires with different confinement potential suggests that from a comparison of high- and low-temperature transport experiments one obtains qualitative information on the shape of the confinement potential.

The results presented in this section and in particular those on the behavior of the 1D subband spacing as a function of the carrier density are also interesting with respect to the use of quantum wires as tunable photoconductive detectors. This is because they indicate a particularly simple way to tune the sublevel energies of a quantum wire within a certain range by simply varying its carrier density. This could be done, for example, with back or front gates on the active region of the wire device.

1.7.2. Vertical tunneling through tunable quantum wires

Recently, several tunneling spectroscopic investigations of various spectral properties of two- and one-dimensional electron gases have been reported [47, 48, 49, 50, 51, 52]. Once the technological difficulties encountered in the fabrication of tunneling devices are overcome, this type of spectroscopy is a powerful and productive source of deep insight into the electronic properties of low dimensional electron states. For example, the dependence of the tunneling current on the spectral density function [53] of the involved electron states [49, 50] allows to study scattering processes in great detail. On the other hand, the matrix elements of the tunneling transitions are found to be proportional to the overlap integrals of the initial and final wave functions [54]. This gives direct access to various spectral features that are directly related to the shape of the wave functions. For example, magnetotunneling spectroscopy has been used to investigate the band structure of 1D lateral surface superlattices [51] as well as the detailed shape of the lateral 1D confinement potential [52]. A particularly impressive result of magnetotunneling spectroscopy is the direct measurement of the Fourier transform of 1D wave functions [48], [52].

In all these investigations the major difficulty in device fabrication has been the formation of independent Ohmic contacts to two electron gases separated by a barrier of only several hundred Å thickness. Two successful schemes to achieve this have been demonstrated in the mentioned tunneling studies. The first [50, 51, 52, 55] is an improvement of Eisenstein's selective depletion technique [56]. It is implemented by growing a highly doped back gate layer into the wafer structure, which is *in situ* patterned by focused ion beam lithography and subsequently overgrown with the actual active structure, namely two barrier separated quantum wells. By locally depleting the upper electron channel with a conventional Schottky gate on the sample surface and the lower channel with an *in situ* patterned backgate one achieves independent Ohmic contacts to the two 2DEGs. The second scheme [47, 48, 57] relies on a sequence of selective and anisotropic etch steps performed on a double barrier resonant tunneling (DBRTD) structure. This results in two crossed GaAs bars, of which the upper forms a narrow, free standing bridge to a separate set of Ohmic contacts. By giving the upper bridge a submicron width, one achieves a situation where tunneling occurs between two tightly confined 1DEGs. The confinement strength can be adjusted only by etching a sufficiently narrow bridge.

Both these methods are highly sophisticated and require the availability of *in situ* FIB equipment in the first case or an exact control over complicated etching steps in the second case, which in addition seems to be restricted to DBRTD structures. We demonstrate here a new, simple and flexible way of establishing independent Ohmic contacts to two barrier separated 2DEGs, using self aligned side gates. In addition, the same technique is shown to be suitable to impose an electrostatically tunable lateral confinement to the active region of

the tunneling device. This can be achieved by conventional photolithographic steps without the necessity to control extremely sensitive etching steps.

Sample layout

Figure 32 shows the layout of the side gated tunneling device. The active region of the device consists of a 20 μm long bar shaped mesa with a width ranging from 0.9 μm up to 1.4 μm . This part of the device is connected to two large Ohmic contacts which simultaneously contact the two electron channels. The upper channel can be separated from one of the Ohmic contacts by a top Schottky gate, which selectively depletes the upper channel beneath the gate region. On the opposite side of the active region a thin side gate is positioned. The width of the mesa is chosen so that a negative voltage applied to the side gate depletes the electron gases near the gate. If the mesa depth is sufficiently large and the side gate metallization is only thin, the side gates will be situated closer to the lower channel and the electric field produced by the negative voltage will be partially screened by the doped barrier. This means that, using this gate geometry, one can achieve a situation where the lower channel is completely depleted and thus separated from the corresponding Ohmic contact while the upper channel is still conducting. The lower part of Figure 36 schematically depicts the situation where the two channels are separated from their corresponding contacts. Thereby a situation is established where current induced via one of the contacts can flow only across the tunnel barrier.

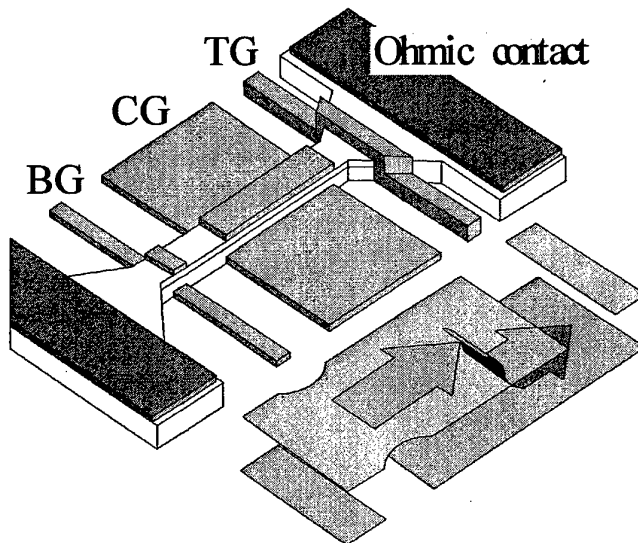


Figure 32: Schematics of the side gated tunneling device. Only the active region is drawn, consisting of a narrow mesa line of length 20 μm and width of order 1 μm . Only a small part of the large ($300 \times 300 \mu\text{m}^2$) contact pads is shown. BG denotes the bottom contact separator, CG the central gate (both fabricated in a self alignment technique). TG is the top contact separator. The bottom part symbolizes the two electron gases in pinch off. The arrow depicts the current path for reverse bias.

The region in between the two gates, where tunneling occurs, can be further modified by placing a second side gate as shown in

Figure 32. This gate can be used to induce a lateral confinement on the two electron channels. Depending on the position and thickness of this central gate, the lateral confinement will be different for the upper or the lower channel. As will be shown in the following subsection, there are two ways of fabricating a side gate geometry by conventional optical lithography. It is possible to manually align a split gate structure around the narrow mesa. With contemporary photolithographic equipment this alignment can be performed with an accuracy of 100 nm or even better. The second possibility takes advantage of the properties of the undercut produced by the wet chemical mesa etch. This undercut is so sharp that a continuous gate pattern can be defined and evaporated. The continuous gate will be interrupted at the mesa edges, leading to a *self aligned* side gate pattern. The latter method is best suitable if the thickness of the gate metallization is small, i.e. for the fabrication of the bottom contact separator. However, it is found that even if the metallization is of the same order of magnitude as the mesa depth, a continuous gate will be interrupted in most cases. Therefore the self aligning technique is also suitable for the fabrication of the central gate.

For the experiments discussed below the following sample structure, referred to as g228, has been chosen: On a semi-insulating GaAs substrate and a 7500 Å thick GaAs buffer a δ -doped $\text{Al}_x\text{Ga}_{1-x}\text{As}$ ($x=0.32$) barrier has been grown which is followed by an $\text{In}_x\text{Ga}_{1-x}\text{As}$ ($x=0.15$, strained) quantum well. A nominally undoped GaAs layer and a GaAs cap layer, doped to nominally $2 \times 10^{18} \text{ cm}^{-3}$ complete the structure. The carrier densities in the two electron channels have been determined to be $6.1 \times 10^{11} \text{ cm}^{-2}$ in the InGaAs well and $3.1 \times 10^{11} \text{ cm}^{-2}$ in the GaAs-AlGaAs heterojunction. Details of the sample characterization leading to these values are given in Appendix A. There is also given a self consistently calculated conduction band profile together with the energy levels in the two channels.

The choice of an InGaAs well as the upper electron channel has its reason in the fact that it is difficult to achieve a sufficiently high doping concentration in the cap and the near-surface GaAs layers in order to obtain an electron density in the upper well which is appreciably larger than that of the lower channel. This is the crucial prerequisite for the side gate selective depletion technique to be applicable.

Details of the fabrication sequence can be found in refs. [44, 58].

2D-2D Tunneling

Figure 33 shows different representations of low temperature current voltage characteristics, obtained for a device with a lithographic width of the uppermost mesa edge of $1\mu\text{m}$. In Figure 33 (a) a typical $I(V_b)$ curve is plotted together with the conductance $G = I/V_b$. The latter representation of the data reveals more clearly the peak structure in the $I(V_b)$ characteristics. The gate voltages necessary for pinching off the corresponding

electron channel were $V_{TG} = -1.27$ V and $V_{BG} = -0.78$ V, respectively. The central gate voltage for these curves is $V_{CG} = 0$ V. We attribute the structure seen in the various curves to resonant tunneling between the energy levels of the upper and lower electron gases, which for zero central gate voltage are of a 2D nature. Negative V_b corresponds to tunneling from the InGaAs well into the lower 2DEG, positive V_b to the reverse situation.

The first peak at negative bias results from tunneling from the lowest occupied subband in the well into the lowest subband of the GaAs-AlGaAs heterojunction. The broad

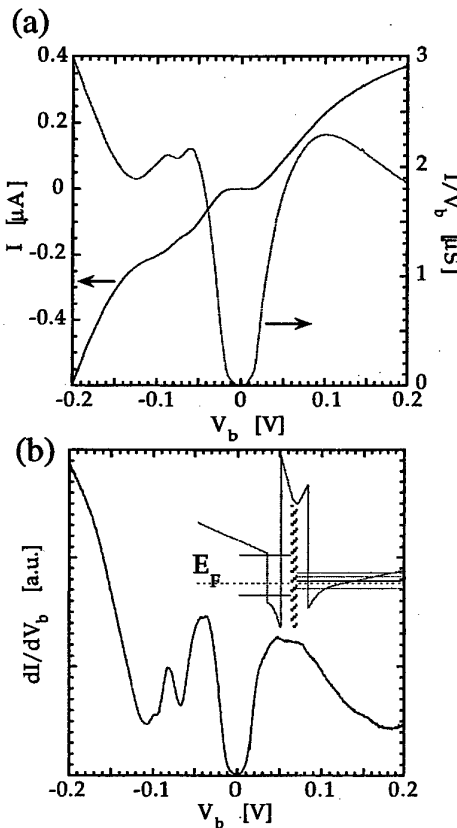


Figure 33: (a) $I(V_b)$ and $G(V_b) = I/V_b$ at $T = 2K$ plotted for sample g228/6 D3 for a central gate voltage $V_{CG} = 0V$. (b) Differential conductance dI/dV_b for the same sample obtained by standard ac lock-in techniques with an excitation frequency of 126 Hz and a modulation amplitude of 1 mV. The inset shows the conduction band profile and some of the energy levels in the two wells.

peak observed for forward bias is due to tunneling from the lowest subband of the heterojunction into the first excited state of the well. As a consequence of the two terminal layout of the device, the voltage drop across the tunneling barrier is not the same as the

applied V^1 . V_b rather has to be scaled with an appropriately determined factor α . To estimate α we first note that the calculated energy difference between the ground state and the first excited state in the InGaAs well is approximately 80 meV. This corresponds to the measured V_b difference between the two main peaks in forward and reverse direction, respectively, which is about 160 mV. From this we obtain a scaling factor of 2 between the voltage drop across the barrier and the corresponding V_b . This value is confirmed by measurements in a perpendicular magnetic field. Here the main resonances split into a series of peaks corresponding to inter Landau level (LL) tunneling. From the known energy splitting of the LLs involved in the tunneling, we estimate α to be close to 2, in excellent agreement with the previous value. With this scaling factor, the energy difference corresponding to the first and second peak on the negative bias side is about 14 meV, which agrees very well with the calculated energy difference between the lowest and the first excited subband in the heterojunction (15.4 meV). Tunneling into the second excited subband of the lower channel leads to a resonance structure that is greatly reduced in amplitude. It is resolved as a weak shoulder in the derivative of the tunnel current (cf. Figure 33 (b)).

A disadvantage of the chosen sample structure (with a doped barrier separating the two electron gases) is that it leads to a considerable broadening of the resonances in the tunneling current. From a fit of the peak current (obtained after subtraction of the non-resonant background) to a model that assigns a Gauss line profile to each tunneling resonance it can be shown that the linewidth is of the order of 8 meV in zero magnetic fields and somewhat smaller in non-zero magnetic fields (about 4.5 meV). The main reason for this line broadening is the δ -doping of the barrier. The resulting imperfections of the barrier lead to elastic scattering of tunneling particles. As a consequence, also off-resonant particles (i.e. particles that do not perfectly satisfy the condition of simultaneous conservation of energy and momentum) are allowed to tunnel through the barrier, which leads to a broadening of the bias range where an appreciable tunneling current is measured. The dominant influence of the doped barrier is also seen in the large non-resonant background current observed in the $I(V_b)$ characteristics.

Tuning the dimensionality of the emitter and collector states

This section deals with the behavior of the tunneling characteristics, when the central gate is negatively biased in order to impose an additional lateral confinement on the two electron channels.

The following Figure 34 reproduces the $I(V_b)$ and $G(V_b)$ characteristics, obtained for sample g228/6 D3 at $T = 2$ K for several values of the central gate voltage. Several

¹ Note that there is also a shift of the entire tunnel characteristics to negative bias. This is characteristic for two terminal tunneling experiments when there are series resistances (contact resistances) of a similar order of magnitude as that of the tunneling barrier itself.

interesting features can be seen already in these curves, although the large intrinsic width of the resonant structures does not allow to resolve these in great detail. First, the region of zero conductivity around $V_b = 0$ is seen to broaden. This is accompanied by a broadening of the main resonant peaks in $G(V_b)$ at forward and reverse bias. Second, there is an apparent enhancement of the splitting between the first and second peak on the negative bias side of the $G(V_b)$ curves. The second peak is seen to move towards higher bias voltage and finally to become so broad that it can hardly be resolved. In order to

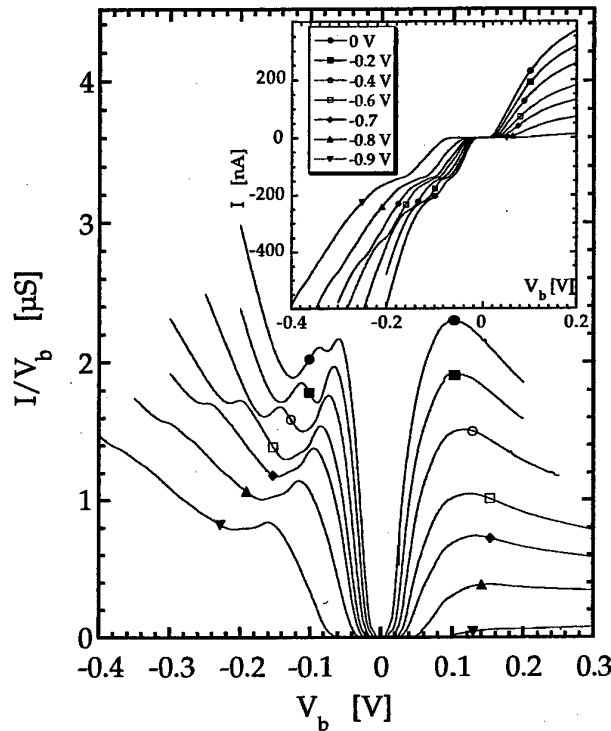


Figure 34: $G(V_b)$ and $I(V_b)$ (inset) curves, obtained at $T = 2$ K for sample g228/6 D3 for various central gate voltages. $G(V_b)$ and $I(V_b)$ curves corresponding to the same central gate voltage are marked by the same symbols.

obtain a clearer picture of what happens, an attempt has been made to subtract the large background current from the I-V and to obtain the bare resonant peak structure. For this purpose the approximately quadratic behavior of the background, observed at the highest reverse bias voltages has been extrapolated over the entire V_b range. Figure 35 shows the normalized peak currents, obtained from the measured $I(V_b)$ after subtraction of the approximate background. It is clear that this crude method will not be able to reproduce the correct absolute values of the peak amplitudes. Therefore and since we are mainly interested in the qualitative behavior of the peak shape, the amplitude of the first resonant peak in each curve has been normalized to unity.

Figure 39 shows that the second peak, which seems so strongly broadened at the highest central gate voltages, actually is split into a series of weak structures. The small

structures in the peak currents are resolved in greater detail in the differential conductance dI/dV_b . A sequence of dI/dV_b traces for sample g228/6 D3 at various central gate voltages is shown in Figure 36.

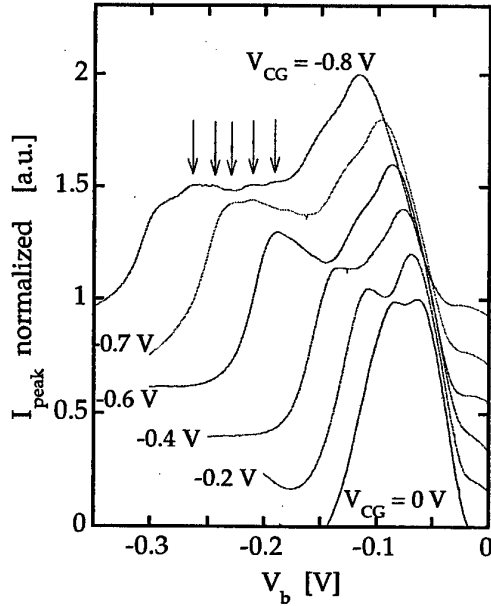


Figure 35: Normalized peak currents of sample g228/6 D3 obtained from the $I(V_b)$ traces of Figure 6.15 after subtraction of the background current. The arrows indicate the weak resonant structure resulting from the 1D quantization of the emitter and collector states. Curves are vertically offset for clarity.

For a proper interpretation of these results two important points have to be taken into account. The first concerns a fact already discussed in the previous section, namely that there are gated and ungated regions of the device, which behave differently when the central gate is biased.

A second point to be made here concerns the effect of the central gate on the two electron channels. As V_{CG} is increased, there are two main effects. First, from magnetic depopulation investigations on single side-gated wires [59] it is known, that there is a considerable reduction of the electron density n_s in the gated regions with increasingly negative V_{CG} . In the case of the tunneling structures under consideration here, this reduction of n_s is expected to occur mainly in the lower channel. The depleting action of the central gate on the upper channel is considerably smaller for several reasons. On the one hand this is due to the geometry of the device, with the central gate being situated somewhat beneath the active region of the structure. There is consequently some screening of the gate field by the doped barrier as well as by the considerably higher carrier density in the upper channel. On the other hand, the presence of the residual metal cap on top of the gated region has another, useful, side-effect. It creates positive image charges on top of

the device which ensure that the carrier density in the upper channel is approximately constant.

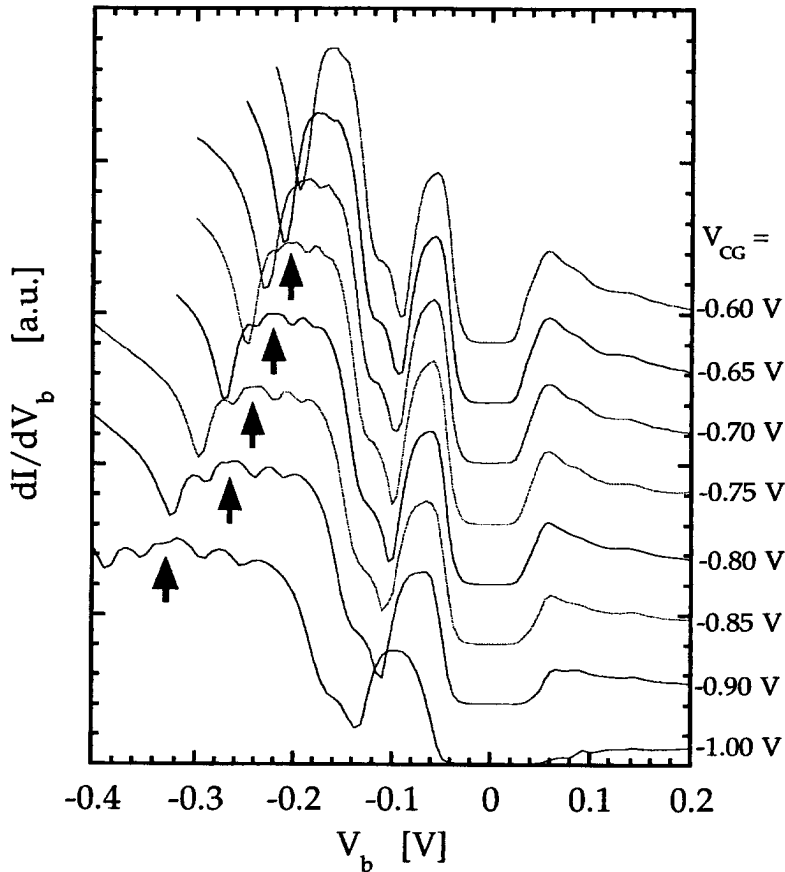


Figure 36: dI/dV_b traces, obtained for g228/6 D3 at $T = 2$ K for various central gate voltages. Curves are vertically offset. The upward arrows indicate those regions of the tunneling characteristics, discussed in the text, where contributions of two different 2D subbands mix.

With this, it is possible to explain the main features of the tunneling characteristics discussed above. In the dI/dV_b sequence shown in Figure 36 the shape of the first peak on the negative bias side is seen to be essentially unchanged over the entire V_{CG} range. There is only a shift of the resonance position to higher bias voltages accompanied by some broadening of the peak. However, this can be entirely attributed to the additional series resistance, which is naturally induced by the central gate. This results in charge build up at the transition region of gated and ungated regions compensating part of the applied bias.

Therefore the V_b necessary to meet the condition for resonant tunneling grows with increasingly negative V_{CG} . As a consequence, the region of zero current at low bias is broadened and the peak positions are shifted towards higher bias voltage. Additional series resistances also change the scaling between the bias voltage and the corresponding

effective voltage drop across the barrier. This, in turn, explains the broadening of the first resonant peak.

In addition to this series resistance effect, which affects the entire tunneling characteristics, there is also a shift of the resonance condition, which affects solely the gated regions. It has its reason in the depletion of the lower channel and the corresponding reduction of the Fermi level in the lower channel. Thus a higher bias voltage is required to match the resonance condition. This means that the apparent shift of the second peak, observed e.g. in the $G(V_b)$ curves of Figure 34, actually is due to the shift of the resonance condition in the gated region. For small central gate voltages therefore the first resonance in the gated section of the device overlaps with the second resonance of the ungated section giving the impression that it is the second resonance which shifts. At higher V_{CG} , however, clearly the second resonance of the ungated region is still present at its original position. It is visible as a shoulder following the first resonant peak^{*)}. Additional evidence that the first peak comes from the ungated section of the device is provided by measurements in a magnetic field applied parallel to the growth direction (i.e. parallel to the tunneling current). Figure 36 compares the differential conductance for g228/6 D3 at $B = 5$ T both for $V_{CG} = 0$ V and $V_{CG} = -0.8$ V.

For $V_b \leq -0.1$ V the only differences between the two curves are the slightly different relative amplitudes of the peaks assigned to tunneling into the second subband and a slight overall shift of the resonant structure to higher V_b . The former can be attributed to the obvious changes in the absolute value of the background current, the latter to the additional series resistance at non-zero V_{CG} . The conformity of the Landau level spectra of the first peaks in the two cases is maintained over the entire magnetic field range. Consequently the first peak in the dI/dV_b traces of Figure 36 can be unambiguously assigned to tunneling in the ungated regions of the device. The gradual depletion of the lower channel with increasing V_{CG} is also reflected by the fact that the broad peak at forward bias is partially suppressed (see Figure 34 and Figure 36).

We now turn our attention to the sequence of small peaks following the “ungated” peak in the dI/dV_b traces of Figure 36, which develop as the central gate voltage is increased above -0.5 V. At these values of V_{CG} there is obviously a transition in the dimensionality of the emitter and collector states and the observed fine structured is therefore attributed to 1D-1D tunneling. From the geometry of the device it is expected that the confinement is weaker in the upper InGaAs channel than it is in the lower channel. This is also obvious from the dI/dV_b traces of Figure 36, for if the subband spacing were of the same order of magnitude in both channels, one would have only a small peak splitting. This is in contrast to the observed broad tunneling structure.

To analyze the behavior of the peak positions with increasingly negative central gate voltage, some care has to be taken about the scaling of the voltage axis. As already noted,

^{*)} Note that the correct amplitude relations between the various peaks cannot be extracted from a superficial inspection of the $G(V_b)$ or $I_{peak}(V_b)$ curves in Figures 35 and 36 due to the contribution of the background current, which is not precisely known.

the central gate induces additional series resistances and also is a source of charge build-up at the transition zone between gated and ungated regions.

Figure 37 shows the subband spacing in the lower channel as a function of central gate voltage. The plotted solid symbols are determined from the spacing of the first and second peak of the 1D-1D tunneling regime. The subband spacing is found to grow approximately quadratically with V_{CG} . The solid line in the figure is the result of a fit using a second order polynomial, found to reproduce best the measured data points. As expected, the values apparently saturate at high V_{CG} , when the device is in the strong pinch-off regime. This again reflects the fact that in this regime the bias voltage axis can no longer be properly scaled. A second point to be noted here is that with the observed subband energies, found to grow from 2.5 meV up to 7 meV, there obviously has to be some entanglement of tunneling peaks belonging to

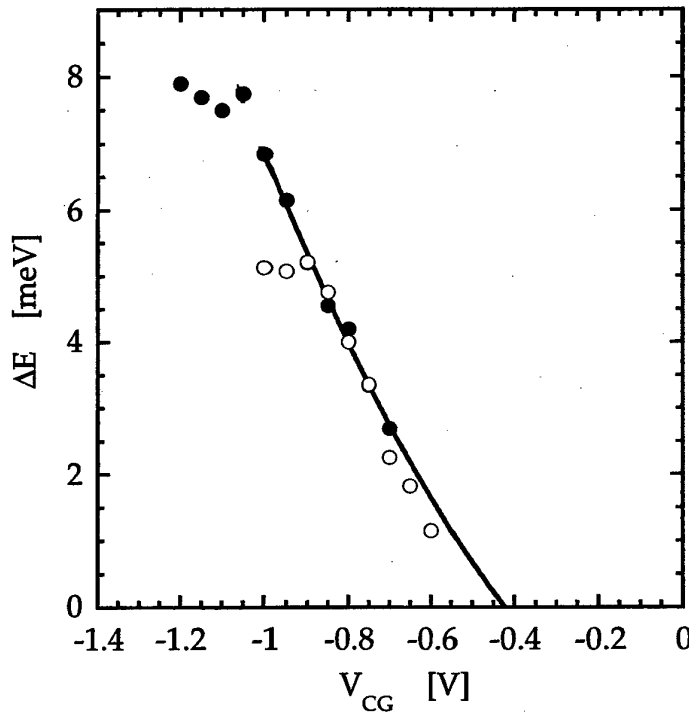


Figure 37: Subband energies of the lower channel of device g228/6 D3, estimated from the scaled peak positions of Figure 36. Solid symbols are results obtained from the first and second 1D-1D tunneling peak (uppermost points and lines of Figure 35, open symbols are extracted from the fourth and fifth peak (lowest curves of Figure 36. The solid line is the best quadratic fit to the data points, indicating an onset of 1D quantization at $V_{CG} \approx -0.4$ V.

contributions of the first and second 2D subband of the lower channel. Evidence for this is given by the double peak structure marked by an arrow in Figure 36. The higher subband energies (open symbols) seem to saturate at somewhat smaller central gate voltages. This might be an indication that the scaling of the bias voltage axis is actually not linear over the entire V_b range.

These results show that with the present device it is possible to achieve quite large subband energies (in the lower channel), ranging between zero and 6 – 7 meV. Although the highest values for the subband energy have to be interpreted with some caution due to the described difficulties with the scaling at high central gate voltages, it nevertheless can be said that it is possible to obtain a level spacing of at least 4 – 5 meV in the lower channel. This value is considerably higher than that usually achieved in side gated wires fabricated from single heterojunctions [59], which are in the range of about 1.5 – 2 meV. The reason is that the lower channel can safely be operated in a regime where it is almost completely depleted, since it is provided with charge carriers tunneling out of the upper emitter channel. The order of magnitude of the measured subband energies is also confirmed by temperature dependent measurements on a similar sample g228/6 DC. When this sample is operated in a similar regime of the central gate voltage, one also observes tunneling into 1D levels. As the temperature is increased, thermal broadening wipes out the small resonant structure, which consequently is found to collapse into two broad peaks corresponding to the original first and second 2D subband in the lower channel. As shown in Figure 38, this occurs at a temperature of about 50 K. The thermal energy at this temperature, $k_B T \approx 4.3$ meV, is therefore of the same order of magnitude as the 1D energy splitting in the lower channel.

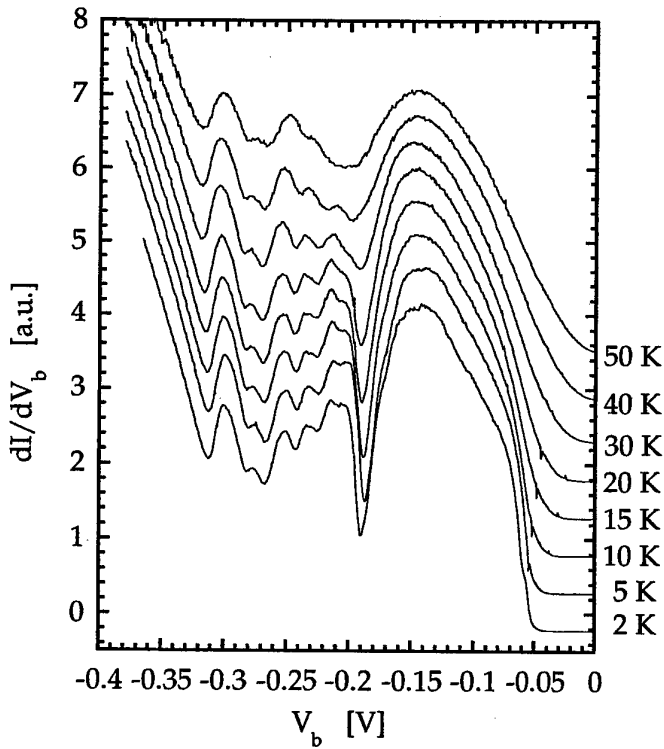


Figure 38: dI/dV_b plotted for several temperatures for sample g228/6 DC. The mesa line of this device is somewhat broader than for g228/6 D3 ($1.2 \mu\text{m}$). Therefore a higher central gate voltage is necessary to achieve appreciable confinement of the lower channel. The various gate voltages are in this case $V_{TG} = -1.32\text{V}$, $V_{BG} = -3.1\text{V}$, $V_{CG} = -2.6\text{V}$.

Also measurements in magnetic fields directed parallel and perpendicular to the tunneling current were carried out with this device structure [44]. They were found to confirm the 1D-1D nature of the tunneling processes as well as the order of magnitude of the measured subband spacing. Measurements in a magnetic field parallel to the wire axis (perpendicular to the tunneling current) could in principle be used to gain information on details of the 1D wave functions of the emitter states [48, 52]. In our case the large linewidth of the tunneling resonances only allows to observe the gross structure of the corresponding tunneling characteristics without giving the possibility to resolve wave function-related fine structure. However, the behavior of the gross structure is in good agreement with the theoretical predictions put forward for 1D-1D tunneling processes [60].

Summary

The investigations presented in this chapter demonstrate that the side gate technique could be successfully implemented as a novel selective depletion scheme for vertical tunneling devices. If no additional confinement was imposed to the active tunneling region of the device (i.e. if $V_{CG} = 0$ V), the differential tunneling conductance revealed pronounced structure due to resonant tunneling from the lowest occupied subband of the InGaAs well into the subbands of the lower GaAs-AlGaAs heterojunction. The measured peak positions were found to reproduce well the calculated subband positions in the junction. The application of a central gate voltage leads to a wealth of additional structure in the dI/dV_b characteristics. This was interpreted in terms of resonant tunneling between 1D states developing in the lateral confinement generated by the central gate. The 1D nature of the corresponding resonant structure in the dI/dV_b is corroborated by measurements of the tunneling characteristics in parallel and perpendicular magnetic fields. By variation of the central gate voltage the lateral confinement was shown to be electrostatically tunable. From model considerations assuming a parabolic confinement the tuning range of the subband energy was estimated to lie between 0 meV and 5 – 6 meV in the lower channel. The confinement in the upper InGaAs channel was found to be in all cases considerably smaller. This has been attributed to the screening action of the δ -doped barrier as well as to the higher electron density in the upper well.

We note that this device principle is not necessarily restricted to narrow-mesa geometries. To ensure the proper action of the bottom gate, a large area device simply has to be provided with a $1\mu\text{m}$ constriction which otherwise does not affect the active tunneling region. To eliminate the influence of the resulting contact resistance, the same fabrication principle can be readily used to implement a four-terminal device geometry. And finally, also the presence of a doped barrier is not necessary for the side gate technique to be applicable. It is sufficient to have a significantly lower carrier density in the lower of the two electron channels. This makes a wide variety of possible tunneling geometries accessible to the experimental study without requiring sophisticated lithographic techniques or advanced sample growing equipment.

One of the most promising applications of quantum wire structures is their use as photoconductive detectors for the far-infrared spectral range. This was also the main motivation for the foregoing investigation of the tunability properties of side-gated narrow channels. Since the 1D subband spacing of etched and gated structures typically is in the range between 1 meV and 10 meV, the exploitation of their photodetecting capabilities would open a spectral window for the detection of radiation in the Terahertz range. This spectral region is not yet developed very well and sources (especially coherent sources) as well as detectors are scarce. As photoconductive detectors, quantum wires have several advantages over e.g. parabolic quantum wells. On the one hand one could fabricate large arrays of gated wire structures on very small areas, where each single wire could be operated independently. This would make a considerable range of far-infrared frequencies detectable on a single microchip. Another advantage of gated wires comes from the fact that the 1D subband spacing can be tuned over a considerable range of energies as subband energies have been found to vary between zero and 6 meV. Generally, this wide tuning range is not found in quantum channels fabricated from single heterostructures, which tend to deplete at already moderate gate voltages with negative effects on their photoconductivity. Barrier separated double channel systems have been found to be in some sense immune against premature depletion in so far as the conductivity of some lower, nearly depleted channel is maintained due to electrons tunneling from the top channel into the almost empty states of the lower one. A promising way of further study would therefore be provided by the investigation of the photoconductive properties of side gated devices. Very probably, however, the fabrication methods will have to be refined considerably since particularly etching processes introduce a sidewall roughness, which has disadvantageous effects on the expected linewidths of photocurrent resonances.

Part B

Novel THz Emission Devices

E. Gornik, C. Pacher, C. Rauch, G. Strasser, J. Ulrich, K. Unterrainer, and R. Zobl

The THz regime is defined between 100 GHz (3 mm) and 10 THz (30 μm). Since no compact THz sources are available, an increasing need is present to develop devices in this frequency range for technical applications. The THz frequency range is characterized by numerous amount of important resonances in spectroscopy. This reaches from molecular spectroscopy over astrophysics to fundamental resonances in solid state material and semiconductor devices. Further applications include radar sensing systems, the high frequency characterization of new materials and microelectronic devices, environmental monitoring and tomography.

However the technological coverage of this range is poor. The low frequency limit is given by the availability of microwave sources. The high frequency border of the THz regime is given by the low frequency limit of photonic devices.

In this project we concentrate on the development of coherent THz radiation sources based on semiconductor devices by investigating various possible mechanism, which might lead to coherent and compact sources. For this purpose we consider concepts in which the electron distribution and corresponding the emission spectrum can influenced by bandstructure engineering especially by growth and nanofabricated structures.

A novel concept considers the occurrence of a current driven plasma instability (CDPI) in electron systems when the drift velocity exceeds the Fermi velocity. In this situation the instability can grow and be used to generate THz radiation via a grating coupler. However the necessary drift velocities are unrealistically high. In modulated systems and especially in modulated high mobility quantum wire systems the CDPI effect is expected to occur already at rather low drift velocities and provide an efficient source of radiation. This lead to the study of quantum wire properties. A different approach is to generate a confined plasmon. In this case tunnel injection can be used to achieve an inverted electron distribution by injecting carriers selectively into higher quantum well states and maintain an efficient extraction scheme. In this case the occurrence of a CDPI is also possible.

Electrons drifting in a periodic potential can emit coherent THz radiation, if a bunching of electrons is achieved. This bunching requires an electron mean free path, which is larger than the period of the potential modulation. As first experiments successfully showed the occurrence of a grating induced radiation (Smith Purcel Effect), this concept seems to be a promising way to construct efficient radiation sources. These ideas motivated the study on superlattice transport.

2. EMISSION STUDIES

In this section concepts for the realization of an electromagnetic emitter that emits light in the THz regime are introduced. Different generation schemes for THz radiation are investigated in detail.

The first is based on the generation of plasmon oscillations by current injection in nanostructures. We start with the study of incoherent plasmon excitations in parabolic quantum wells, to study the efficiency of radiative plasmon decay. The next step is the realization of appropriate injection and extraction schemes to maintain a sufficient population inversion in the carrier distribution to generate a plasma instability. This will lead to stimulated plasmon decay and coherent THz emission.

The second scheme is based on electrons oscillation in a superlattice potential leading to so-called Bloch oscillations.. These electrons can emit coherent THz radiation, if the electron mean free path is large enough so that Bloch oscillation can occur before they are damped by scattering.

2.1. Multiple Superlattice Structures

While the previous section describes the transport through a single period superlattice structure, this section refers to transport through a combination of two or three superlattices with different well widths and barrier thicknesses. The basic motivation of these experiments is the realization of a long wavelength infrared laser based on inter miniband emission [61] in the conduction band of a superlattice. Strongly coupled superlattices are favorable to intersubband transitions in quantum wells by means of higher oscillator strength of the transitions [62]. In addition special structures have to be designed to maintain a population inversion within the miniband structures.

To test the transition probability and amount of inversion of blocked miniband superlattice structures, samples with combinations of several five period superlattices were carefully designed and simulated using a standard Schrödinger solver software [63] for calculating appropriate band structures. In Figure 39 the basic idea is shown: electrons injected into the miniband on the left side can only pass the entire structure by a recombination process with the middle miniband. The direct nondissipative way is blocked. Two different multiple superlattice structures are embedded into the three terminal device. Sample g194 consists of two superlattices (SL) with five periods each. The structure is designed in a way that the first miniband of SL1 is aligned with the second miniband of SL2. Injected electrons with energies high enough to traverse into the miniband of the first superlattice have two output channels: via the second miniband of SL2 without scattering or via the first miniband of SL2 after a decay process. The growth parameters are given in Table 3: Description of the multiple superlattice layers.

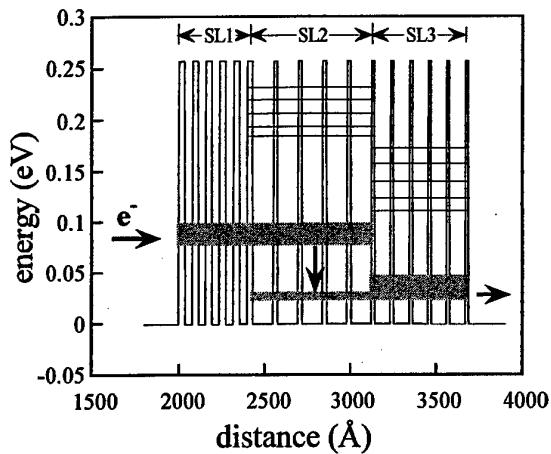


Figure 39: Conduction band diagram of a multiple superlattice structure. The second miniband of superlattice 2 is aligned to the first miniband of superlattice 1 and to the energy gap of superlattice 3 (blocked miniband). A transition of injected electrons to the lowest miniband of superlattice 2 is necessary to observe transport through the whole structure.

sample No.	superlattice 1 (5 periods)		superlattice 2 (5 periods)		superlattice 3 (5 periods)	
	barrier (nm)	well (nm)	barrier (nm)	well (nm)	barrier (nm)	well (nm)
G194	3.5	4.25	2.5	12	-	-
G202	3.5	4.25	2.5	12	1.5	8.5

Table 3: Description of the multiple superlattice layers.

Sample g202 consists of three superlattices. Again the second miniband of SL2 is aligned with the first miniband of SL1 like in analogy of sample g194. SL3 is designed in such a way that the first miniband is aligned with the first miniband of SL2, but the second miniband of SL2 is blocked by the minigap of SL3. Consequently, only electrons that have performed an interminiband transition between the second and the first miniband in SL2 can pass the entire structure. Electrons that are reflected by the minigap and not scattered into the first miniband bounce back to the base contact. These electrons will not be transmitted and do not contribute to the measured collector current.

In Figure 47 the transfer ratios α versus injection energy are shown for all samples. A sharp increase of the transfer ratio at about 97 meV corresponds to the calculated position of the lowest miniband in SL1. The additional peaks (separated by 36 meV) in the transfer ratio spectra can be again identified as the longitudinal optical phonon replica as described in the previous section.

The transfer ratio of sample g202 (three SL structure) is observed to be about 50 % of the transfer ratio of sample g194 (two SL structure). Thus indicating that about half of the

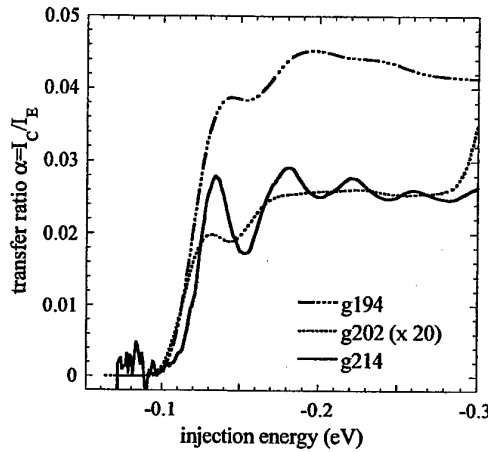


Figure 40: Measured transfer ratio of three different samples. While sample g194 consists of two superlattices, the second miniband of sample g202 and g214 is blocked by a third superlattice as indicated in the band structure above.

electrons pass the 70 nm long region of the second miniband of SL2 without scattering indicating a transit time comparable to the scattering time.

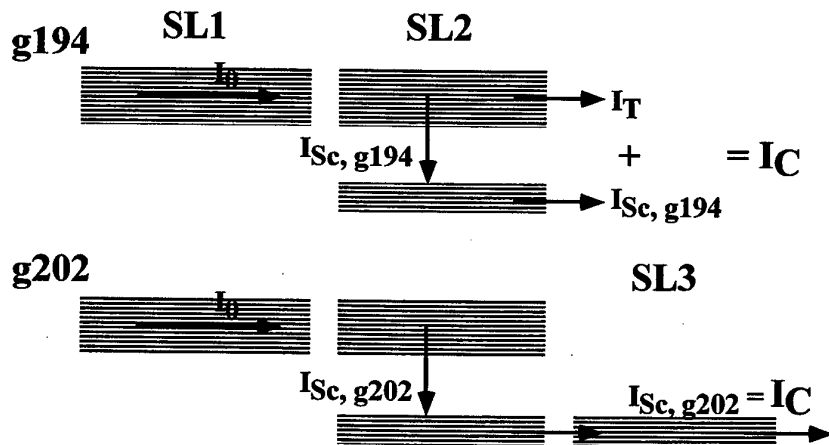


Figure 41: Systematic sketch of the different transport channels through the structure for ballistically injected hot electrons.

The different transport channels of the two samples are shown schematically in Figure 41. If we neglect any reflection of electrons injected into the second miniband of SL2 in sample g194, the measured collector current is equal to the injected current ($I_{C,g194} = I_0$). In sample g202, only those electrons which have undergone subband transitions will be measured at the collector. The collector current for this case is given by

$$I_{C,g202} = I_0 \left(1 - e^{-\frac{2l_{SL}}{\lambda_{sc}}} \right)$$

where l_{SL} is the length of SL2, and λ_{sc} is the electron scattering length. From the experiment we know that $I_{C,g194}=2 I_{C,g202}$. Substituting the collector currents of the two samples gives

$$I_0 = 2I_0 \left(1 - e^{-\frac{2l_{SL}}{\lambda_{sc}}} \right)$$

solving this equation gives the scattering length and the scattering time of the injected electrons to be

$$\lambda_{sc} = -\frac{2l_{SL}}{\ln \frac{1}{2}} = 200 \text{ nm}$$

$$\tau_{sc} = 250 \text{ fs}$$

This result proves that the inter miniband transitions are mainly governed by LO- phonon emission as the energy gap between the second and the lowest miniband is of the order of the longitudinal optical phonon energy $\hbar\omega_{LO}$. The transit time through the miniband is then of the same order of magnitude.

2.1.1. Higher current Three Terminal Devices

This section introduces a modified three terminal device structure. The basic idea behind this concept is to inject selectively carriers into the second miniband of a high period superlattice in order to achieve population inversion. The overall goal of this concept is to achieve lasing action by interminiband tunneling. The wavelength of such devices is thus determined by the minigap and can be designed in a way that the transition energy is less than the LO-phonon energy. In fact, this concept even might be used to generate THz radiation.

In contrast to spectroscopic investigations, where the number of electrons injected into the quantum structure is very low to avoid the influence of electron-electron interaction in the superlattice, a high number of carriers is needed for emission devices. To maximize the current through the miniband structure the base contact is grown into the first well of a 50 period superlattice as shown in Figure 42. The superlattice consists of 28 nm GaAs wells and 2.5 nm $\text{Al}_{0.3}\text{Ga}_{0.7}\text{As}$ barriers. For these parameters a simple Kronig-Penny calculation gives the lowest miniband lying between 5 and 7 meV, the second between 20 and 25 meV, a third between 45 and 55 meV, and a fourth between 82 and 97 meV. It should be noted that the injector barrier also serves as the first superlattice barrier. The base and collector contact layers are grounded in order to establish flat band condition for the superlattice. Since there is no drift region between the injector and the structure

longitudinal optical phonon replica will not be observed. As a consequence the injected current is expected to be much higher.

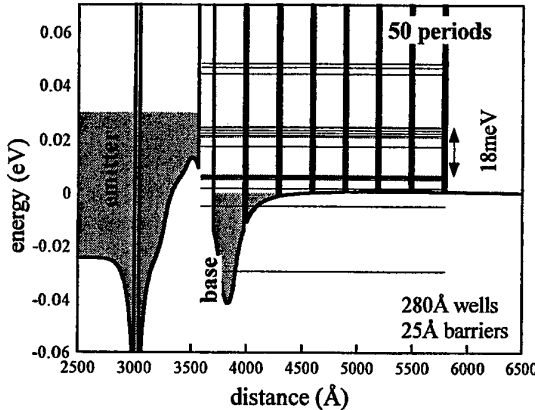


Figure 42: Calculated band diagram of a high power three terminal device including band bending. The base is grown into the first well of a 50 period superlattice consisting of 28 nm GaAs wells and 2.5 nm AlGaAs barriers.

The transition energy of the grown structures is calculated to be 18 meV, well below the LO-phonon energy. Figure 43 shows the measured collector current versus injection energy. The calculated positions of the minibands are indicated by hatched bars. Since no phonon replica are present, the peaks due to miniband transport can be identified directly in the measured collector current. At very low emitter biases a sharp increase of the collector current due to transport of injected electrons through the first miniband is measured. A saturation of miniband transport up to the third subband is observed. The peak at about 50 meV due to transport through the third subband is clearly evident.

In order to measure the current voltage characteristics of semiconductor heterostructure with low resistance, mesa with diameters in the submicron range have to be fabricated in order to ensure homogenous transport through the entire structure. Since the processing of mesa structures requires less photolithographic steps, these devices are used for all basic characterization measurements of the heterostructure.

To measure emission of the considered structures the mesas have to be coupled via airbridges to broad band antennas in order to increase the radiation efficiency perpendicular to the wafer and to decrease any parasitic capacities.

The measured transmitted current injected into the second miniband ($\sim 6 \text{ mA/cm}^2$) is about 100 times higher than the currents measured in conventional three terminal devices, but still considerably too low to get emission out of these structures. Considering a quantum efficiency of 10^{-6} the optical output power of a device with an active area of 0.25 cm^2 can be estimated to be in the range of 0.4 pW thus too low to be detected.

This clearly shows that this is a possible approach to increase the current in injection devices. The best way to increase the current turned out to be realized with quantum cascade structures which are combined with graded superlattice structures as will be discussed in chapter 2.3.

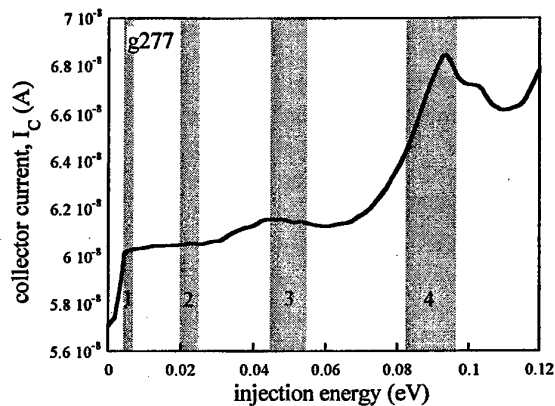


Figure 43: Measured collector current versus injection energy of a high power three terminal device. Since no drift region is grown between injector barrier and superlattice, no phonon replica can be observed. The nominal positions of the minibands are indicated by shaded areas in the figure.

2.2. Emission measurement technique

The emission experiments are performed with a specially designed set up, consisting of a light pipe immersed in liquid Helium, holding emitter and detector under 4K background conditions. This guarantees the most sensitive detection of weak emission signals. Spectroscopy is performed by tuning the InSb cyclotron resonance detector with the magnetic field.

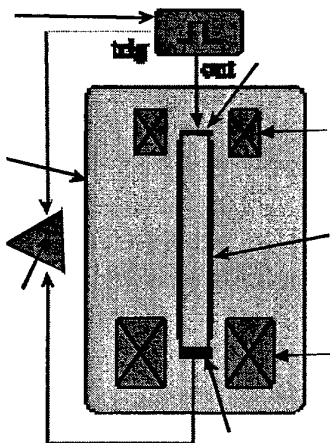


Figure 44: Emission set up showing emitter and detector inserted in liquid Helium. The detector is tuned by the magnetic field. The basic measurement equipment is also shown schematically.

A plot of the detailed spectral response for the InSb detector is shown in Figure 45 as obtained with a narrowband GaAs cyclotron emitter [64]. The emitter has a spectral width of 2cm^{-1} corresponding to a width of $\Delta E=0,25\text{meV}$. The emitter is set to different frequencies by the upper magnetic field as shown in Figure 44. The detector is continuously tuned and thus represents a spectrometer with a given resolution.

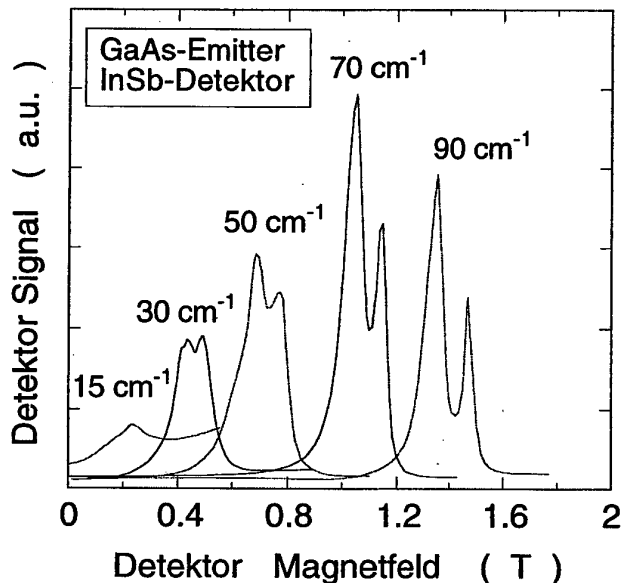


Figure 45: InSb detector signal as a function of magnetic field for different emitter frequencies. The width of the emission line is $0,25\text{meV}$.

The peak response correspond to the upper line, since the spectral response of the impurity line is dominant at 4K. This plot (upper curve) represents the spectral analysis characteristic of the InSb detector and is used throughout this report as conversion of magnetic field into frequency or energy.

The spectral resolution of the InSb detector is in the order of 10cm^{-1} corresponding to an energy resolution between 1,3 and 1,5 meV depending on the magnetic field of operation. The main reason for the rather low resolution comes from the existence of two detector lines separated by about 8 cm^{-1} . The magnetic field dependence of the two detector lines is shown in Figure 46.

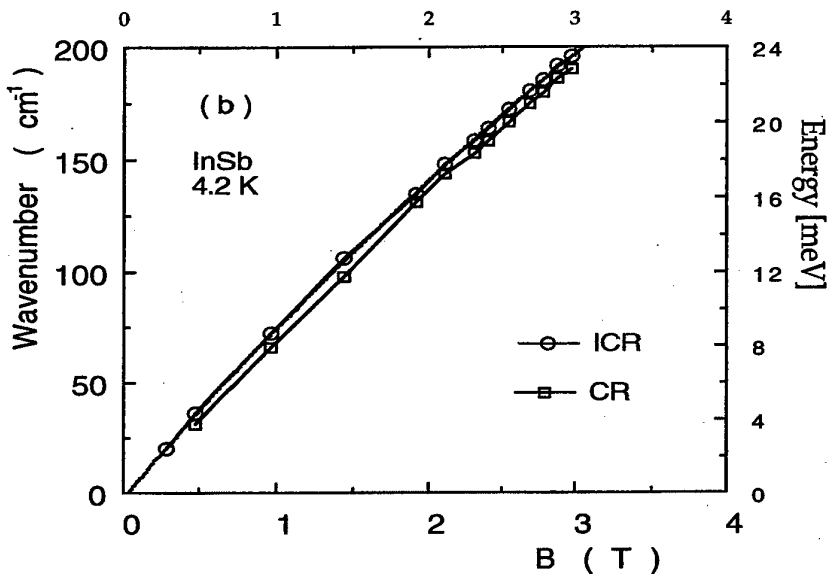


Figure 46: InSb detector line positions as a function of magnetic field. The squares correspond to the cyclotron resonance the circles to the impurity resonance transition. This plot is used for the conversion between energy and magnetic field.

2.3. Generation of plasmon emission from parabolic quantum wells

Parabolically graded quantum wells are promising candidates for far-infrared sources operating above liquid nitrogen temperature, because their emission frequency is independent of the electron distribution and concentration in the well. Therefore, the large temperature-induced variation of the electron distribution is expected to have little impact on the emission performance. In absorption and emission spectroscopy [65,66] coupling between the radiation and the electron system has been observed at only one frequency. This is the harmonic oscillator frequency, solely determined by the width and the energetic depth of the quantum well.

Two samples were examined: one with 140 nm, the other one with 200 nm well width, both with 167 meV energetic well depth. The samples were grown by molecular beam epitaxy, depositing alternate layers of $\text{Al}_{0.3}\text{Ga}_{0.7}\text{As}$ and GaAs on a semi-insulating GaAs substrate. Thereby, the digital alloy technique [67] was applied. By adjusting the ratio of the layer thicknesses, the average Al-content in the well region is parabolically graded from $x = 0$ to $x = 0.2$. The well is sandwiched between $\text{Al}_{0.3}\text{Ga}_{0.7}\text{As}$ spacer layers and remotely doped.

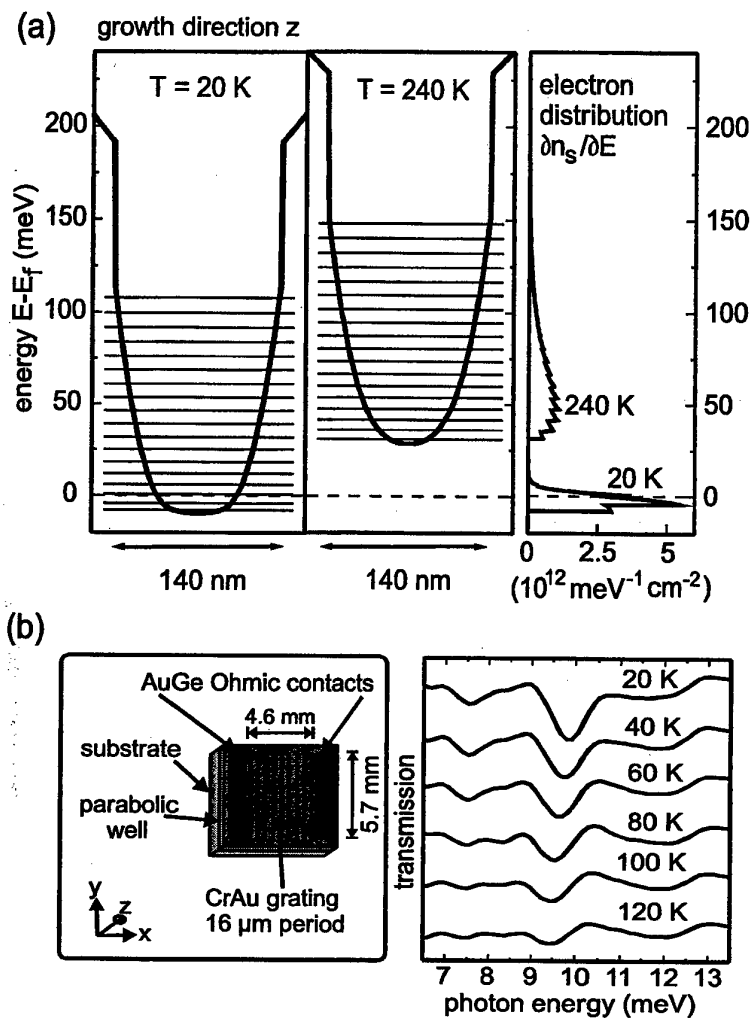


Figure 47: (a) Self-consistent calculation of the band diagram of the 140 nm well at two different temperatures T as indicated. The horizontal lines denote the energy levels in the graded part of the well. The electron sheet concentrations n_s from Hall measurements have been used as input parameters. The right panel shows the electron distributions for the two temperatures. (b) Device geometry of the 140 nm well sample and transmission spectra at various temperatures.

By Hall measurements we determined the electron concentration and mobility. Here we describe only the results from the 140 nm well sample which is more representative for the results. In the 140 nm well, the electron concentration varies from $3.8 \times 10^{11} \text{ cm}^{-2}$ at 20 K to $5.1 \times 10^{11} \text{ cm}^{-2}$ at 240 K, the mobility decreases from $7.2 \times 10^4 \text{ cm}^2/\text{Vs}$ at 20 K down to $0.7 \times 10^4 \text{ cm}^2/\text{Vs}$ at 240 K. The schematic energy band diagram of the 140 nm well is shown in. The left panel of shows the device geometry schematically. The 140 nm well sample was contacted with two 5.7 mm long AuGe Ohmic contact stripes, 4.6 mm apart. In order to couple out the intersubband radiation that is polarized with its electrical field perpendicular to the layers a metallic CrAu grating of 16 μm period was evaporated between the contacts.

We measured the electroluminescence of the parabolic quantum wells using a Fourier-transform infrared spectrometer in step scan mode with a spectral resolution of 0.5 meV. The sample was mounted on the cold finger of a helium-flow cryostat. The emitted radiation was collected by an off-axis parabolic mirror with an f/2 aperture, transmitted through the spectrometer, and then focussed by another parabolic mirror on a helium cooled Si-bolometer. The whole beam path was purged with dry nitrogen gas to minimize the far-infrared absorption of water vapor. In order to excite the electron gas a pulsed electric field at a frequency of 411 Hz and 50 % duty cycle was applied between the Ohmic contacts. A lock-in amplifier was employed to detect the bolometer signal.

In Figure 48 spectra of the 140 nm well at various temperatures are displayed. The peak emission is observed at a photon energy of 9.8 meV at low temperatures, that is slightly shifted to 9.1 meV, as the temperature is raised to 240 K. This value corresponds to the harmonic oscillator energy calculated from the well dimensions is 8.4 meV. The full width at half maximum of the emission line ranges from 1 meV at low temperatures to 2 meV in the high temperature regime ($T > 100$ K). The line position and its temperature related shift, as well as the line width agree with the behavior observed in the transmission experiments. For comparison, we estimated the line width corresponding to the Drude's electron scattering time obtained from the mobility data. In the whole temperature range, the measured emission linewidths are larger than the estimated ones ranging from 0.2 meV at 20 K to 2 meV at 240 K. This is an indication that some inhomogeneous broadening is present.

The optical power collected by the bolometer P_{co} of both samples is depicted in Figure 49 as a function of inverse temperature. It was determined as the integrated area of the emission spectra divided by an amplification factor and the bolometer sensitivity. Using a collection efficiency of the optical set-up of $\sim 10^{-3}$, we estimate the optical power per area P_o/A , emitted in a half sphere at a temperature of 20 K. For the 140 nm well sample, we find $P_o/A = 11 \text{ nW/cm}^2$ at an electrical input power density P_{el}/A of 250 mW/cm^2 . This is a quite conservative estimate of the emission intensity, which could well be a factor of 5 higher assuming a collection efficiency of 5×10^{-3} . This results in an efficiency P_o/P_{el} of 4.4×10^{-8} or 2.2×10^{-7} with the more optimistic assumption. The collected optical power P_{co} is assumed to depend on the electrical input power P_{el} and on the ratio of non-radiative life time τ_{nr} and radiative life time τ_r of the intersubband plasmon (in case of

$$\tau_r \gg \tau_{nr}$$
 like $P_{co} \propto P_{el} \frac{\tau_{nr}}{\tau_r}$.

The proportionality between the collected optical power P_{co} and the electrical input power P_{el} has been confirmed up to ~ 70 mW, above which saturation occurs. Lacking a model for the decay of intersubband plasmons, we follow the approach of Maranowski et al. [68] and Heyman et al. [69] and discuss the relaxation times in a single electron picture. The difference in the efficiency P_o/P_{el} between the two samples can be qualitatively understood by looking at the radiative life time τ_r . It was calculated in the model of a classical electron oscillator as 59 μs for the 140 nm well.

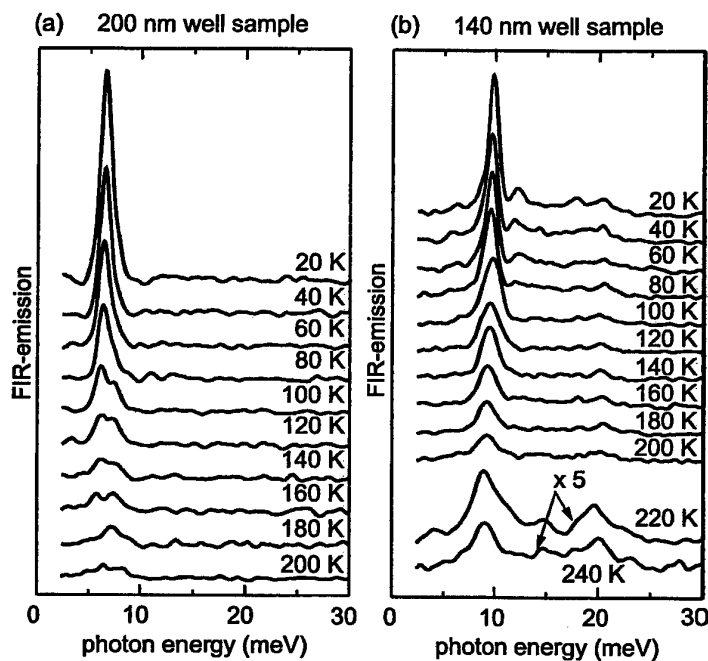


Figure 48. Emission spectra of the 140 nm well sample for various temperatures as indicated. The spectra of the two highest temperatures are shown enlarged by a factor of five.

The decrease of (collected) optical power is induced by a thermally activated process. The solid lines in Fig. 3 are fits of the inverse sum of two exponential functions in $1/T$ yielding in activation energies of $E_1 = 34$ meV, $E_2 = 0.8$ meV for the 140 nm well sample. The higher energy E_1 is probably the activation barrier for the emission of optical

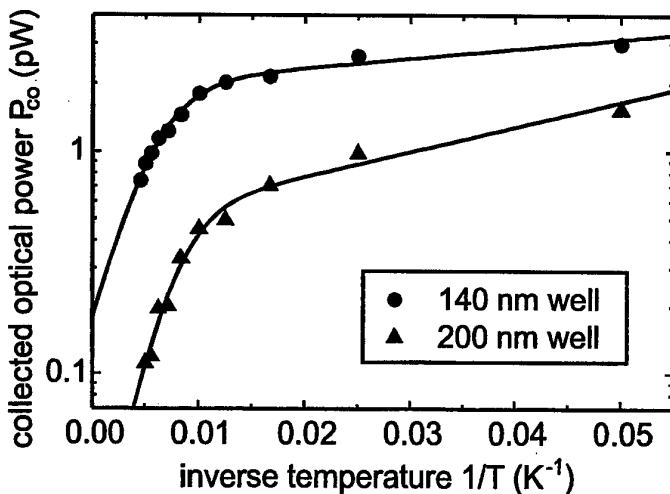


Figure 49. Collected optical power P_{co} versus inverse temperature $1/T$ of the 140 nm well sample driven at 65 mW (solid circles). The solid lines are inverse double exponential fits.

phonons $\hbar\Omega_{LO} - \Delta E$, where the energy spacing ΔE between the two lowest subbands is 4 meV in the 140 nm well (see (a)). The low energy E_2 activation process is most likely connected with the thermal dependence of the contact resistance. The intersubband relaxation rate $1/\tau_{nr}$ shows a similar behavior of thermal activation, as described by Heyman et al. [69]. We conclude that the temperature dependence of the optical power is governed by the non-radiative life time τ_{nr} . For simplicity, we disregard any changes in the excitation process. At temperatures above ~ 100 K, the emission of optical phonons limits the optical power. Assuming the non-radiative rate in the high temperature limit ($k_B T \gg \hbar\Omega_{LO}$) to be $1/\tau_{nr} = 2 \text{ ps}^{-1}$, the phonon relaxation time at the temperature of 100 K is determined as 26 ps for the 140 nm well sample, which has to be related to the radiative time of 59 μs . Using these values we obtain an internal quantum efficiency of 5×10^{-7} . At low temperatures where the external efficiency has been determined the internal efficiency is expected to be even a factor of five larger.

These results demonstrate electrically driven far-infrared emission from parabolic quantum wells up to a temperature of 240 K. At even higher temperatures, the thermal energy $k_B T$ exceeds the photon energy by a factor greater than two. The electron distribution in thermal equilibrium varies significantly in the investigated temperature range, still single frequency emission, and a rather constant emission line shape is observed. The emission efficiency is limited by the temperature dependent decrease of the non-radiative life time.

These results clearly show that radiative plasmon decay is a robust mechanism, which extends to higher temperatures than any other THz emission process. There are several ways to extent the emission to room temperature: one the one hand the injection and plasmon excitation process efficiency can be improved, on the other hand the nonradiative decay can be influenced by reducing the decay via optical phonons by bandstructure engineering.

2.4. Generation of Coherent Plasmons for radiative decay

A plasmon instability is a robust classical phenomenon of microcharge oscillations, the analog of which is well known in gaseous plasmas. In fact, the frequency of carrier plasma oscillations of typically doped semiconductor systems is in the THz range as shown in *Figure 50*. It is seen that radiative plasmon decay can lead to emission frequencies which allow to cover the whole THz range with well available carrier densities between 10^{16} cm^{-3} and 10^{18} cm^{-3} . This principle would therefore allow to cover an extremely large frequency range. Two of the major advantages of this concept are the possibility to operate these emitters up to high temperatures (even at room temperatures are possible) and that there is no RC limitation.

In general, all non-equilibrium plasmas can develop spontaneously plasma oscillations [70]. This happens because plasmons form an efficient energy dissipation channel in a carrier gas. It should therefore be possible to convert the free energy stored in a non-equilibrium plasmas to radiation .

The concept which has turned out to be most promising and was decided to be pursued after several other concepts was proposed by K. Kempa and Bakshi [71]: this concept requires a population inversion of the carrier distribution in combination with the presence of confined plasmons. The basic idea is to use an energetically selective injection and extraction scheme for carriers into a bounded active region where plasmons can be generated, followed by an energetically selective extraction scheme which maintains the inversion.

The structures designed for these experiments consist of two coupled quantum wells, one of which acts as a plasma resonator, i.e. can sustain growing plasma oscillations, and the other which acts as a plasmon emitter, providing a proper arrangement of levels to assure efficient emission of plasmons into the resonator. A resonant tunneling diode filter, attached to the plasmon emitter maintains an efficient carrier extraction from the active region.

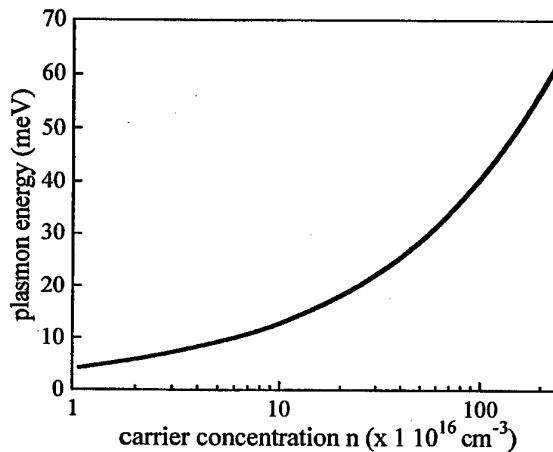


Figure 50: Plasmon energy versus carrier concentration.

A typical band structure under forward bias is shown schematically in *Figure 51*. The basic idea is to realize a three level scheme of finite and controllable size in which the first subband and the third subband of the plasmon emitter quantum well are occupied, while the second subband is kept partially empty. Occupation of the third level is assured by heavy electron inflow from the plasmon resonator area, while the occupation of the first level is due to the very fast intersubband transitions from the third subband by optical phonon emission. The energy separation between the third and first subband is chosen to be equal or larger to the energy of an LO-phonon. Since the LO-phonon scattering time is of the order of 200 fs this process is very effective. The second subband is designed in a way that the level can be aligned under typical bias conditions to the resonant level of the extractor resonant tunneling diode. This extraction, if efficient, assures a lower depopulation due to resonant carrier extraction. We hope that this mechanism can maintain a lower population in this level than in the upper level. The insets of Figure 51 show the expected population inversion with the 3 levels schematically and the level structure with the carrier transitions.

2.4.1. Transport characterization

A series of structures were grown using different growth techniques and slightly different layer thicknesses. The sample parameters are summarized in *Table 4*. The MBE grown wafers are structured into submicron mesa structures. The devices are then used to measure the current-voltage characteristics at 4.2 K in order to characterize the structures and to verify their desired properties.

The devices are processed into $7 \times 8 \mu\text{m}^2$ mesa using standard technologies. To characterize the structure and verify the desired properties, the measured I-V curves are compared to the calculated I-V characteristics. In order to perform emission measurements the grown structures are processed into $6 \mu\text{m}$ wide ridges with different lengths between 20 and $50 \mu\text{m}$ as shown in Figure 52. Several mesas are connected in parallel in the emission experiments to obtain the necessary high current levels.

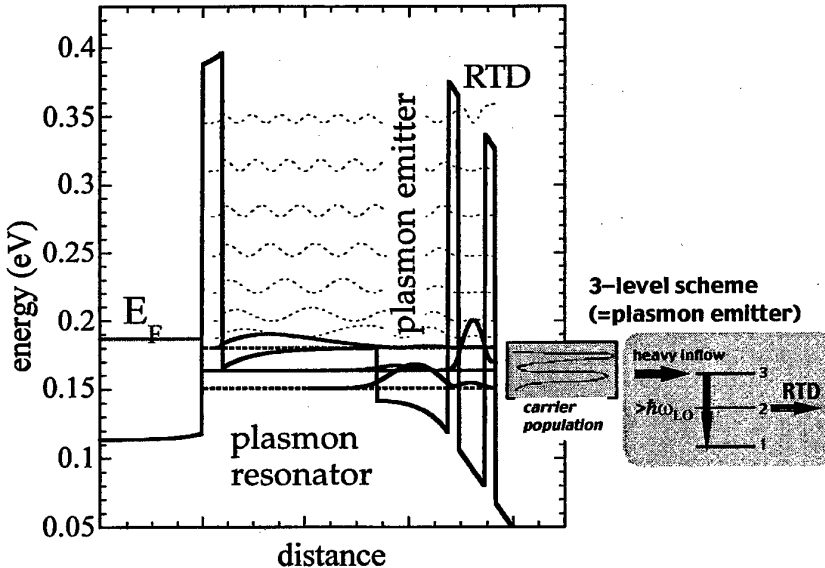


Figure 51: Typical conduction band diagram of a plasmon generation device consisting of a plasmon resonator, a plasmon emitter (3-level scheme), and a resonant tunneling extraction diode. The insets show the expected population inversion with the 3 levels and the level structure with the carrier transitions.

Figure 53 shows the current-voltage characteristics of sample g205 and g206 measured on a $3 \times 3 \mu\text{m}^2$ Mesa. the smallest mesas show the best IV characteristics since they have the lowest series resistances and in-plane nonuniformities. Sample g205 and g206 have the same nominal layer thicknesses and the same doping concentration but are grown slightly different. For sample g205 the $\text{Al}_{0.05}\text{Ga}_{0.095}\text{As}$ barrier is grown employing digital growth, while for sample g206 this barrier is grown at a very low Al cell temperature in order to get a very low Al mole fraction. The IV characteristics for both samples are only similar in terms of the overall behavior however the diode character is only well pronounced in

Layer (Substrate to Surface)	X (%)	G205/G206		G301	
		Thickness (Å)	Doping (Si)	Thickness (Å)	Doping (Si)
Si: GaAs		5000	2 e18	5000	1e18
GaAs		200	-	200	-
AlGaAs	33	20	-	20	-
GaAs		50	-	47	-
AlGaAs	33	20	-	20	-
GaAs		135	1e18	155	0.73e18
AlGaAs	5	300	2.5e17	400	3e17
AlAs	100	40	2.5e17	40	3e17
Si: GaAs		3000	2e18	2000	2 e18

Table 4: Growth parameters of the double quantum structures.

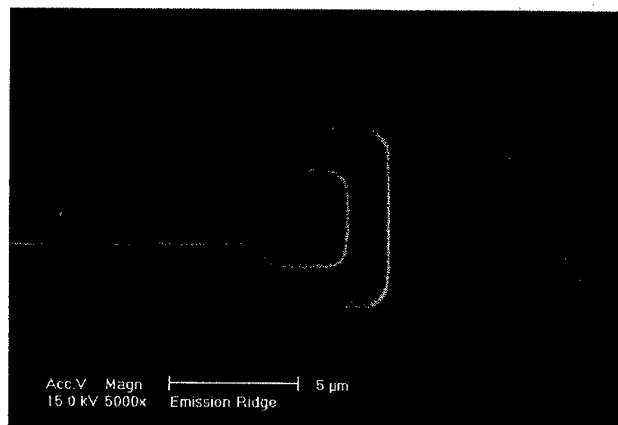


Figure 52: SEM picture of the top contact of a 6 μm wide ridge. Silicon nitride is used to isolate the extended contact from the highly doped bottom contact.

sample g205. In sample g206 the resonant features are only very weak. For sample g205 a series of peaks can be observed in the conductance-voltage curve for negative bias, while a single feature is observed for positive bias at about 0.35 V. The measured current-voltage characteristics scale with mesa size up to a diameter of $10 \times 10 \mu\text{m}^2$ showing that the result is unaffected by in-plane nonuniformities for these sizes. For larger mesa sizes, a nonuniform current transport profile has to be considered since the sample resistance is very low and the current is expected to flow primarily through the edges of the mesa. It is clearly evident that the features in the IV-curves are only clearly pronounced in sample g205 while sample g206 does not show clear structures in the first derivative. This is a clear indication that the digital growth technique seems to be the better growth technique for structures needed in these experiments.

Figure 54 shows the current-voltage and the conductivity-voltage characteristics for sample g301, which is a modified structure g205. The modification involves increasing the size of the plasmon resonator and the plasmon emitter as it is expected that the emission

will become more effective with increasing size of the plasmon resonator. Also this material shows a clear nonlinearity in the current at a positive bias of 0.35 V due to the resonance of the second level with the resonant tunneling diode. The features in the negative bias direction are less pronounced than for sample g205. However sample g301 has a considerably better diode characteristic than g205 and has a similar current density. The better characteristic makes sample material g301 more promising for emission experiments. The current density at the extraction resonance is in the order of 10^3 A cm^{-2} for both samples.

The measured transport properties are compared to the results of two calculations of the dynamic conductivity. First, employing the zero frequency limit of the Random Phase Approximation (RPA) conductivity, and second, the standard tunneling theory based on a calculation of the total transmission coefficient. The result of these calculations

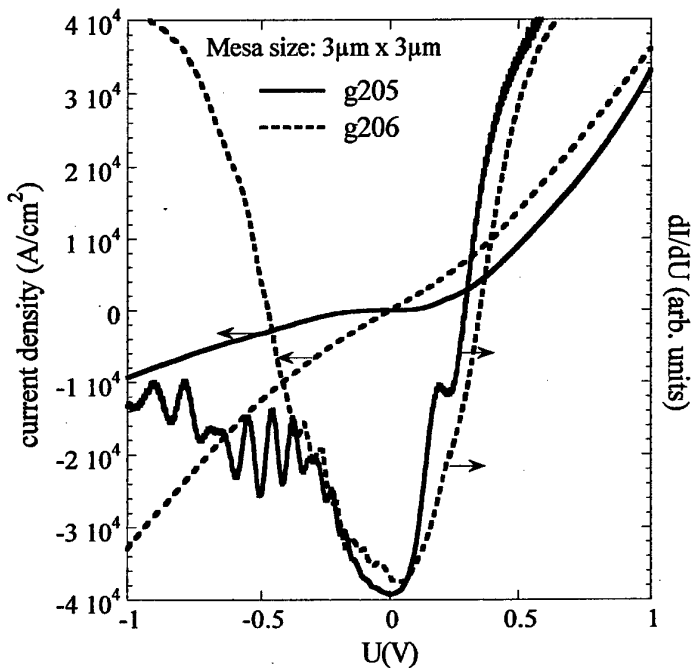


Figure 53: Measured current density and conductance versus voltage for sample g205 (solid lines) and g206 (dashed lines).

are compared to the experimental data. Both structures have similar features. The series of peaks for negative bias represents the resonantly enhanced transport as the resonant tunneling diode (RTD) "walks" through the levels of the active region. These peaks at negative bias are more pronounced in sample g205. For positive bias (forward bias direction) there is one distinct feature around 0.15 V. This feature corresponds to the RTD extraction from the localized subbands of the plasmon emitter. At the voltage of the second feature (corresponds to the carrier extraction out of level 2) at about 0.35 V an instability is expected to occur.

The calculated dI/dU characteristics are in qualitative agreement with the experimental curves [72], except that the calculated features are more pronounced. Part of this resonance broadening is caused by electron scattering processes, which are incompletely treated in the RPA calculation, as well as by smearing of the levels due to tunneling of electrons into the open space of the outer region, neglected in the RPA.

The overall agreement between theory and experiment indicates that the grown structures are of good quality and conform to the design parameters. The desired population scheme can be foreseen.

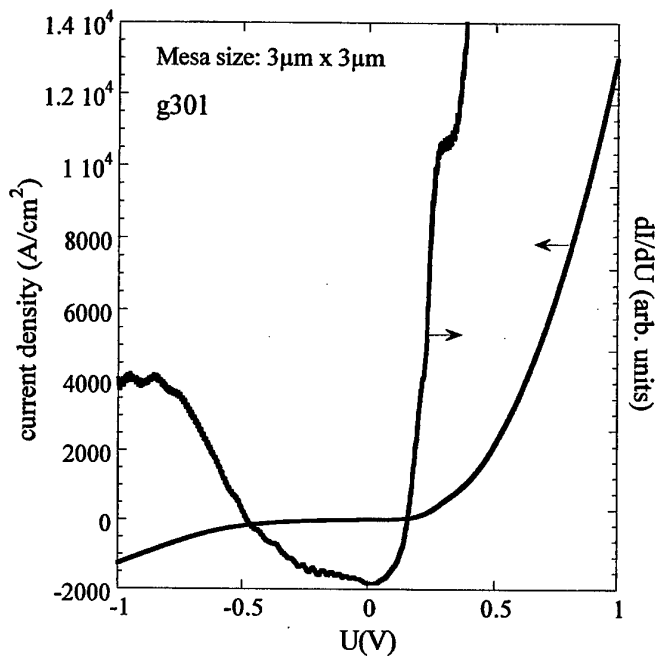


Figure 54: Measured current density and conductance versus voltage for sample g301.

2.4.2. Emission experiments

However the ultimate goal of the design of these structures is to generate electromagnetic radiation in the far infrared spectral range via plasma instabilities. Whether plasma instability will occur in a given heterostructure is determined by collective electromagnetic response of that structure. This response can be calculated by employing

the RPA formalism [73]. The growth rate calculated from the analysis should exceed the damping rate due to electron phonon interaction and other dissipative processes [72].

Unstable modes are found to exist for sample g205 and for sample g301. For sample g205 a robust instability is expected only for the case of practically empty second subband of the plasmon emitter. Sample g301 is designed to sustain instability for larger population values of level two. The resonator length has been extended in order to accommodate more subbands. A robust instability with a gain of about 0.4 meV is predicted.

In order to prove the predicted instability we have performed first emission measurements on structures made out of material g205, g206 and g301. We have observed a weak emission signal with a spectral content in the 10 to 15eV range for the samples g205 and g301, while no emission could be detected from sample g206.

The emission signal from sample g205 for a high positive bias, well above the voltage of the resonant feature is shown in

Figure 56, where the InSb detector response is shown as a function of magnetic field and frequency. A broad resonance superimposed on a rising background signal is clearly evident between one and two T. By subtracting the InSb background signal which is due to broadband radiation from the thermal heating of the carrier gas and corresponds to blackbody Drude emission, a resonant feature can clearly be extracted. The result is a clear emission signal at a frequency corresponding to 12 meV. The emission is quite broad and corresponds to an energy width of about 5meV. This spectral range corresponds to the energy separation between the third and the second subband and is most likely due to radiative subband transitions.

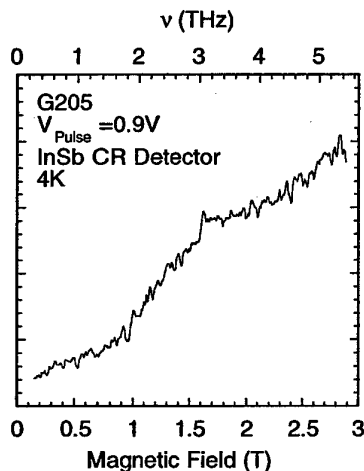


Figure 55: Emission signal from sample g205 at a bias of 0.9V as a function of the detector magnetic field.

The input power for a set of mesas which have in total an active area of $600\mu\text{m} \times 600\mu\text{m}$ amount to 200mW for sample g205 at a bias voltage of 0,9V. The emitted power can be estimated to be close to the limit of detection to be in the order of 5pW. If we assume a detection efficiency of 10^{-1} and an outcoupling loss from inside the sample of 10^{-3} this gives an estimated internally emitted radiation of $5 \times 10^{-8}\text{W}$. This gives an internal quantum efficiency of $\eta_{\text{int}}=2,5 \times 10^{-7}$ which is comparable with the quantum efficiency of the plasmon emission from parabolic quantum wells. The outcoupling loss is high mainly due to two effect: as the radiation is emitted with a polarization perpendicular to the surface, the effect of self-absorption is dominant due to a large angle of internal total reflection; the second reducing effect is due to the small size of the active emitting region as compared to the wavelength of the emitted light.

The emission from sample g301 has been studies with different mesa sizes. The best results were achieved with the mesas having rather narrow fingers of $6\mu\text{m}$. The directly measured emission spectrum with the InSb detector is shown in

Figure 56. The spectrum is considerably narrower than for sample g205. A clear resonant peak can be seen at an energy of 11 meV. This peak has a half width in the order of 3 meV and is thus considerably narrower than for g205. The peak is not present in the spectra for biases below the critical voltage for the extraction resonance.

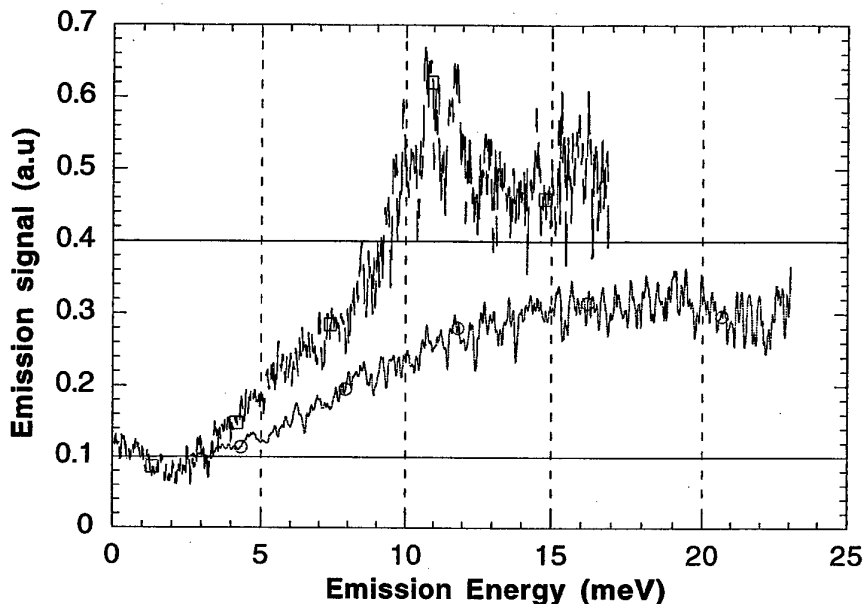


Figure 56: Emission signal of sample g301 versus energy. The upper curve is for a bias voltage of 0.7 V, the lower curve for 0.4 V.

The mesa area used for the emission experiment was $500\mu\text{m} \times 500\mu\text{m}$, the input power for the higher voltage was 170 mW and for the lower voltage 50 mW. The voltage is higher for a large number of mesas due to the appearance of series resistances. It is clearly evident that there is no resonant emission for the lower voltage. Only above a certain voltage value the narrowband emission appears. We have observed this narrow emission only in a small range of electric fields. At higher fields (above 0.8V) the input power becomes so large that thermal effect-a heating of the sample- become evident from a strong increase of the broad signal background.

The detected resonant emission intensity is somewhat higher than for sample g205 and is estimated to be in the order of 10 pW. Using the same efficiency and loss considerations as for sample g201 that means taking a total loss term of 10^{-4} , the internal emission intensity is in the order of 10^{-7}W . This gives an internal quantum efficiency 6×10^{-7} , which is a value even higher than the optimistic estimate of the parabolic quantum well emission. The structure used for sample g301 was designed in such a way that the size of the plasma

resonator is increased by 10nm as compared to g205. This is a clear indication that the plasma resonance is sensitive to a size tuning.

The main open question is now, whether we have evidence for the appearance of a plasma instability. The plasmon frequency for these structures is in the same spectral range as the observed subband emission energies. The doping of the active plasmon resonator is quite high at values of a few times 10^{17}cm^{-3} . These values are necessary to obtain the required bandstructure and the necessary high Fermi level. The Fermi level without bias is above the third level in the quantum well. This results in a completely filled second level without bias. Any emission into level two must therefore come from a reduced population of this level by an extraction process.

From this experiment we cannot draw a conclusive interpretation since the emission signal is very weak and we were not able to find a nonlinear dependence of the emission signal on the bias voltage. In addition we have to consider the fact that these high doped structures have a very high loss rate for plasma oscillations. The calculated gain for sample g301 is in the order of 1meV, which is considerably lower than the observed emission linewidth.

However, there exist possibilities to improve the structures further. The high doping can be avoided by growing bandstructure modulated structures, which mimic the doping by a bandstructure engineered band bending. This way the emission linewidth should be further reduced and reach values comparable to the predicted growth rates.

The purpose of this part of the project was to develop a new concept to generate coherent THz radiation, based on the stimulated emission of coherent plasmons, achieved without population inversion. Efforts are currently under way towards detecting and characterizing emission of THz radiation from these structures. Summarizing we can state that the proof for the existence of a plasma instability in confined semiconductor systems is around the corner. The investigation until this point took longer than anticipated at the beginning. During the process of this work it turned out that especially the understanding of the current transport through resonant structures had to be improved and that new types of emission geometries had to be developed. With the present knowledge the outlook for the proof of the existence of plasma instabilities in semiconductor nanostructures is more optimistic.

2.4.3. New plasmon generation concepts

A new concept proposes a laser scheme based on stimulated emission of plasmons without population inversion, adding a region where a dynamic charge inhomogeneity can develop to a plasmon bath. In this scheme, a dc current excites plasmons in the carrier gas and, subsequently, the resulting charge oscillations emit electromagnetic radiation [74].

The basic bandstructure of such a scheme is shown in Figure 57. The structure consists of a narrow barrier, separating the doped region to the left reservoir from the parabolically profiled active region. The curvature of this parabolic confining potential has been chosen

so that the Kohn's resonance (plasmon of the parabolic region) is at 12meV. Immediately to the right of the parabola is a linearly graded region of the pocket. Finally a narrow barrier separates the pocket from the outside doped region. This barrier and the pocket simulate the dynamic inhomogeneity region.

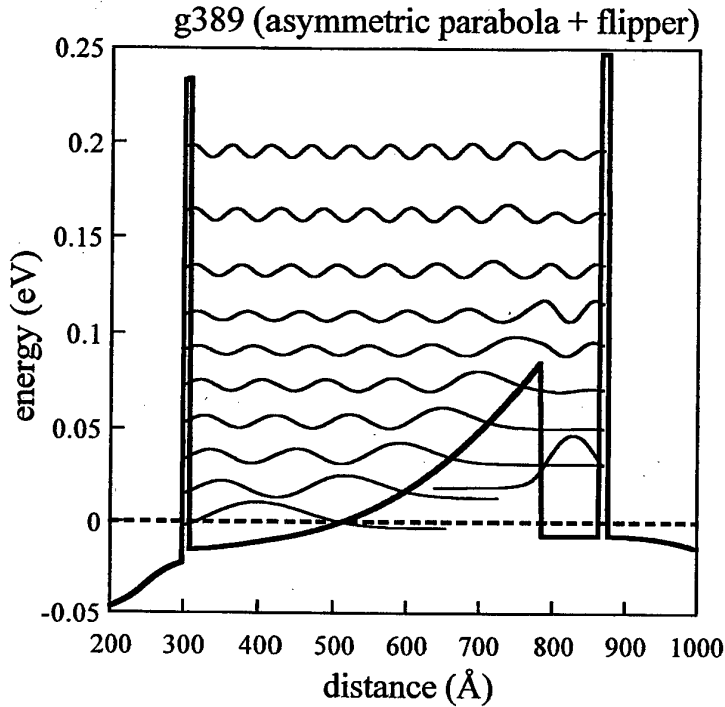


Figure 57: The energy of the conduction band edge versus distance. The solid lines represent the squared wave functions of the quantized states.

To calculate the possibility of an instability in sample g389 (asymmetric parabola with flipper, see Figure 57), the RPA formalism is employed. A robust instability at a resonant energy of 13.7meV is found. Due to non linear effects this instability supports large charge oscillations. To understand this, one has to assume that initially the pocket is empty. Then the corresponding energy position of the pocket is at its lowest value. As the pocket fills with electrons from the left the energy position of the pocket increases. In the process, the potential wedge, which rises even faster, strongly reduces the charge in-flow into the pocket. As the inflow of charge in the pocket diminishes, the current outflow through the right barrier begins to empty the pocket. Consequently the screening decreases, causing the potential energy position of the pocket to approach its minimum value again. This, in turn, lowers the wedge, and with the in-flow of charge into the pocket, the new cycle begins. This periodic charge build up in the pocket occurs at the expense of the charge in the parabolic region, and will enhance charge "sloshing" there, leading to an enhancement of the instability in the asymmetric parabolic well.

Figure 58 shows the measured I-V characteristics compared to the result of a calculation based on the RPA method. Since the quasi-groundstate of the structure can be unstable, two theoretical lines are shown for the maximum and minimum of the expected current density. The predicted instability occurs at bias above 0.15 V. The experimental data show a very good agreement to the calculated results, verifying the basic functionality of the structure.

For sample g390 (asymmetric parabola without flipper) a very good agreement between the experimental data and the calculation is also found for both bias directions. While vanishing current is predicted for reverse bias, a sharp increase of the current density at about 0.1 V is predicted and observed.

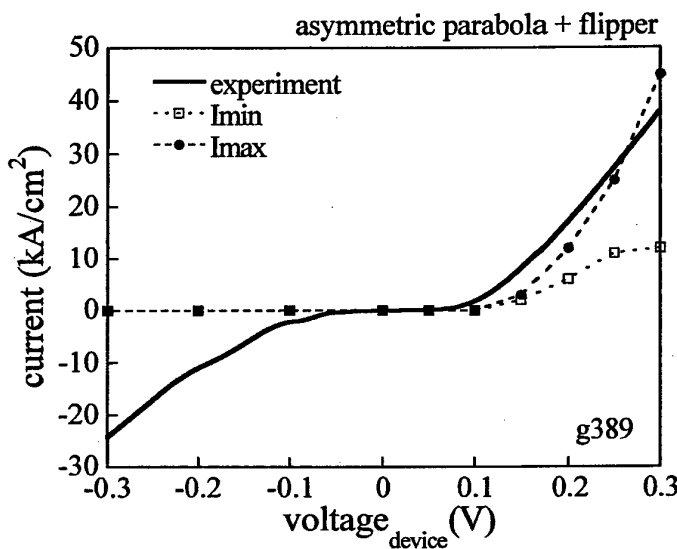


Figure 58: Measured (solid line) and calculated (dashed line) current voltage characteristics of sample g389.

In order to investigate the influence of the flipper, a reference sample with the same layer structure except the flipper has been grown (Figure 57). The IV curve of this sample is shown in Figure 59. It is evident that the behavior is different and that no instability is found in the device characteristics demonstrating that the quantum well functions as an extractor. The open question at this point is the dynamics of the flip process. Detailed time dependent investigation will be necessary to determine the dynamic response of the flip process. First emission experiments with this type of samples have not been successful. The samples show strong oscillations of the current in the high MHz range, which obscures the observation of THz emission. However the concept is promising and will be pursued further.

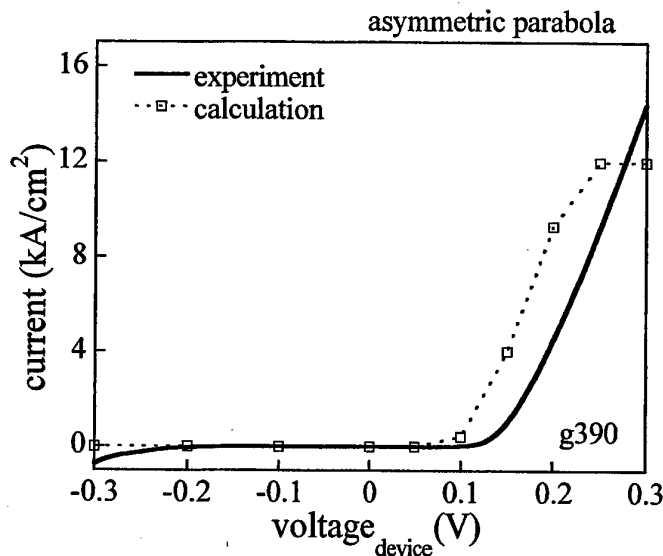


Figure 59: Measured current density (solid line) of a sample similar to sample g389 but without quantum well extractor. The dashed line shows the calculated current density.

2.5. Superlattice emission, Bloch emission

In this part of the work we concentrated our efforts on the investigation of drifting electrons in a superlattice potential. The main question to answer is whether it is possible to realize a large enough mean free path to achieve a bunching of electrons which would result in coherent THz radiation. Based on the obtained knowledge of the mean free path and the limiting scattering mechanisms we designed and optimized a two terminal 25 period GaAs/AlGaAs superlattice structure with a miniband width of 15 meV in order to investigate the possibility for carrier bunching and THz emission.

In the above investigation we found that the IV-curves in superlattices show a negative differential conductance between Helium temperatures and room temperature. The onset of negative differential conductance appears when the electric field is large enough to maintain Bloch oscillations which means that the Bloch frequency exceeds the scattering rate (old result by Esaki and Tsu). The appearance of a negative differential conductance is a requirement for the generation THz radiation based on Bloch oscillations.

We have fabricated multi mesa ridges for the emission experiment with an active area of $30\mu\text{m} \times 30\mu\text{m}$ area, which were connected with air bridges to the contact as shown in Figure 60. Current densities of up to several 10^3 Acm^{-2} were injected into the two terminal device. A bias of $V=1,35\text{V}$ and a current of 140mA are applied. The total input power is $0,19 \text{ W}$, which leads to an emission in the order of 10nW . Taking the same efficiency arguments as before the internal quantum efficiency is also found to be in the order of 5×10^{-7} , so basically the same value as for the plasmon induced emission. However as the

structures are all very similar the emission intensity could be dominated by the very inefficient outcoupling mechanism in the case of spontaneous emission.

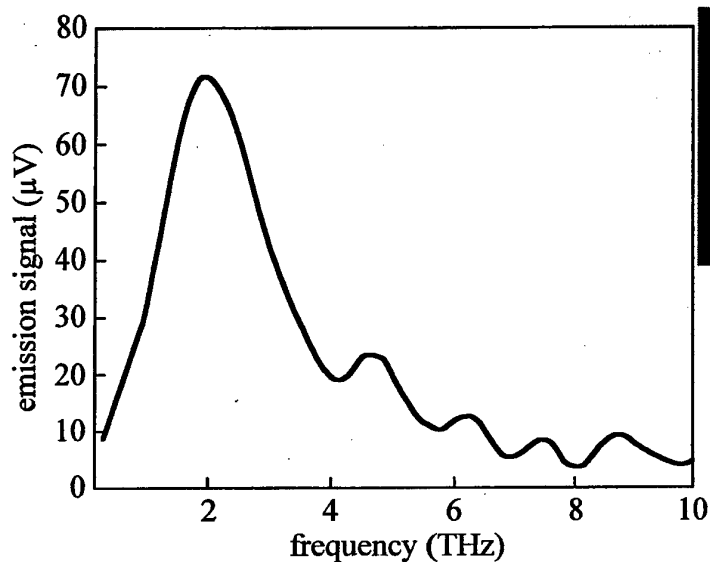


Figure 60: Emission signal of a superlattice sample measured with a step scan spectrometer as a function of frequency for a bias voltage of. The inset shows the mesa and the contact to the antenna.

A duty cycle between 1:1 and 1:10 was used to avoid sample heating. The inset of the figure shows an SEM picture of a typical single device, which was used for electrical characterization. The emission devices have the same form as shown in Figure 52. The emission spectra, measured using a step scan Fourier spectrometer at 5 K, shows a broad emission centered at 2 THz, which we attribute the spontaneous decay of Bloch oscillations in the superlattice. The calculated emission frequencies from the applied electric fields are in reasonable agreement with the observed emission frequency. Extensive work towards the realization of coherent THz emission from the above process is in the main focus of our future work. This result is the first demonstration of electrically induced Bloch emission in a semiconductor. As the IV-curves of superlattices are robust up to high temperatures, the Bloch type of emission may persist up to temperatures close to room temperature. The basic charge oscillations rely on the bunching of macroscopic charges in a similar way as the Plasma instability,

REFERENCES

- [1] W. Boxleitner, PhD theses, TU Vienna (1997).
- [2] L. Bloch and R. Tsu, IBM J. Res. Develop. **14**, 61 (1970).
- [3] M.Ogata and H.Fukuyama, Phys. Rev. Lett. **73**, 468 (1994)
- [4] D.L.Maslov and M.Stone, Phys. Rev. B **52**, R5539 (1995)
- [5] V.V. Ponomarenko, Phys. Rev. B **52**, R8666 (1995)
- [6] D.L. Maslov, Phys. Rev. B **52**, R14368 (1995)
- [7] I. Safi and H.J. Schulz, Phys. Rev. B **52**, R17040 (1995)
- [8] V.V. Ponomarenko and N. Nagaosa, Phys. Rev. Lett. **79**, 1714 (1997)
- [9] N.P. Sandler and D.L. Maslov, Phys. Rev. B **55**, 13808 (1997)
- [10] I. Safi, Phys. Rev. B **55**, R7331 (1997)
- [11] A. Yacoby, H.L. Stormer, K.W. Baldwin, L.N. Pfeiffer and K.W. West, Solid State Commun. **101**, 77 (1997)
- [12] A. Yacoby, H.L. Stormer, N.S. Wingreen, L.N. Pfeiffer, K.W. Baldwin K.W. West, Phys. Rev. Lett. **77**, 4612 (1996)
- [13] A.Y. Alekseev and V.V. Cheianov, Phys. Rev. B **57**, R6834 (1998)
- [14] S. Tarucha, T. Honda and T. Saku, Solid State Commun. **94**, 413 (1995)
- [15] T. Honda, S. Tarucha, T. Saku and Y. Tokura, Jpn. J. Appl. Phys. **34**, L72 (1995)
- [16] K.J. Thomas, M.Y. Simmons, J.T. Nicholls, D.R. Mace, M. Pepper and D.A. Ritchie, Appl. Phys. Lett. **67**, 109 (1995)
- [17] K.J. Thomas, J.T. Nicholls, M.Y. Simmons, M. Pepper, D.R. Mace and D.A. Ritchie, Phys. Rev. Lett. **77**, 135 (1996)
- [18] A. Gold and L. Calmels, Phil. Mag. Lett. **74**, 33 (1996)
- [19] K.J. Thomas, J.T. Nicholls, N.J. Appleyard, M.Y. Simmons, M. Pepper, D.R. Mace, W.R. Tribe and D.A. Ritchie, Phys. Rev. B **58**, 4846 (1998)
- [20] L. Langer, V. Bayot, E. Grivei, J.P. Issi, J.P. Heremans, C.H. Olk, L. Stockman, C. van Haesendonck and Y. Bruynseraede, Phys. Rev. Lett. **76**, 479 (1996)
- [21] M. Bockrath, D.H. Cobden, P.L. McEuen, N.G. Chopra, A. Zettl, A. Thess and R.E. Smalley, Science **275**, 1922 (1997)
- [22] S.J. Tans, M.H. Devoret, H. Dai, A. Thess, R.E. Smalley, L.J. Geerligs and C. Dekker, Nature **386**, 474 (1997)
- [23] A. Bezryadin, A.R.M. Verschueren, S.J. Tans and C. Dekker, Phys. Rev. Lett. **80**, 4036 (1998)
- [24] D.H. Cobden, M. Bockrath, P. McEuen, A.G. Rinzler and R.E. Smalley, Phys. Rev. Lett. **81**, 681 (1998)
- [25] T.W. Ebbesen, Physics Today **49** (No.6), 26 (1996)
- [26] S. Frank, P.P. Poncharal, Z.L. Wang and W.A. de Heer, Science **280**, 1744 (1998)
- [27] A. Globus, C.W. Bauschlicher, J. Han, R.L. Jaffe, C. Levit, D. Srivastava, Nanotechnology **9** (Special issue featuring papers from the 5th Foresight Conference on Molecular Nanotechnology), 192 (1998)
- [28] V.L.Gurevich and Y.A.Firsov, Zh. Eksp. Teor. Fiz. **40**, 198 (1961) (Sov.Phys. JETP **13**, 137 (1961))
- [29] R.L.Peterson, in Semiconductors and Semimetals, Vol.**10**, p.221 eds.: R.K.Willardson and A.C.Beer, Academic Press, New York (1975)

-
- [30] R.A.Stradling, R.A.Wood, Solid State Comm. **6**, 701 (1968)
- [31] P.G.Harper, J.W.Hodby, R.A.Stradling, Rep. Prog. Phys. **37**, 1 (1973)
- [32] D.Schneider, D.Rürup, B.Schönfelder and A.Schlachetzki, Z. Phys. B **100**, 33 (1996)
- [33] D.Schneider, K.Fricke, J.Schulz, G.Irmer, M.Wenzel, Proceedings of the 23rd Int. Conf. Physics of Semiconductors Vol.1, p.221 ed. by M.Scheffler and R.Zimmermann, World Scientific (1996)
- [34] D.C.Tsui, T.Englert, A.Y.Cho and A.C.Gossard, Phys. Rev. Lett. **44**, 341 (1980)
- [35] M.A.Brummell, R.J.Nicholas, M.A.Hopkins, J.J.Harris and C.T.Foxon, Phys.Rev.Lett. **58**, 77 (1987)
- [36] M.A.Brummell, D.R.Leadley, R.J.Nicholas, J.J.Harris and C.T.Foxon, Surf. Sci. **196**, 451 (1988)
- [37] D.R.Leadley, R.J.Nicholas, J.Singleton, W.Xu, F.M.Peeters, J.T.Devreese, J.A.Perenboom, L.van Bockstal, F.Herlach, J.J.Harris and C.T.Foxon, Phys. Rev. Lett. **73**, 589 (1994)
- [38] W.Xu, F.M.Peeters, J.T.Devreese, D.R.Leadley and R.J.Nicholas, Int J.Mod.Phys. B **10** 169 (1996)
- [39] G.Berthold, J.Smoliner, C.Wirner, E.Gornik, G.Böhm, G.Weimann, M.Hauser, C.Hamaguchi, N.Mori and H.Momose, Semicond. Sci. Technol. **8**, 735 (1993)
- [40] G.Berthold, *Magnetotransport in niederdimensionalen Elektronensystemen*, PhD thesis, Technische Universität München (1993)
- [41] C.Wirner, *Untersuchung der Driftgeschwindigkeit und der Geschwindigkeits-Verteilungsfunktion niedrigdimensionaler Elektronengase*, PhD thesis, Technische Universität München (1993)
- [42] W.Demmerle, *Tunnelspektroskopie an niederdimensionalen Elektronensystemen*, Dissertation, Technische Universität München (1993)
- [43] G.Ploner, J.Smoliner, G.Strasser, M.Hauser and E.Gornik, Phys. Rev. B **57**, 3966 (1998)
- [44] G.Ploner, PhD Thesis, Technische Universität Wien (1998)
- [45] N.Mori, H.Momose, K.Taneguchi, and C. Hamaguchi, Phys.Rev. B **38**, 7622(1988)
- [46] J. Smoliner, G. Berthold, F. Hirler, N. Reinacher, Semicond. Sci. Technol. **6**, 642 (1991)
- [47] J. Wang, P.H. Beton, N. Mori, L. Eaves, H. Buhmann, L. Mansouri, P.C. Main, T.J. Foster and M. Henini, Phys. Rev. Lett. **73**, 1146 (1994)
- [48] P.H. Beton, J. Wang, N. Mori, L. Eaves, P.C .Main, T.J. Foster and M. Henini, Phys. Rev. Lett. **75**, 1996 (1995)
- [49] S.Q. Murphy, J.P. Eisenstein, L.N. Pfeiffer and K.W. West, Phys. Rev. B **52**, 14825 (1995)
- [50] N. Turner, J.T. Nicholls, E.H. Linfield, K.M. Brown, G.A.C. Jones and D.A. Ritchie, Phys. Rev. B **54**, 10614 (1996)
- [51] B. Kardinal, C.H.W. Barnes, E.H. Linfield, D.A. Ritchie, K.M. Brown, G.A.C. Jones and M. Pepper, Phys. Rev. Lett. **76**, 3802 (1996)
- [52] B. Kardinal, C.H.W. Barnes, E.H. Linfield, D.A. Ritchie, J.T. Nicholls, K.M. Brown, G.A.C. Jones and M. Pepper, Phys. Rev. B **55**, R1966 (1997)
- [53] see, for example, L. Zheng and A.H. MacDonald, Phys Rev. B **47**, 10619 (1993)

-
- [54] W. Demmerle, J. Smoliner, E. Gornik, G. Böhm and G. Weimann, Phys. Rev. B **47**, 13574 (1993)
- [55] K.M. Brown, E.H. Linfield, D.A. Ritchie, G.A.C. Jones, M.P. Grimshaw and M. Pepper, Appl. Phys. Lett. **64**, 1827 (1994)
- [56] J.P. Eisenstein, L.N. Pfeiffer and K. West, Appl. Phys. Lett. **57**, 2314 (1990) and Appl. Phys. Lett. **58**, 1497 (1991)
- [57] J. Wang, P.H. Beton, N. Mori, H. Buhmann, L. Mansouri, L. Eaves, P.C. Main, T.J. Foster and M. Henini, Appl. Phys. Lett. **65**, 1124 (1994)
- [58] G. Ploner, H. Hirner, T. Maier, G. Strasser, J. Smoliner and E. Gornik, Appl. Phys. Lett. **74**, 1758 (1999)
- [59] H. Hirner, Diploma Thesis, Technische Universität Vienna (1999)
- [60] N. Mori, P.H. Beton, J. Wang and L. Eaves, Phys. Rev. B **51**, 1735 (1995), N. Mori, P.H. Beton, J. Wang and L. Eaves, Phys. Rev. B **52**, 1504 (1995),
- [61] G. Scarmarcio, et al., Science **276**, 773 (1997).
- [62] M. Helm, Semicond. Sci. Technol. **10**, 557 (1995).
- [63] G. Snyder, (1997).
- [64] E. Gornik, Landau emission
- [65] A. Wixforth, M. Kaloudis, C. Rocke, K. Ensslin, M. Sundaram, J. H. English, A. C. Gossard, Semicond. Sci. Technol. **9**, 215 (1994).
- [66] K. D. Maranowski, A. C. Gossard, K. Unterrainer, E. Gornik, Appl. Phys. Lett. **69**, 3522 (1996).
- [67] A. C. Gossard, M. Sundaram, P. F. Hopkins, in "*Epitaxial Microstructures*", edited by A. C. Gossard (Academic, Boston, 1994), p. 153.
- [68] J. Ulrich, R. Zobl, K. Unterrainer, G. Strasser, E. Gornik, K. D. Maranowski, A. C. Gossard, Appl. Phys. Lett. **25**. May (1999).
- [69] J. N. Heyman, K. Unterrainer, C. Craig, B. Galdrikian, M. S. Sherwin, K. Campman, P. F. Hopkins, A. C. Gossard, Phys. Rev. Lett. **74**, 2682 (1995).
- [70] A.B. Mikhailovskii, Theory of Plasma Instabilities, Vol. 1 (Consultants Bureau, New York, 1974).
- [71] K. Kempa, P. Bakshi, and E. Gornik, Phys. Rev. B **54**, 8231 (1996)
- [72] K. Kempa, P. Bakshi, C. Du, G. Feng, A. Scorupsky, G. Strasser, C. Rauch, K. Unterrainer, and E. Gornik, Journal of Appl. Physics **84** (7), 1 (1999).
- [73] W.R. Frensel, Rev. Mod. Phys. **62**, 745 (1990).
- [74] K. Kempa, and P. Bakshi private communication